UNIVERSITY OF OKLAHOMA

GRADUATE COLLEGE

SEISMIC DATA CONDITIONING AND ANALYSIS FOR FRACTURED RESERVOIRS

A DISSERTATION

SUBMITTED TO THE GRADUATE FACULTY

in partial fulfillment of the requirements for the

Degree of

DOCTOR OF PHILOSOPHY

By

ABDULMOHSEN ALALI
Norman, Oklahoma
2018

SEISMIC DATA CONDITIONING AND ANALYSIS FOR FRACTURED RESERVOIRS

A DISSERTATION APPROVED FOR THE
CONOCOPHILLIPS SCHOOL OF GEOLOGY AND GEOPHYSICS

BY

Dr. Kurt Marfurt, Chair

Dr. S. Lakshmivarahn

Dr. Norimitsu Nakata

Dr. Xiaowei Chen

Dr. Jamie P. Rich

To my parents, Layla and Mohammed

Acknowledgements

First, I would like to express my sincere gratitude to my advisor Prof. Kurt Marfurt for his continuous support of my Ph.D. study and related research, as well as for his patience, motivation, and immense wealth of knowledge. His guidance helped me tremendously during the research and writing of this thesis. He approaches every day with so much optimism, respect, and passion, which is an inspiration to me and is, in my humble opinion, part of what it truly means to be human.

A special thanks as well to committee member Dr. Norimitsu Nakata for the endless discussions and fruitful meetings we have had ever since he joined the department. He has had a big influence on my dissertation and I am forever grateful. If I may give Dr. Nakata a nickname, it would be the "geophysics express".

I would also like to thank the rest of my thesis committee, Prof. Sivaramakrishnan Lakshmivarahan, Dr. Xiaowei Chen, and Dr. Jamie Rich, not only for their insightful comments and encouragement, but also for the hard questions they asked which inspired me to widen my research to include various other perspectives.

Moreover, I would like to thank my fellow graduate students and the whole AASPI group for the stimulating discussions and all the fun we have had in the last four years. Special thanks to Thang Ha, Bin Lyu, Ali Alshafai, and Jie Qi for your constant inspiration.

Furthermore, I would like to thank Saudi Aramco for sponsoring me during my studies and, in particular, my previous supervisor, Panos Kelimas, and my current supervisor, Mustafa Alali. The management has put a huge amount of faith in me and I hope to repay them with hard work and dedication in the years to come.

And finally, special thanks to my family. Words cannot express how grateful I am to my spouse "Walaa" and my son "Qusai" for all the sacrifices that they have made on my behalf.

Although I may have more gray hair than either of them, I think I have learned more from them throughout the course of my studies.

Table of Contents

List of Figures

Abstract

The ability to identify the intensity and orientation of fractures within both unconventional and conventional resources can have a critical impact on oil field development. Fractures and faults are often the primary pathways for hydrocarbon migration and production. Because of their complexity and commercial importance, fractures have been studied by each of the main disciplines – geology, geophysics, petrophysics, and engineering. The focus of this dissertation is to present an understanding of how different geophysical technologies can be used to characterize fractures at different scales. Seismic attributes are one of the main tools to map the distribution of fractures and can be categorized into geometric attributes, azimuthal velocity anisotropy, amplitude variation with offset and azimuth, and diffraction imaging. These categories are complementary to each other and can provide overlapping information. The diversity of the assumptions under each category makes it challenging to bridge the gap for real world applications.

Acquisition footprint overprints most seismic surveys and can mask or in some cases be misinterpreted as underlying faults and fractures. There are two modern trends in imaging the subsurface with high quality 3D seismic surveys. The first is to acquire new high density, high fold, wide azimuth surveys that exhibit less footprint. The second is to combine multiple legacy surveys into "megamerge" (or even "gigamerge" surveys) that exhibit multiple footprint patterns. To address this latter problem, I start my dissertation by introducing an adaptive 2D continuous wavelet transform (CWT) footprint suppression workflow whose design is based on artefacts seen on seismic attributes. Suboptimum seismic acquisition is one of the major causes of acquisition footprint. 5D interpolation (also called 5D regularization) is a modern seismic processing workflow that attempts to fill in the missing offsets and azimuths. I examine the effect of a commercial Fourier-based 5D interpolation on both footprint artefacts and geologic discontinuities

measured using seismic attributes. I find that by accurately interpolating specular reflections, 5D interpolation suppresses acquisition footprint and improves the lateral continuity of prestack inversion images of P-impedances. Unfortunately, 5D Fourier-based interpolation incorrectly corrects diffraction events and therefore attenuates faults and karst edges seen in coherence.

Whereas 5D interpolation attempts to enhance the specular component of seismic data, diffraction imaging attempts to enhance the non-specular or diffracted component of the seismic data necessary to image fractures. Although the lateral resolution of diffractions is better than that of specular reflections, closely spaced fractures forming a "fracture swarm" may appear to be a single, larger fracture, while more laterally extensive fracture swarms give rise to azimuthal and offset anisotropy. I investigate each technique's ability to detect fractures using forward modeling and find that diffraction's focusing sensitivity to velocity inaccuracies makes it an excellent candidate to highlight close-spaced fractures. I also find that cross-correlating images of diffractions from nearby experiments is useful in constructing an objective function that can be used to update the velocity due in the image domain. I demonstrate the efficiency of these findings using synthetic models with different complexity. Azimuthal and offset anisotropy signature for irregularly spaced fractures is complex and different from the constant fracture spacing approximated by effective medium theory particularly for reflection below the fractures. I find isotropic amplitude variation modeling give an indication if fractures are located at the bottom portion of the reservoir.

Chapter 1: Introduction

Naar et al. (2006) state that "All reservoirs should be considered fractured until proven otherwise." Fractures exist across a vast range of scales, from millimeter-scale microcracks to macroscopic kilometer-long features. Fractures matter in drilling, well completion, and reservoir management, effecting the economics of a development program (Delbecq et al., 2013). Fractures and their response to waste water are also of interest to government regulators concerned about induced seismicity (Wines, 2016). The ability to identify fractures and their characteristics is critical and depending on the scale, different geophysical techniques are used to image the fractures (Figure 1.1). This dissertation is structured in chapters that address challenges not only for analyzing fractures at different scales but also in seismic data conditioning.

Chapters 2 and 3 address concepts of data conditioning, where one of the major challenges is coherent and random noise linked to the seismic data acquisition and processing. "Acquisition footprint" refers to the component of the seismic amplitude that in some way mirrors the lateral deployment of sources and receivers of the acquisition geometry. There are multiple causes and therefore multiple expressions of acquisition footprint, including coherent noise such as guided, surface that are insufficiently attenuated before or by the stack or systematic errors introduced by an inaccurate velocity model. In chapter 2 I present a novel workflow that uses a 2D Continuous Wavelet Transform (CWT) to suppress acquisition footprint and incoherent noise on poststack seismic data. that for either time, money, or even data access reasons cannot be reprocessed from the original common shot gathers. I show that by decomposing time slices of amplitude and attribute data into voices and magnitudes using 2D wavelets., that I can design filters to suppress footprint whose pattern varies laterally across the survey. I demonstrate the efficacy of the method

on a legacy data volume from the Delaware Basin of New Mexico and on a recently reprocessed mega-merge of four legacy surveys exhibiting two footprint patterns from north Texas.

In the chapter 3, I use a commercial implementation of a Fourier transform based 5D interpolation algorithm to further regularize a well-sampled data modern from northwest Oklahoma. I show that an underrecognized pitfalls associated with Fourier based interpolation is the suppression of subtle but important lateral discontinuities such as faults and karst edges. Through numerical models, I show how the technique accurately interpolates specular reflections but inaccurately interpolates non-specular diffractions. Such inaccurately interpolated diffractions result in the attenuation of fault and karst edges at the target Mississippian horizon and a channel at the shallower Pennsylvanian age Red Fork horizon.

Chapters 4 and 5 focus on the transition from micro-scale to meso-scale fractures using full wave modeling software. In the chapter 4, I examine the effect of fracture clustering and the validity of effective medium theory. After reviewing the theoretical background, I examine the differences between models of constant vs. random fracture spacing in both confined and unconfined settings. I hypothesize that modeling the isotropic amplitude variation with offset can provide indication of the location of fractures within the formation of interest. I also examine factors controlling diffraction imaging resolution on fractures and their horizontal orientation.

In chapter 5, I utilize diffraction's high sensitivity to local errors in the velocity model, with the goal to better locate and focus the diffractors. I present a workflow consisting of two steps. First, I analyze the velocity errors based on the focused energy of diffracted events in the image-domain. For a single common shot image, the maximum energy along each migrated trace provides a maximum focusing at the diffraction location for the correct velocity. The diffractor can be

distinguished even in the heterogenous medium. Second, I improve upon this initial observation by cross-correlating multiple nearby common shot images, where the cross-correlation are both maximum and laterally symmetric for the correct velocity. I combine these observations to construct an objective function, which can be used to estimate velocity errors in the image-domain.

I summarize my conclusions in Chapter 6.

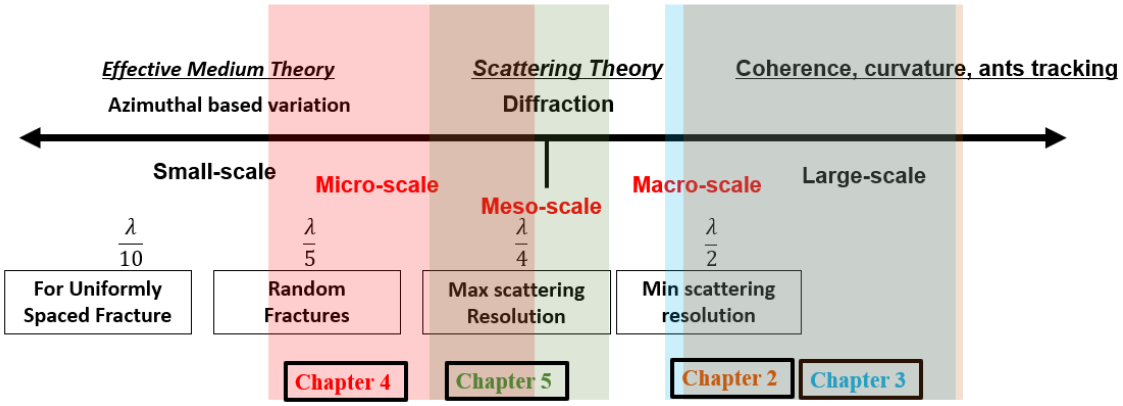

Figure 3.1. Different scale fractures are detected using different techniques. Larger scales can be detected through seismic attributes such as coherence. Meso-scales can be detected using diffraction imaging. Micro-scale can be detected through AVAz and AVO.

References

Delbecq, F., J. Downton, and M. Letizia, 2013, A math-free Look at azimuthal surface seismic techniques: CSEG Recorder, 21-31.

Narr, W., D. W. Schechter, and L. B. Thompson, 2006, Naturally fractured reservoir characterization: SPE.

Wines, M., 2016, Oklahoma puts limits on oil and gas wells to fight quakes: The New York Times, A12-A15.

Chapter 2: Attribute-assisted footprint suppression using a 2D continuous wavelet transform

Published as:

Alali, A., G. Machado and K.J. Marfurt (2018), Attribute-assisted footprint suppression using a 2D continuous wavelet transform, Interpretation, 6, no. 2, T457-T470.

Abstract

Acquisition footprint manifests itself on 3D seismic data as a repetitive pattern of noise, anomalously high amplitudes, or structural shifts on time or horizon slices that is correlated to the

location of the sources and receivers on the earth's surface. Ideally, footprint suppression should be handled by denser seismic acquisition and more careful prestack processing prior to seismic imaging. In the case where only legacy data exist, or where economic and time constraints preclude more expensive acquisition and more careful processing, interpreters must deal with data contaminated by footprint. While accurate time-structure maps can be constructed from footprint-contaminated data, the effect of footprint on subsequent attributes such as coherence, curvature, spectral components, and P-wave impedance will be exacerbated. In this work, we propose a workflow that uses a 2D Continuous Wavelet Transform (CWT) to suppress coherent and incoherent noise on poststack seismic data. The method involves decomposing time slices of amplitude and attribute data into voices and magnitudes using 2D wavelets. We exploit the increased seismic attribute sensitivity to the acquisition footprint to design a mask to suppress the footprint on the original amplitude data. The workflow is easy to apply and improves both the interpretability of the data and improves subsequent attribute resolution.

Introduction

The interpretation of 3D seismic data and attribute analysis is challenging in the presence of severe noise. In reflection seismic data, we generally consider the reflected and the diffracted wavefields to be signal and everything else to the noise. The noise can be either coherent or incoherent. Coherent noise can be defined as non-reflection energy that contains a systematic phase relation between adjacent traces and remains strong after stacking (Sheriff, 2002). In contrast, noise that either is or appears to be random will be weaker after stacking. Acquisition footprint refers to that component of the seismic amplitude that in some way mirrors the lateral deployment of sources and receivers of the acquisition geometry. While acquisition footprint is

often associated with coherent noise, its root cause is more systemic, allowing it to generate artifacts from incoherent noise and even signal as well. Edge detection attributes like coherence and curvature exacerbate the appearance of footprint, thus hindering their effectiveness detecting fractures and faults. The effects of footprint can also contaminate more quantitative attribute analysis, including impedance inversion and waveform classification.

Cahoj et al. (2016) used seismic modeling to hypothesize the main causes of acquisition footprint: (1) coherent noise such as guided, surface and airwave data that are insufficiently attenuated before or by the stack array, (2) systematic errors introduced by an inaccurate velocity model, resulting in non-flat and/or stretched NMO-corrected or migrated gathers.

Dense acquisition greatly reduces the impact of acquisition footprint (Meunier et al. 2008). Alternatively, acquisition footprint can be suppressed in the processing workshop using more careful velocity analysis, least-squares migration (Ha and Marfurt, 2017), and 5D interpolation (Trad, 2009; Chopra and Marfurt, 2013). In the case where only legacy data exist, or where economic and time constraints preclude more expensive acquisition and more careful processing, interpreters must deal with data contaminated by footprint. While accurate time-structure maps can be constructed from footprint-contaminated data, the effect of footprint on subsequent attributes such as coherence, curvature, spectral components, and P-wave impedance will be exacerbated.

Several techniques can be found in the literature on filtering the acquisition footprint on poststack data through domain transformation. Sahai and Soofi (2006) used a 2D low-pass filter in the k_x - k_y domain to suppress the footprint. Drummond et al. (2000) used a wavenumber notch filter to estimate the noise and adaptively suppress it. Soubaras (2002) used the offset distribution

as an input to design a k_x - k_y filter to attenuate the footprint. This latter filter can be very effective but requires access to (at least the geometry of) the prestack traces. A pitfall with any filter is if the signal and noise overlap in the transform domain. For this reason, highly localized notches are much more effective than broad interpreter-drawn polygons. Chen et al. (2012) used an adaptive stationary wavelet transform to suppress footprint and other random noise. Al-Bannagi et al. (2005) used a truncated singular value decomposition algorithm in a cascaded multi-directional manner to suppress the noise on a time/horizon slice. In this paper, we use a 2D continuous wavelet transform variation of a workflow based on application of k_x - k_y filters constructed from attributes originally proposed by Falconer and Marfurt (2008), and extended by Davogustto (2011).

Filtering in the wavelet transform domain has been used in seismic data processing for the past 20 years. Selesnick et al. (2005) highlight the pros and cons continuous and discrete wavelet transforms (CWT and DWT). The DWT is widely used in seismic data compression (Vassiliou et al., 1984). Goudarzi et al. (2014) implemented a 2D DWT to attenuate ground roll. The CWT is more amenable to seismic processing, with one of the more common applications being the attenuation of the airwave within a processor-defined corridor (Schuster and Sun, 1993). Yu and Whitcombe (2008) applied 2D CWT on common shot gathers to parameterize and then suppress coherent noise components. Yu et al. (2017) used a 3D CWT to suppress coherent noise, cross talk and random noise on prestack gathers. Although this list is not complete, it gives a flavor of different applications of filtering in the wavelet domain.

In this paper, we present a novel technique that uses 2D Continuous Wavelet Transform to model the footprint and subsequently suppress it on poststack data volumes, time slice by time slice. First, we introduce the arithmetic and various element in the workflow. Second, apply the

workflow to legacy data volumes, showing how to use attribute in the filter design. Finally, we quantify the parameters considered in the noise suppression and illustrate potential pitfalls.

Method

1D Fourier Transform

For a given function in space $f(x)$, the spatial Fourier transform is given by:

$$\hat{f}\ (k_x) = \int_{-\infty}^{\infty} f(x)\, e^{-g\,2\pi k_x x}\, dx, \qquad (1)$$

where x is the distance, k_x is the spatial wavenumber scaling constants have been omitted, $\hat{\mathrm{f}}\,(k_x)$ is the data in the wavenumber domain and $g = \sqrt{-1}$. The Fourier transform converts the signal in space f(x) to the wavenumber domain by integrating over the whole space axis into a complex function $\hat{\mathrm{f}}\,(k_x)$. The Fourier transform can precisely detect which frequencies reside in the data, but yields no information about the time position of signal features.

1D Continuous Wavelet Transform

The continuous wavelet transform can be defined differently based on the normalization and conjugation and it gives the projection of the function $f(x)$ at any scale a and position u into wavelet domain by (Mallat, 2009):

$$C\ (a,u) = \frac{1}{\sqrt{a}} \int_{-\infty}^{\infty} f(x) \psi \left(\frac{x-u}{a}\right) dx, \qquad (2)$$

where $C\ (a,u)$ refers to the data in the wavelet transform domain, and ψ is the wavelet used to transform the data, a is the dilation or scale, while u is the translation parameter. We can make a couple of observation on equation 2. First, it transforms the input data from one dimension into a two dimensions. Second, the term $(x-u)$ in the integral indicates that CWT is a convolution process and hence we can rewrite it as:

$$C\ (a,x) = f(x) * \psi\left(\frac{x}{a}\right). \tag{3}$$

Equation 3 simply states that the CWT is a convolution of the input data with a set of complex-valued functions generated from the mother wavelet (Liner, 2010). Therefore, for computation efficiency we can compute the wavelet transform in the Fourier domain where convolution is replaced by multiplication. Hence, we can rewrite equation 2 as:

$$C\ (a,x) = FT^{-1}\{a\hat{f}\ (k_x)\ \hat{\psi}(ak_x)\}, \tag{4}$$

where $\hat{\psi}(ak_x)$ is the Fourier transform of wavelet modulated by the scale a and FT^{-1} is the inverse of the Fourier transform. Next, we illustrate the parameters of CWT in equation 2 to build up the understanding our application. For that purpose, we consider two wavelets with different dilations (a) and their representation in the wavenumber domain in Figure 2.1a. For simplicity, we assume that the Fourier transform of the wavelet is nonzero in the positive wavenumber and consider a real wavelet only. First, Figure 2.1a indicates that a short dilatation wavelet corresponds to a high wavenumber content in the transform domain and vice versa. Consequently, the dilation of the wavelet in the space domain controls the number of components i in the transform domain, needed to cover the whole spectrum. Also, it controls the interval shift in the wavenumber η, given by $\frac{(max(k_x))}{i}$. In our application, we use a uniformly shifted version of that of the prototype filter along

the wavenumber domain. Hence, the magnitude response of all the wavelets is uniformly transform into a Gabor wavelet or more accurately a modified Morlet wavelet in the space domain (Cohen, 1995). In the wavenumber-domain the wavelet can be given as:

$$\hat{\psi}(k_x) = \begin{cases} \left(\cos\frac{\pi(\eta\, i - k_x)}{2\,\eta}\right)^2, \eta(i-1) \le k_x \le \eta(i+1)\,, \\ 0,\ otherwise \end{cases} \qquad (5)$$

As indicted by Equation 5 the wavelets' spectrum in the wavenumber domain is represented by a raised-cosine at each component *i.* Figure 2.1b shows a couple of the 1D wavelets for eleven components along the k_x showing the real, imaginary and absolute wavelets.

The 2D Continuous Wavelet Transform

The 2D continuous wavelet transform can be thought of as two cascaded 1D CWTs which can be implemented as a 2D convolution in the x-y space domain or as a simple multiplication in the k_x-k_y wavenumber domain. Generalizing equation 4 by representing the 2D wavelet transform . $\mathrm{C}\,(i,j,x,y)$ as the inverse Fourier transform of the multiplication between the input data and wavelets of choice gives

$$\mathrm{C}\,(i,j,x,y) = FT^{-1}\{i\,j\,\hat{f}(k_x,k_y)\,\hat{\psi}(ik_x + jk_y)\}, \qquad (6)$$

where

k_x and k_y are the wavenumbers,

i and j are the indices of the components

$\hat{f}(k_x, k_y)$ is the 2D spatial Fourier transform of the amplitude or attribute slice, and

$\hat{\psi}$ is the 2D spatial Fourier Transform of the wavelets.

Choosing values of i and j to be $-5 \leq i \leq +5$ and $-5 \leq j \leq +5$ results in 121 2D wavelets. Figure 2.2 shows nine representative wavelets (one central and eight outer components) of 121 in the wavenumber domain. Figure 2.3 shows 2D spatial wavelets of the nine center real and imaginary components. We notice that the real and imaginary wavelet satisfy the Hilbert relation with a 90 degrees shift between the two. Also, we can predict that the 2D image in space will be decomposed into four minor orientations: an isotropic orientation in the center, and east-west, north-south and diagonal azimuthal orientations away from the center. Based on the number of components used, the corresponding 2D wavelet characteristics will change. We define the voices and magnitudes, which are the data in the CWT domain, for the component $(i,j)^{th}$ to be:

$$mag(i,j) = |C(i,j,x,y)| \tag{7}$$

$$voc(i,j) = \Re[C(i,j,x,y)] \tag{8}$$

where *mag* are the magnitudes, *voc* are the voices and $\Re$ is the real part. Ultimately, one can consider the magnitudes and voices as the data decomposed into different wavenumber components using the 2D absolute and real wavelets.

Mask:

Attributes computed along structure such as coherence exacerbate footprint anomalies but are relatively insensitive to dip, allowing us to use the 2D CWT of an attribute to design a mask. The mask, *m(i,j)*, is defined as

$$m(i,j) = \frac{\varepsilon\, mag\ (0,0)}{\varepsilon\, mag\ (0,0) + mag\ (i,j)} \quad (9)$$

where *mag (0,0)*, is the zero-wavenumber (or mean background magnitude) component and ε is a fractional value. For attributes computed along dip, the (0,0) component will be the largest while other components (with the exception of periodic footprint) will be significantly smaller. We apply the mask in equation 1 to the 2D CWT of the seismic amplitude data, allowing us to reject 2D CWT components that are significantly greater than a user-defined percentage of the (0,0) component. Thus, if $mag(i,j) \gg \varepsilon \times mag\ (0,0)$, the mask, $m(i,j) \approx 0$, and the *(i,j)*th hypothesized footprint component is kept. In contrast, if $mag(i,j) \ll \varepsilon \times mag\ (0,0)$, the mask, $m(i,j) \approx 1$, and the *(i,j)*th component is rejected. This allows us to model the noise.

The value of ε ranges between 0 and 1, with smaller values suppressing more components. The mask is calculated so that when it is applied to the voices, it will match the data as well as possible in a least-squares sense. Subsequently, the generated footprint is subtracted from the original data. The reconstructed data, lacking the voice (s) representing the footprint, is a more interpretable seismic amplitude data set with better signal. Figure 2.4 shows the workflow implemented by this algorithm.

Results and Discussion

We demonstrate our proposed technique by applying it to two vintage data. The first volume is acquired from Vacuum field in southeast New Mexico and on the northwest shelf of the Permian Basin. The field is associated with an anticline developed through differential compaction and faulting. The time slice under consideration is at 450 ms, just above the San Andres producing formation (Pranter et al., 2004). Figure 2.5 shows the amplitude and coherence slices considered

for this analysis. On the amplitude slice, we notice a strong amplitude contrast corresponding to the gently dipping layers. The coherence slice shows coherent geology as high coherency and footprint as low coherence expressions. Figure 2.6 shows the k_x - k_y domain of both the data and attribute, the noise appears as periodic spikes in the transform domain. In our case, we use 121 components, $5 \leq i \leq +5$ and $-5 \leq j \leq +5$, and $\varepsilon = 0.15$ but we will limit our analysis through this section on the nine central components to illustrate how the method works. Ultimately, we will make the case to why we think the magnitude of the attribute yields a better mask to suppress the noise.

We start with the amplitude slice; Figure 2.7 shows the nine central magnitudes of 121 components. The central *(0,0)* component (Figure 2.7e) is the result of cross-correlating the isotropic 2D wavelet with the amplitude slice. It is dominated by the geology and is noise free. Figure 2.7b and 7h show magnitudes with a weak north-south azimuthal orientation, while Figure 2.7d and 7f show a weak east-west azimuthal orientation. The strong amplitude features highlighting the azimuthal orientation indicate the sensitivity of the magnitude of the amplitude data to the geology. Next, we consider the voices of the amplitude data shown in Figure 2.8. The azimuthal orientation on the voices are more pronounced than on the magnitudes. Note the north-south (Figure 2.8b and 8h), east-west (Figure 2.8d and 8f) and a diagonal azimuthal orientation on the four corner voices. These non-central azimuthal orientations are affected by both the geology and footprint with the central voice also dominated by the signal but not impacted by acquisition footprint noise.

Next, we consider the magnitude and voices of the coherence slice. The nine central magnitudes are shown in Figure 2.9. We do not observe a pronounced azimuthal orientation in all

magnitudes. Further, the coherent geology corresponds to a low magnitude in all the components except for the central component. This leads us to conclude that the magnitudes of the coherence are more sensitive to noise than to coherent geology. In other words, it recognizes the coherent geology and exacerbates the noise. Thus, the magnitudes of the coherence provide a good candidate to compute the mask to filter out the noise.

Figure 2.10 shows the voices of the attribute. Similar azimuthal orientations are seen on the nine components with a clear sensitivity to the noise but not to the geology. For that purpose, we cannot apply the mask to these voices as they lack the geology, to begin with. This leads to us to design the mask using the magnitude of the attribute, according to equation 6, then applying it to the voices of the data

Next, we address the choice of number of components and threshold ε. For that purpose, we vary the parameters needed to design the mask and analyze the results. In theory, the optimum number of components is a function of the acquisition parameters which defines the periodicity of the footprint in the k_x - k_y domain. This survey was acquired using an orthogonal source and receiver line with 1320 ft line spacing, resulting in an approximately 1320 by 1320 ft footprint pattern. The source and receiver intervals within the line are 220 ft resulting in a natural 110 ft by 110 bins. The periodicity of the footprint in the wavenumber then $\frac{2\pi}{\lambda_{footprint}} \approx 4.8$ radian/kft. The Nyquist wavenumber of the data is $\frac{2\pi}{\Delta x} \approx 28.6$ radian/kft and thus 6 times greater than that of the footprint along the + k_x. Given the (0,0) k_x is an over lapping element between the $+k_x$and $-k_x$, the ideal number of components is 11. Sampling the footprint significantly with less than 11 components under samples the pattern of the footprint, while sampling significantly greater than 11 times gives a comparable result at increased cost.

To illustrate the effect of the number of components, we analyze the filtered results using different components, namely 9, 49, 121 and 225. We observe a directionally proportional relationship between the number of component and smoothness of the results. We start with the nine components ($1 \leq i \leq +1$ and $-1 \leq j \leq +1$), Figure 2.11a, where we clearly observe the noise. Figure 2.11b shows the modest improvement using 49 components with significant noise present. Using a 225 components oversmooths the data and results in losing geological information, thus hindering the interpretability of the results. To link the number of components to the predicted periodicity, we consider Figure 2.12a. We show the spectrum along k_x with synthetic periodic spikes to resemble the footprint with the spectrum of wavelets superimposed for the four cases. In the 9 and 49 components case, we include more spikes than desired per wavelet spectrum which makes suppressing them more challenging. The 121-component case is optimal because we sample each spike in a wavelet and subsequently suppression more efficient. The 225-components samples it fine enough but oversmooths desired amplitude in the spike free spectrum. Figure 2.12b shows the rejected from Figure 2.11d, the amplitude of the rejected noise.

To analyze the influence of the ε, we consider the spatial trace of is at inline = 251 (Figure 2.13). We also keep the number of components fixed at 121 and vary ε = 0.01, 0.15 and 0.3. Evidently, the larger the epsilon, the higher the rejection. We notice the power of ε is critical in reducing the spikes related to the footprint noise but preserving the trend of the actual data. The choice of the optimum value is subjective to the signal to footprint ratio and the source of the noise. Although not mathematically supported, in our applications on a number of datasets with different footprint characters, marine and land data, we found 10-20% is a reasonable range for ε. This is predominantly driven by the geological features of interest with 10% for subtle features and 20%

for completely flat layers. For this data, the structure is relatively flat, and an ideal result was achieved for $\varepsilon = 0.15$.

Although the method is implemented on a slice by slice basis, we show two figures to reflect how it improves the quality on a vertical section of the data. Figure 2.14 shows the inline 251 before (2.15a) and after (15b) the footprint suppression. Figure (2.15c) shows the noise suppressed using the workflow. Although the noise appears as possible geologic collapse features in the shallow section suggesting, it does not match prior information from the area. Instead, these features are the footprint likely due to processing pitfalls and appear as quasi-hyperbolic artifacts around the reflector or variation in the amplitude along strong reflectors. The noise level reject is about 20-30% of the original amplitude. Suppressing the foot results in continuous reflectors and more acceptable geology representation. Subsequently, this allows for better automated interpretation such as auto horizon/fault pickers. The improvement in the overall quality is better seen on Figure 2.15a showing the k_x - k_y transform of the filtered slice. Compared with Figure 2.6a, we see that a lot of periodic noise magnitudes are suppressed on the transformed data. Figure 2.15b shows the edge detection attribute computed on the filtered data.

Finally, we demonstrate the efficiency of the method on a horizon slice from a megamerge survey acquired in north central Texas. This data consists of four separate surveys all shot two decades ago, three of which had east–west receiver lines and one with north–south receiver lines. The prestack gathers are contaminated with highly aliased ground roll which contributes to the severe footprint (Verma et al., 2016). The horizon considered in this example is the PaloPinto, a shallow target at (t=0.9 s) with a pronounced normal fault (Figure 2.16a). The coherence horizon is shown in Figure 2.16b; the footprint masks the subtle faults making interpreting this time

structure very challenging. Because the of the different acquisition pattern, we used 121 components and an ε =0.1. Figure 2.16c shows the same horizon extracted after applying the workflow. We clearly suppressed the noise and improved the resolution of the structural features.

Discussion and Limitation

There are multiple causes and therefore multiple expressions of acquisition footprint. Although it is not necessary to know the exact cause of the footprint, the proposed workflow assumes that the interpreter can identify its expression. If the cause is variability in the signal-to-noise ratio due to periodic changes in the number and distribution of offsets, the footprint will often be expressed by a coherence attribute. If the cause is systematic errors in velocity that result in a suboptimal NMO (or migration) correction, periodic changes in the distribution of offsets will give rise to a structural footprint, that may be expressed by a curvature attribute. Footprint associated with steeply dipping, and hence, low-apparent-frequency, migration aliasing artifacts may be characterized by a given spectral component. Improper balancing of the gathers for mutes prior to stack can lead to periodic changes in amplitude, such that the amplitude itself (or alternatively, its envelope) is an appropriate attribute for footprint characterization. Inability to identify such an attribute makes this workflow useless.

Although not discussed here, these processes can be applied to prestack migrated gathers, typically through application to one offset or azimuth volume at a time. Prior to migration, one should evaluate some type of improved trace balancing, noise suppression, or 5D interpolation.

This paper has focused on using the 2D CWT to analyze (and then attenuate) noise. The 2D CWT holds potential to characterize signal, such as the periodicity and orientation of polygonal

faulting, syneresis, joints in carbonates, cleats in coal seams, or other laterally repetitive geologic patterns. Such quantitative measurements may be then correlated to the orientation of stresses at the time of deformation or the amount of clay in the formation.

Conclusions

While the 1D continuous wavelet transform (CWT) is widely used as a seismic data analysis and data processing tool, only a limited number of geophysical applications have used the spatial 2D CWT. In this paper, we apply the 2D CWT to time slices of both a seismic amplitude and a corresponding seismic attribute volume that exacerbates footprint contamination, allowing it to be more easily characterized. By using attributes computed along structure and displayed as a time slice, rather than through a time slice through the original amplitude data, the resulting periodicity represents footprint only, rather than footprint and geology. The choice of the attribute depends on the kind of footprint. In the first legacy data from Vacuum Field in this paper, a primary cause of footprint was due to the periodicity in the collection of offsets in any given CMP, which thereby resulted in a periodic variability of the noise rejected by the stack array. This lateral variability in the signal-to-noise ratio is easily characterized by coherence. At each patch, we use the magnitude of the coherence attribute of the center (0 wavenumber) component and an appropriate threshold (ε) value to construct a 2D CWT mask that is then applied to the corresponding 2D CWT voices of the amplitude data to model the noise. This reconstructed noise is then adaptively subtracted from the original amplitude data.

In contrast to previously implemented k_x-k_y footprint characterization workflows, the 2D CWT masks applied to the data vary laterally. Lateral changes in footprint occur due to changing the weathering zone (and hence ground roll that has leaked through the stack or migration array),

to lateral changes in overlying dip, and most commonly in land data in the midcontinent USA, different acquisition designs used in multiple surveys comprising a megamerge. The efficiency of the method was demonstrated on the vintage merged data from north Texas.

We have found de-nosing using CWT to be robust and simple to use. The results of applying the workflow to 3D datasets with a strong acquisition footprint are promising. After suppression, we have improved the overall S/N, resolved structural and stratigraphic features and preserved the spatial bandwidth, resulting in subsequent attribute images that exhibit lateral changes in geology. This works as a handy tool for interpreters to enhance the quality of the signal and understand the subsurface better.

Acknowledgment

Special thanks to Marathon Oil Co. for a license to the Vacuum field survey and Clear Fork Inc. and Mull Drilling for the north central Texas seismic data. We would like to extend our gratitude to all Attributes Assisted Seismic Processing and Interpretation (AASPI) consortium sponsors for their generous support. The first author thanks Saudi Aramco for support of his Ph.D. studies.

Figures

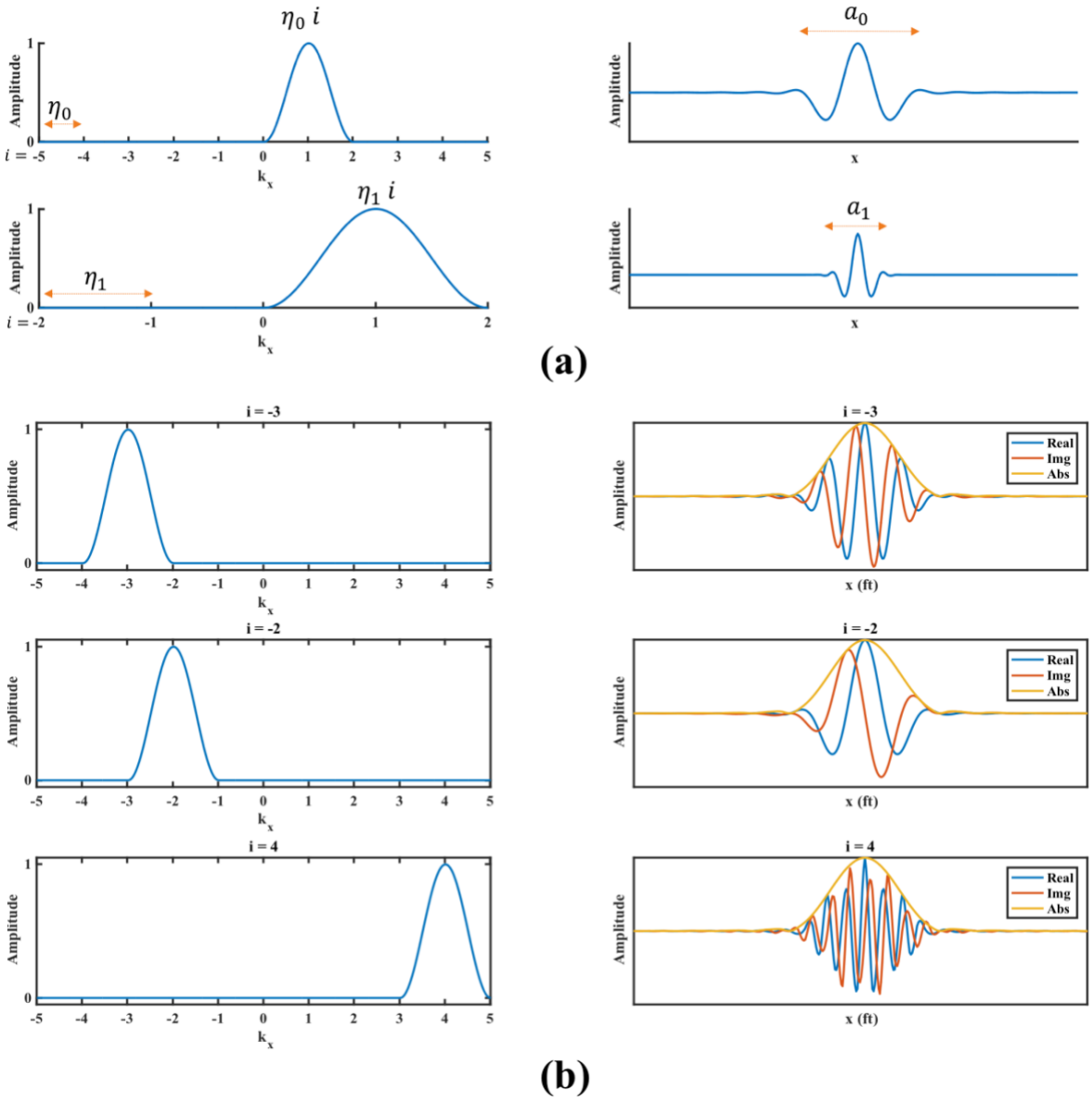

Figure 4.1a Left: the spectrum in the wavenumber domain. Right: the wavelet in the space domain. a0 and a1 are the scales of the two wavelets, i is the component number, $\boldsymbol{\eta_0}$ ***and*** $\boldsymbol{\eta_1}$ are the wavenumber shifts and $\boldsymbol{\eta_0 i}$ ***and*** $\boldsymbol{\eta_1 i}$ are the location of the components. When the scale decreases, the wavenumber spread increases and covers high wavenumbers. **2.1.b** Left, the spectrum of the wavelet in the wavenumber domain. Right: the wavelet in the space domain. We display the real, imaginary and absolute of the wavelet.

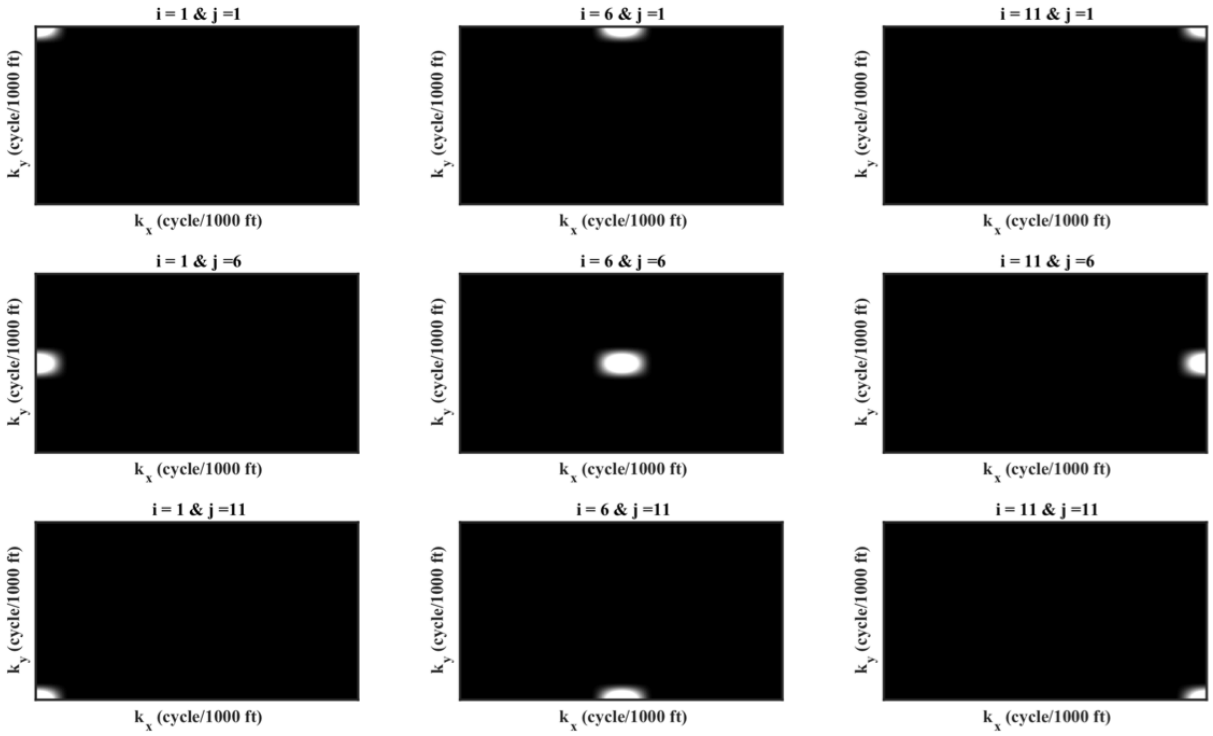

Figure 2.2. The central and eight edge wavelets of 121 in kx – ky transform.

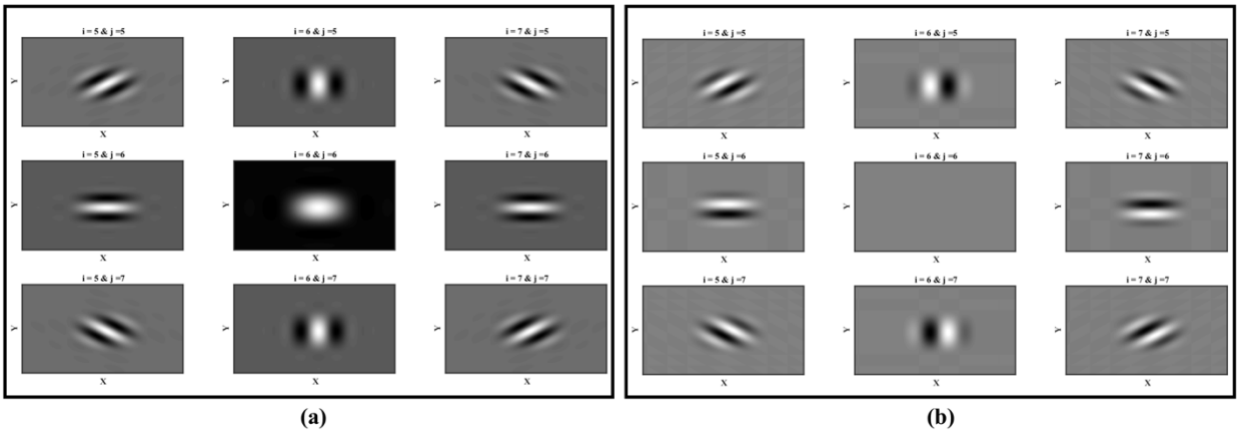

Figure 2.3. The nine central 2D wavelets of 121 in the x-y domain (a) real. (b) imaginary.

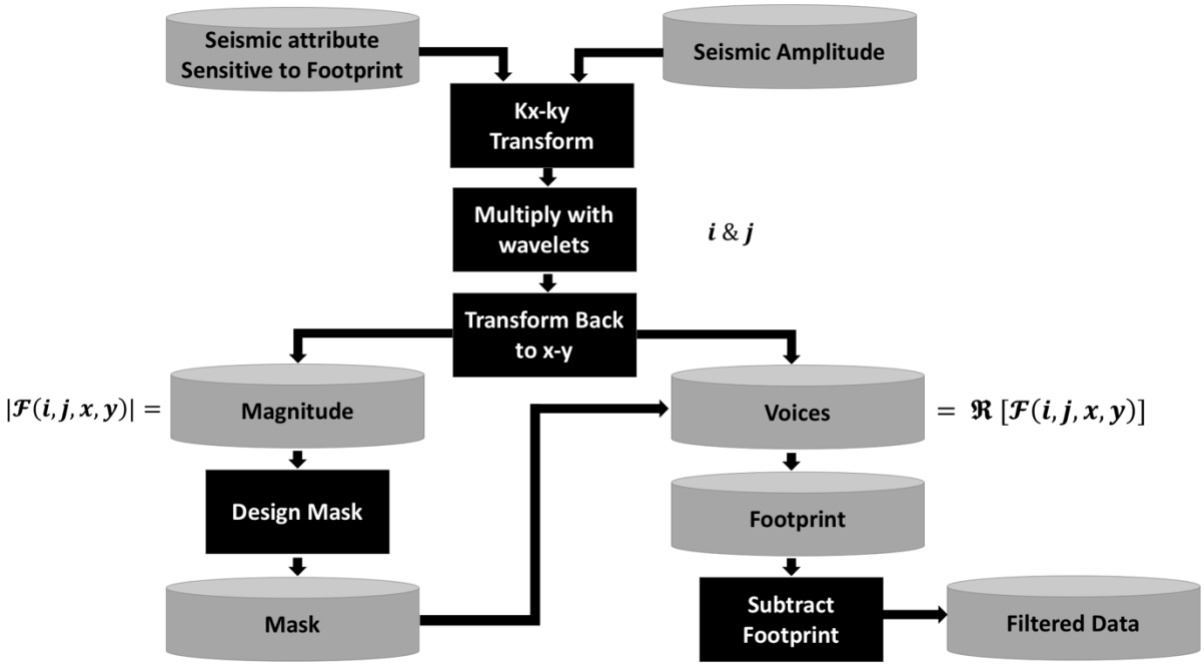

Figure 2.4. The workflow for attribute-assisted footprint suppression using CWT.

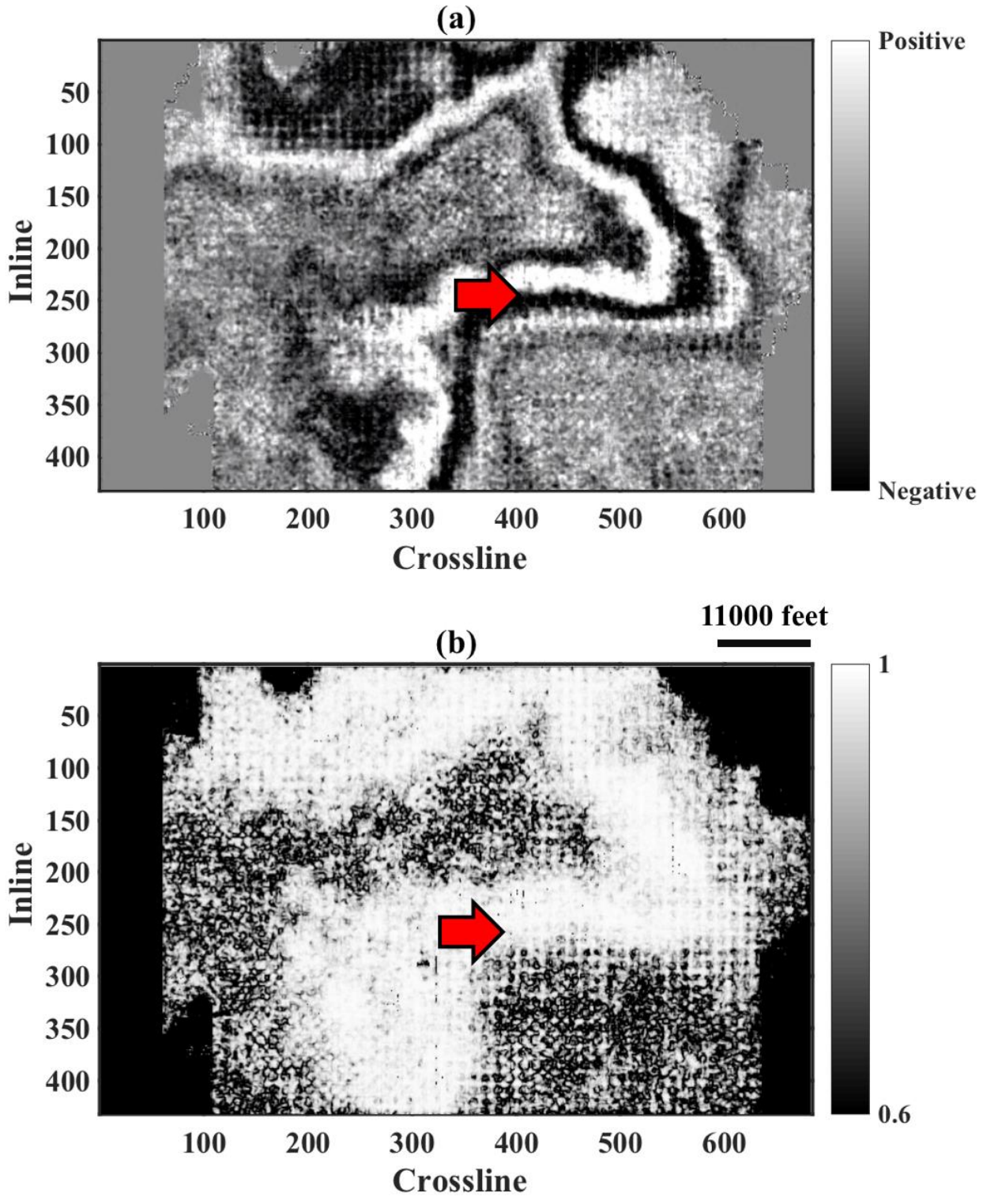

Figure 2.5. Time slice at 450 ms through (a) amplitude and (b) coherence. The red arrow indicates a high amplitude contrast that represent the slice cutting through a strong reflection on the amplitude data.

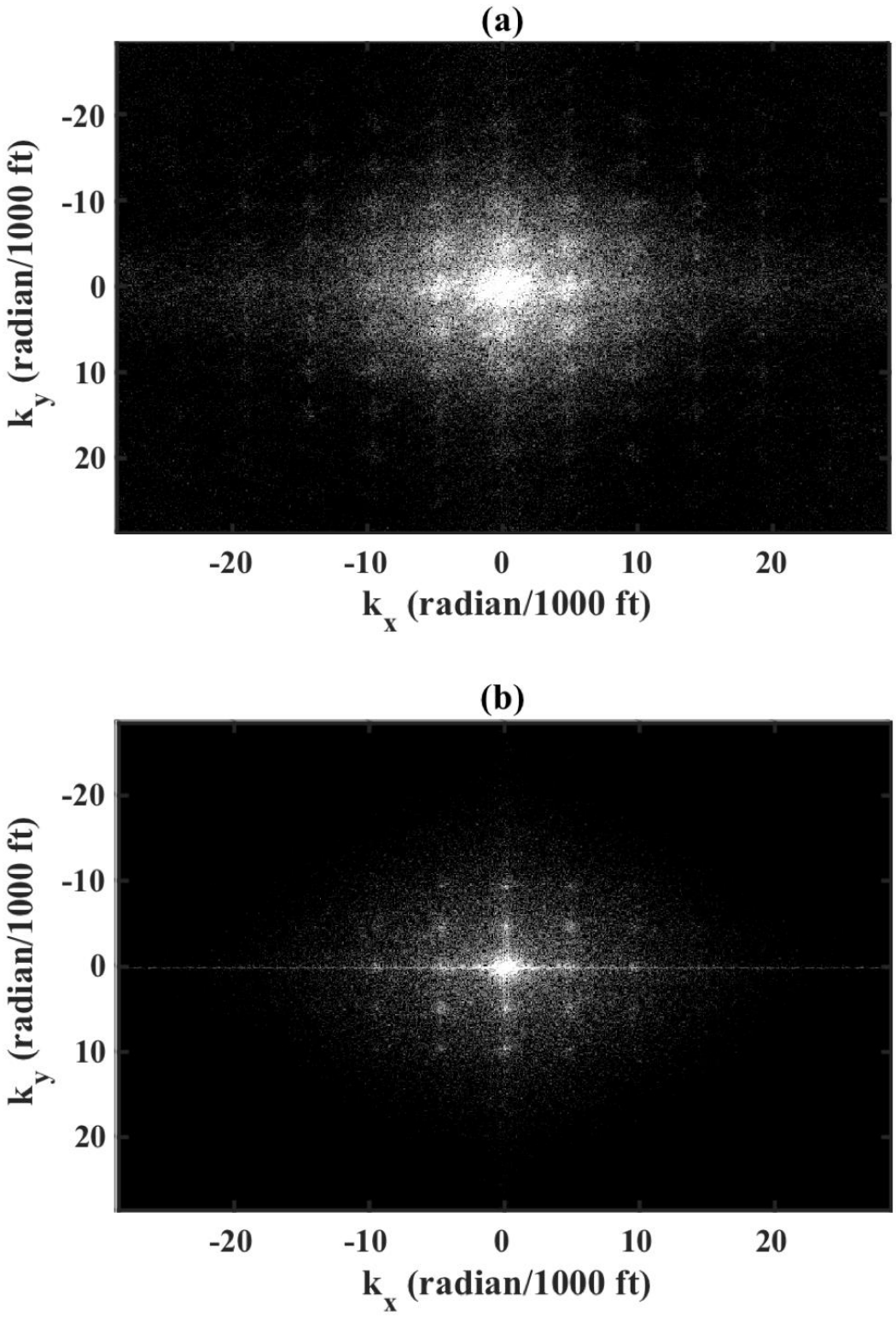

Figure 2.6. The kx - ky transform of the time slices through (a) amplitude (b) coherence shown in Figure 2.3.

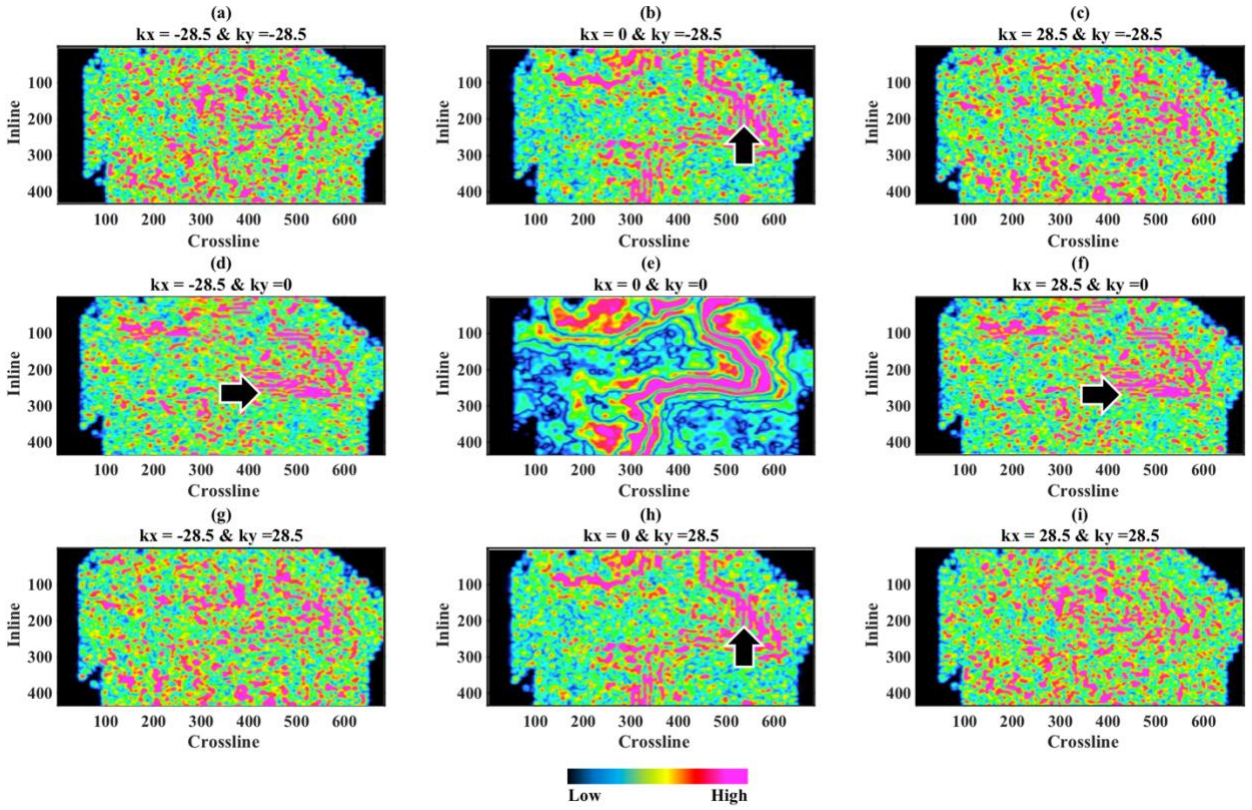

Figure 2.7. The nine central components of 121 magnitudes corresponding to the time slice shown in Figure 2.4a. The black arrows indicate the azimuthal orientation of geology leakage highlighted by the 2D wavelets.

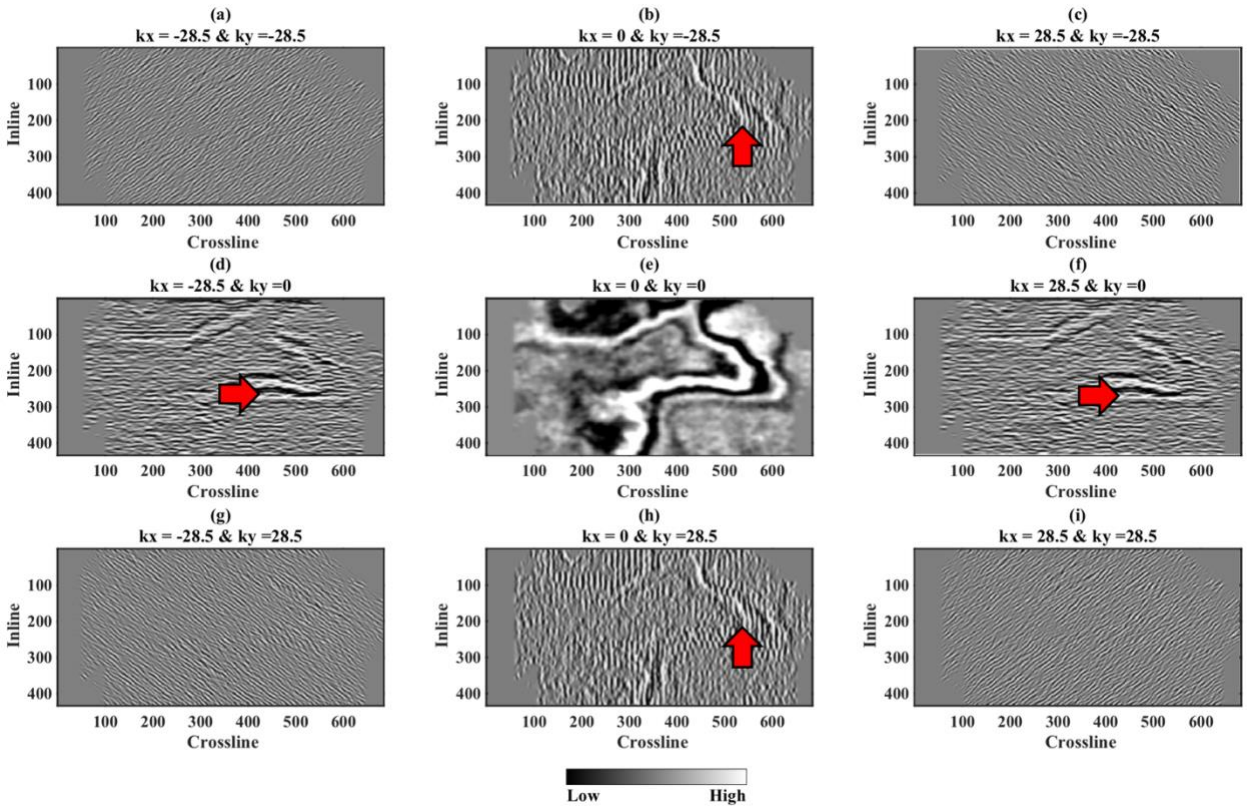

Figure 2.8. The nine central components of 121 voices corresponding to the time slice shown in Figure 2.4a. The red arrow indicates the azimuthal orientation of geology leakage highlighted by the 2D wavelets.

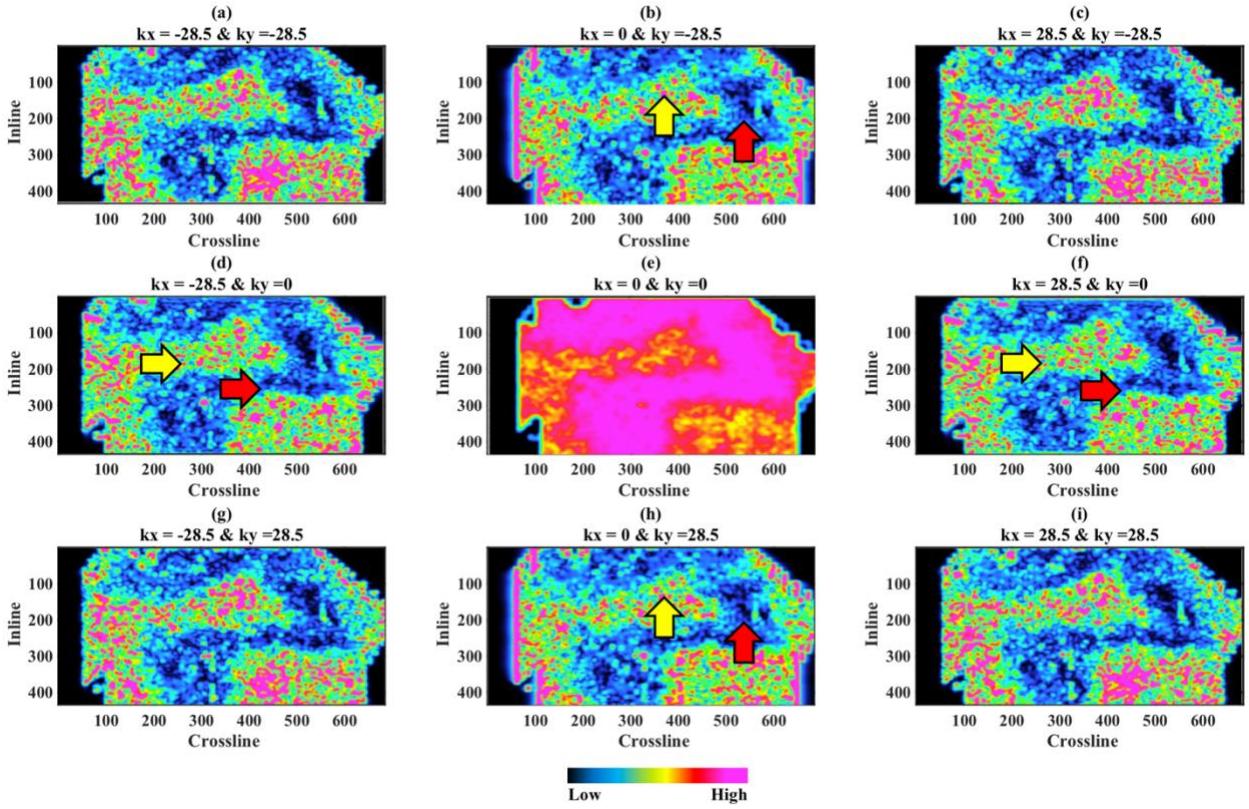

Figure 2.9. The nine central components of 121 magnitudes corresponding to the coherence slice shown in Figure 2.4b. Yellow arrows indicate areas that are contaminated by periodic events which we interpret to be footprint. Red arrows indicate areas that are less periodic and relatively footprint-free. This leads us to conclude that the magnitude of the attribute is insensitive to the geology and highly sensitive to the noise.

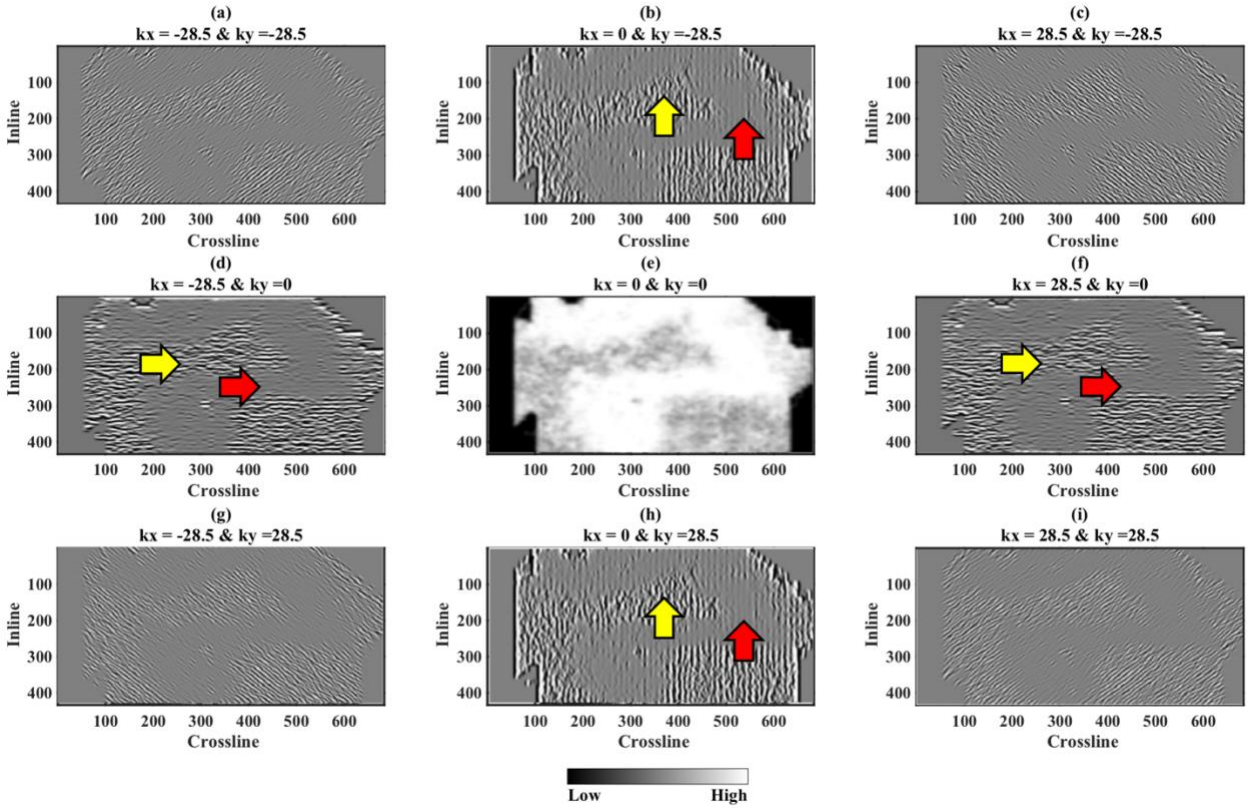

Figure 2.10. The nine central components of 121 voices corresponding to the coherence slice shown in Figure 2.4b. Red arrows indicate the absence of periodic geology. Yellow arrows indicate areas dominated by strong periodic coherence anomalies, which we interpret to be footprint**.**

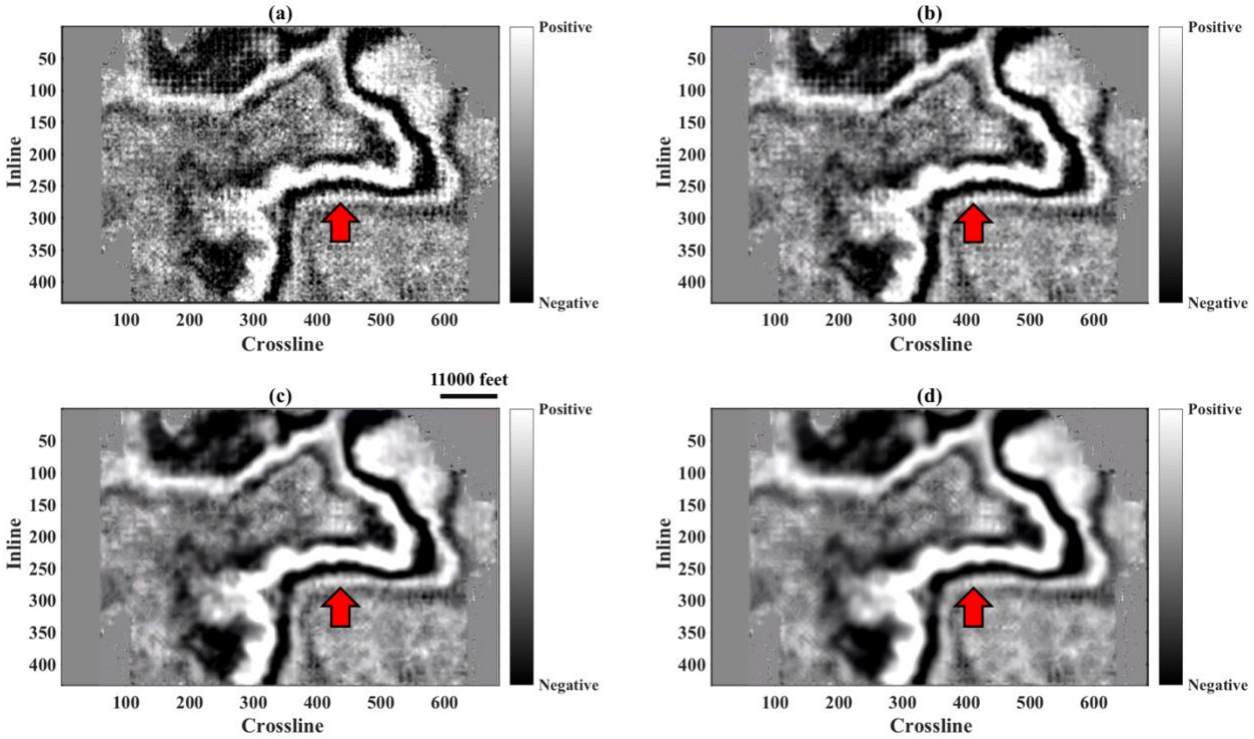

Figure 2.11. The filtered data using $\boldsymbol{\varepsilon}$ = 0.15 and (a) 9, (b) 49, (c) 121 and (d) 225 components. The rejection is directly proportional to the number of components.

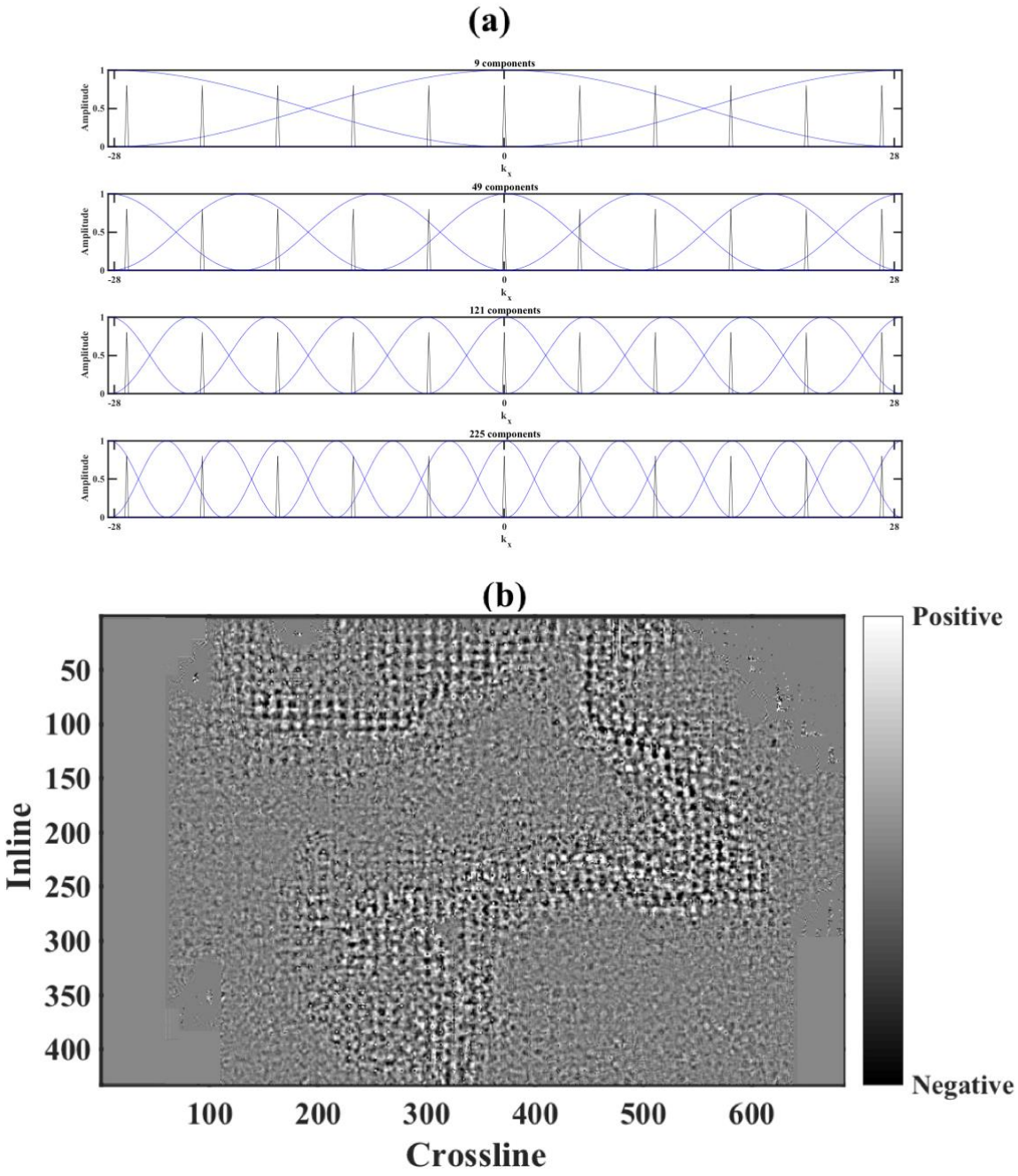

Figure 2.12. (a) The spectrum in wavenumber showing the synthetic periodic noise (black spikes) with the wavelet spectrum superimposed for 9, 49, 121, 225 components. The ideal number of components is achieved when we isolate the spike of the noise using different spectrum to allow for better adaptive subtraction. (b) The noise rejected from **Figure 2.11c,** the amplitude values used in this colorbar are 20% that of the original data.

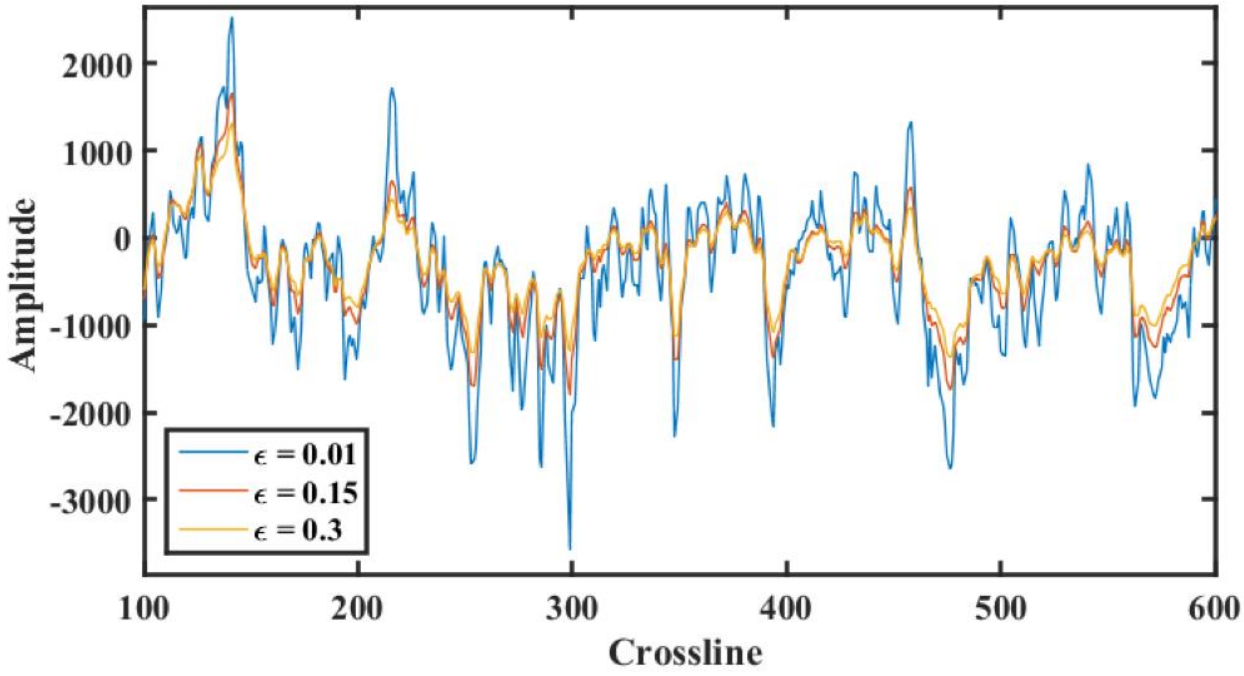

Figure 2.13. A comparison between the spatial traces at inline = 251 using a fixed 121 components and $\boldsymbol{\varepsilon}$ = 0.01, 0.15 and 0.3. The rejection is directly proportional to the value of $\boldsymbol{\varepsilon}$.

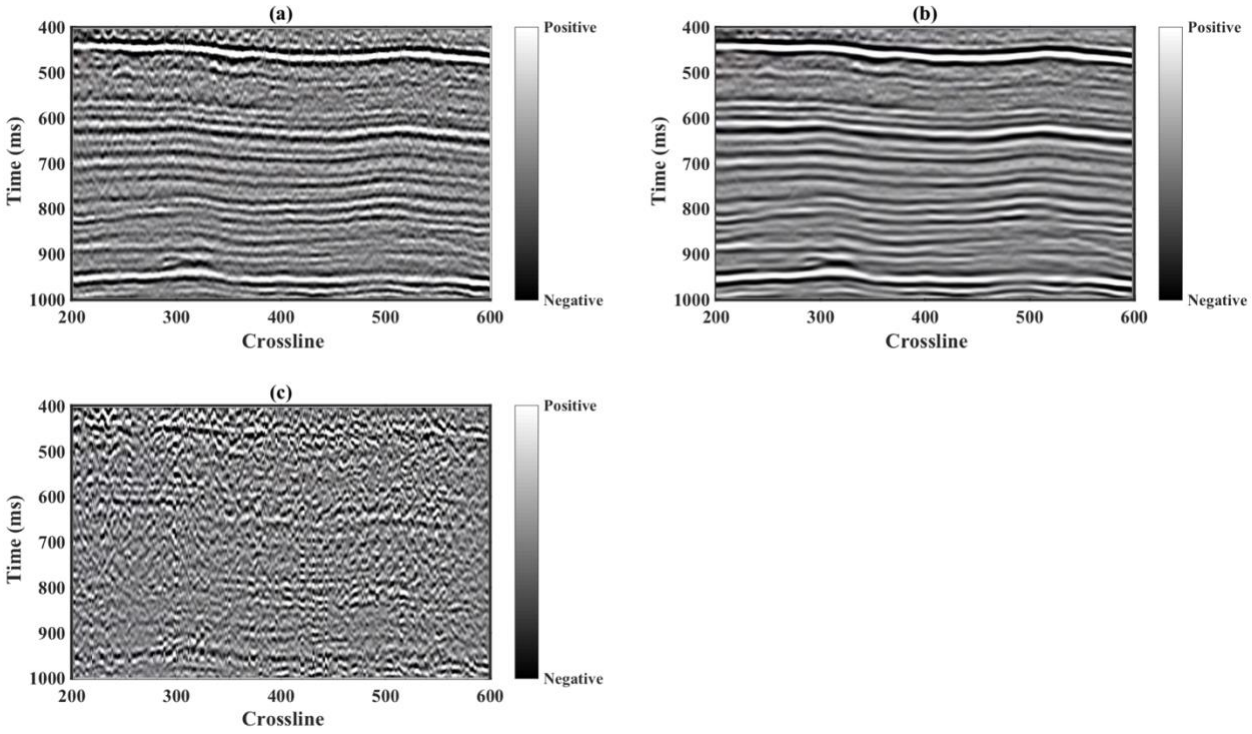

Figure 2.14. A comparison between the spatial traces at inline = 251 using a fixed 121 components and $\boldsymbol{\varepsilon}$ = 0.01, 0.15 and 0.3. The rejection is directly proportional to the value of $\boldsymbol{\varepsilon}$.

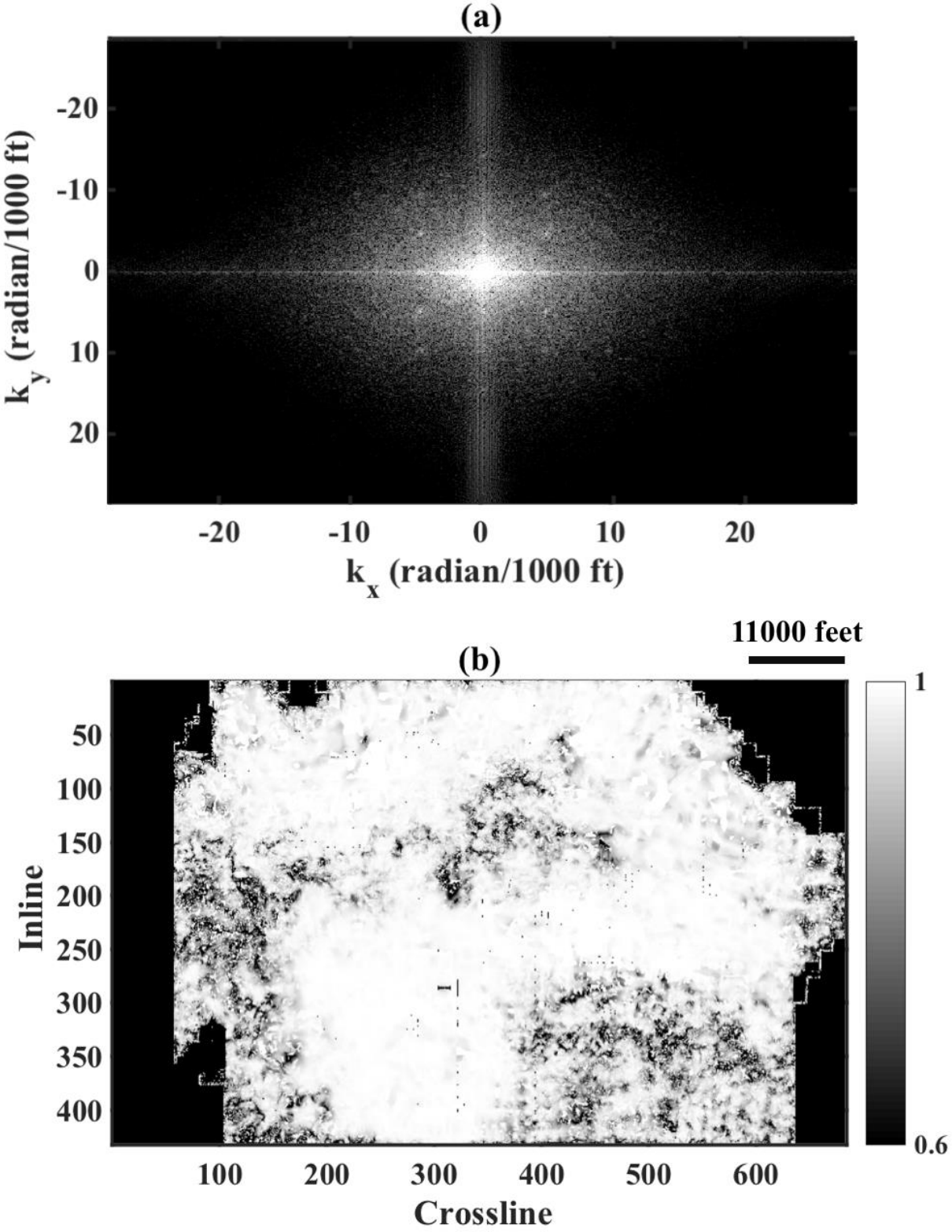

Figure 2.15. (a) kx - ky transform of the filtered data. (b) Coherence computed on the filtered data shown in Figure 2.11.c.

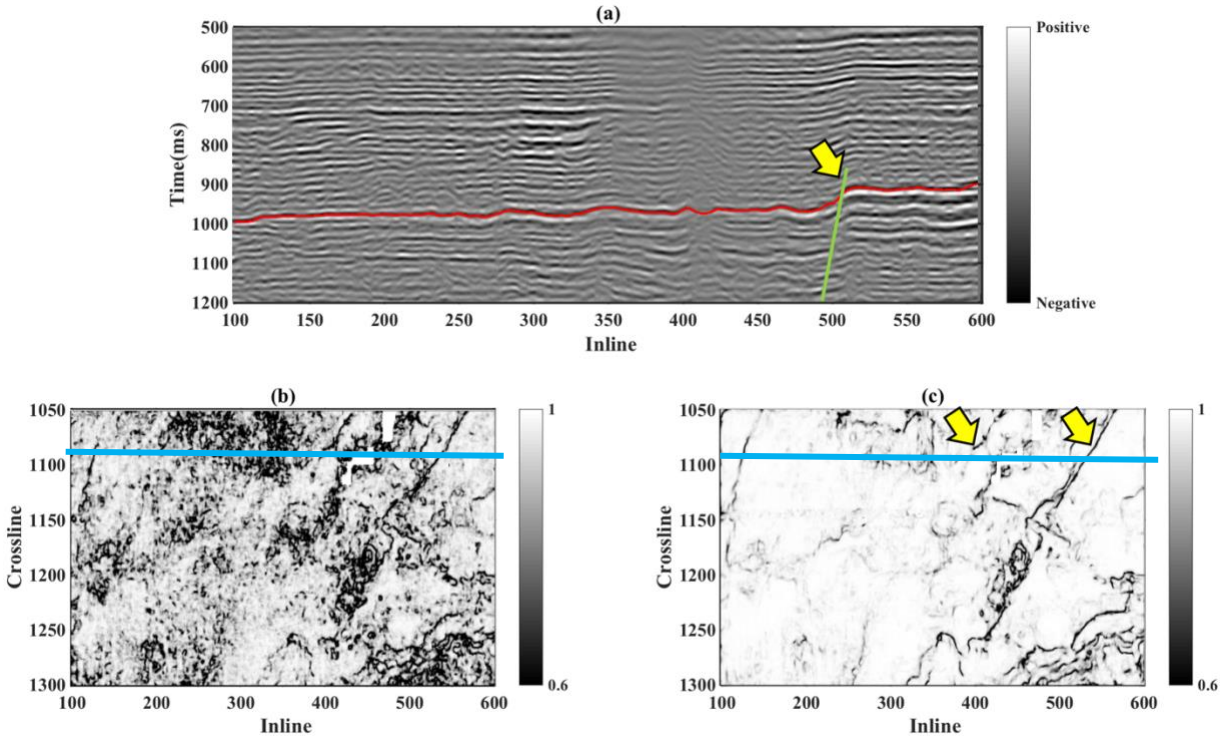

Figure 2.16. (a) crossline 1090 through the north Texas seismic data showing the top PaloPinto horizon in red. The yellow arrow indicates the fault that cuts through the horizon. (b) A horizon slice along the top PaloPinto through the coherence volume. The coherence image is contaminated with footprint noise. (c) A PaloPinto horizon slice through coherence volume computed after footprint suppression We preserve the fault and structural features, whereas the groundroll noise bursts that gave rise to organized low coherence impulse responses are now significantly reduced. The two yellow arrows indicate two faults that can be better interpreted after the noise suppression. The cyan line shows the vertical profile shown in (a).

References

Al-Bannagi, M. S., K. Fang, P. G. Kelamis, and G. Douglass, 2005, Acquisition footprint suppression via the truncated SVD technique: Case studies from Saudi Arabia: The Leading Edge, **24**, 832.

Cahoj, M. P., S. Verma, B. Hutchinson, and K. J. Marfurt, 2016, Pitfalls in seismic processing: An application of seismic modeling to investigate acquisition footprint. Interpretation, **4**, SG1-SG9

Chen, X., W. Yang, Z. He, and W. Zhong, 2012, Adaptive acquisition footprint suppression based on a 3D stationary wavelet transform: A case study from China: Journal of Applied Geophysics, **77**, 1-6.

Chopra, S., and K. J. Marfurt, 2013, Preconditioning seismic data with 5D interpolation for computing geometric attributes: The Leading Edge, 32, 1456-1460.

Cohen, L., 1995, Time-Frequency Analysis, Prentice Hall.

Davogustto, Oswaldo and K. J. Marfurt, 2011, Removing acquisition footprint from legacy data volumes: 80th Annual International Meeting, SEG, Expanded abstract, 1025-1029.

Drummond, J. M., A. J. L. Budd, and J. W. Ryan, 2000, Adapting to noisy 3D data attenuating the acquisition footprint: 70th Annual International Meeting, SEG, Expanded Abstract, 9-12.

Falconer, S., and K. J. Marfurt, 2006, Attribute-driven footprint suppression: SEG Expanded Abstracts, 2667-2671.

Goudarzi, A., M. Riahi, and M. Rabiei, 2014, Ground roll attenuation using real and complex DWT based methods: Digital Signal Processing, **42**, 67-78.

Ha, T., and Marfurt, K., 2017, The value of constrained conjugate-gradient least-squares migration in seismic inversion: Application to a fractured-basement play, Texas Panhandle: Interpretation, **5**, SN13-SN27.

Liner, C., 2010, An overview of wavelet transform concepts and applications: University of Houston, 1-17.

Mallat, S., 2009, A wavelet tour of signal processing: The sparse way, 3rd ed.: Academic Press.

Meunier, J., T. Bianchi, J. J. Poste, and R. Taylor, 2008, The future of vibroseis for high-density wide-azimuth land acquisition: First Break, **26**, 87-91.

Pranter, M. J., N. F. Hurley, T. L. Davis, M. A. Raines, and S. C. Wehner, 2004, Dual-lateral horizontal wells successfully target bypassed pay in the San Andres Formation, Vacuum field, New Mexico: AAPG Bulletin, **88**, 99-113.

Sahai, S. K., and K. A. Soofi, 2006, Use of Simple 2-D filters to reduce footprint noise in seismic data: Solutions, 14-17.

Selesnick, I., R. Baraniuk, and N. Kingsubry, 2005, The Dual-Tree Complex Wavelet Transform: IEEE Signal Processing Mag., **22**, 123-151.

Schuster, G. T., and Sun, Y., 1993, Wavelet filtering of tube and surface waves: 63rd Annual International Meeting, SEG, Expanded Abstract, 25-28.

Sheriff, R., 2002, Encyclopedic dictionary of applied geophysics, 4th ed.: SEG.

Soubaras, R., 2002, Attenuation of acquisition footprint for non-orthogonal 3D geometries: 72nd Annual International Meeting, SEG, Expanded abstract, 3-6.

Trad, D., 2009, Five-dimensional interpolation: Recovering from acquisition constraints: Geophysics, **74**, V123.

Vassiliou, M., Salvado, C. A., and Tittmann, B. R., 1984, Seismic attenuation, in Carmichael, R. C., Ed., CRC handbook of physical properties or rocks, vol. 3: CRC Press, 295–328.

Verma, S., Guo, S., and Marfurt, K., 2016, Data conditioning of legacy seismic using migration-driven 5D interpolation. Interpretation, **4**, SG31-SG40

Yu, Z., R. Abma, J. Etgen, and C. Sullivan, 2017, Attenuation of noise and simultaneous source interference using wavelet denoising: Geophysics, **82**, V179-V190.

Yu, Z. and D. Whitcombe, 2008, Seismic noise attenuation using 2D complex wavelet transform: 70th EAGE Conference & Exhibition, 9-12.

Appendix A

A Step-by-Step Description of the **aaspi_kxky_cwt_footprint_supression** workflow

The goal of the footprint suppression workflow is to generate an estimate of the footprint noise component using edge detection attribute. We subsequently adaptively subtract the modeled noise from the original unfiltered data. We show below screen captures of the GUI and introduce the different steps. We choose (1) the input amplitude data and (2) the footprint sensitive attribute.

Step 1. Slice the amplitude volume (3)

Step 2. Slice the attribute volume (4)

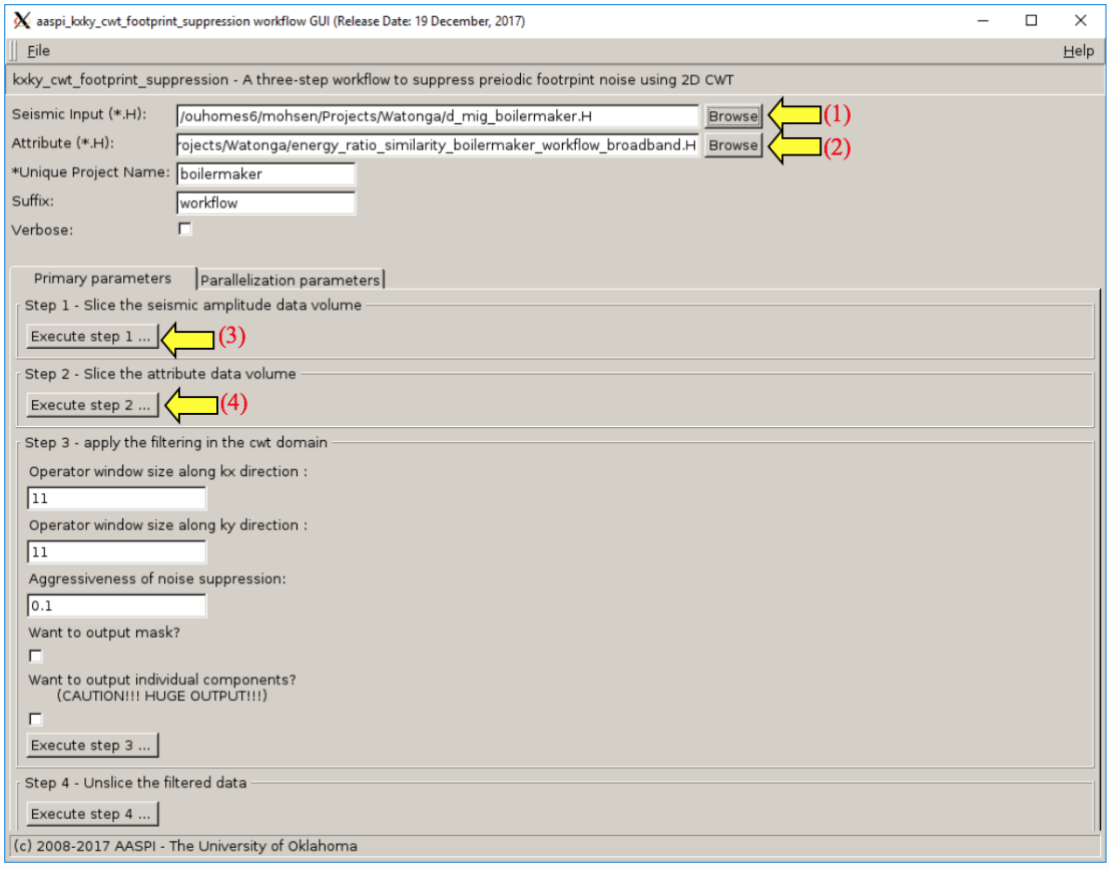

Step 3. Compute the mask using the footprint-sensitive attribute 2D CWT components to model the noise on the 2D CWT seismic attribute components. Then, inverse transform the modeled noise back to

x-y space and subtract it from the original seismic amplitude volume. This step is all done using the kxky_cwt code from the workflow. The parameters needed for these steps are:

(1) Operator window size along kx (defines the number of components along kx) (1)
(2) Operator window size along ky (defines the number of components along ky) (2)
(3) Aggressiveness of the noise suppression (3)
(4) An optional choice to output the mask for quality control (4)
(5) An optional choice to output the voices and magnitudes also for quality control (5)
(6) After selecting these values click Execute *Step 3* (6)

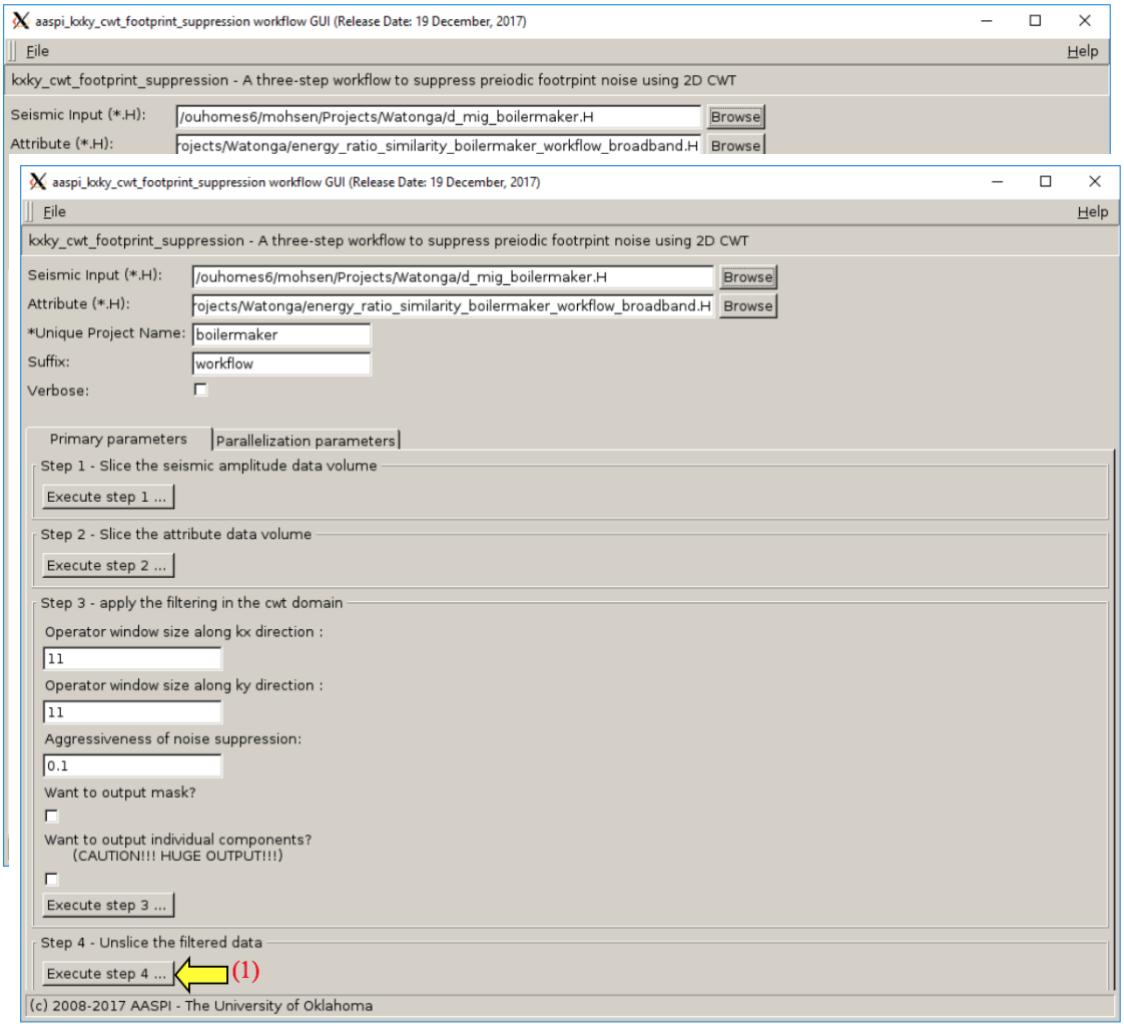

Step 4.

Unslice the filtered data to construct the filtered results. (1)

Chapter 3: Data Conditioning of a Modern Midcontintent Data Volume using POCS Five-Dimensional Interpolation

Alali, A., P. Swetal, N. Nakata and K.J. Marfurt

This paper will be submitted to the SEG journal Interpretation

Abstract

Seismic data acquisition design is subjected to variety of geophysical, operation and cost constraints. In the states like Oklahoma, where property boundaries as well as access roads generally run N-S and E-W, the most common 3D land acquisition geometry is to deploy source and receiver lines at right angles. CMP bins that fall between the two adjacent shot and two adjacent receiver lines contain a variable number of traces exhibiting different source-receiver offsets and azimuths. In the absence of obstacles, this pattern repeats, resulting in variations in fold, signal-to-noise ratio, sensitivity to velocity errors, and AVO response that is called acquisition footprint.

5D interpolation is a well-established technique that addresses these issues by regularizing the data. In general, 5D interpolation is designed to construct missing specular reflections and have been shown to improve inversion for P- and S-wave impedance. Less well documented is the impact of 5D interpolation on nonspecular diffractions needed to accurately image faults and stratigraphic edges. Obvious to seismic processors, but less obvious to interpreters, because 5D interpolation is driven by the input velocity model, it has little value in suppressing multiples where the original primary moveout velocity has been masked.

We present a case study based on a well-sampled Mississippi Lime survey acquired in NW Oklahoma, USA, where the objective was to map not only impedance anomalies indicative of more porous parts of the fractured chert reservoir but also to map subtle faults that may cause a horizontal well to leave the target zone. The original 200-fold data provide good fault images but suffer from acquisition footprint and other noise. Footprint and noise artifacts contaminate subsequent prestack inversion. We use a commercial Fourier transform based interpolation technique Projection onto Convex Sets (POCS) to construct an interpolated 800-fold data volume

and find footprint to be suppressed and lateral continuity of prestack inversion images improved. However, fault and karst edges at the target Mississippian horizon and a channel at the shallower Marmaton horizon have been significantly attenuated. We therefore recommend interpreters who use such technology to request both volumes from their processor – using the original data to define structural and stratigraphic edges, and the interpolated data for inversion for rock properties.

Introduction

5D interpolation is applied routinely in seismic data processing with the purpose of reducing migration operator aliasing artifacts, suppressing acquisition footprint, and suppressing random noise. Ideally, seismic data are acquired on a grid; if we sort the data by offset-azimuth sectors, the traces in a given bin will be irregular. Seismic data regularization can be divided into two categories, the first category relies on wave-equation-based methods to reconstruct the data using the wavefield velocity. The second category is based on signal processing techniques where a transform such as Fourier, Radon or curvelet transform is used to reconstruct the data. Numerous applications in previous studies have demonstrated the advantages of 5D interpolation. Verma et al. (2015) used a (wave equation) migration-based 5D interpolation on a legacy data from Texas to increase the fold and carry better quantitative interpretation. Downton et al. (2008) used 5D interpolation to address inadequate sampling and showed that it preserves the amplitude and improves AVO analyses. Chopra and Marfurt (2013) demonstrated the value of interpolation in filling gaps of source or/and receiver spacing, reducing acquisition footprint, and improving geometrical attribute quality. Barnes et al. (2013) applied amplitude-preserving interpolation to regularize marine data prior to Kirchhoff depth migration.

The most common signal processing interpolations methods are Fourier transform based and have become the standard in commercial software. The comparison of the details of each method is beyond the scope of this paper; rather, we simply list the most common Fourier transform based algorithms and their main properties.

The first group relies on the Discrete Fourier transform (DFT) and requires annulus sector binning prior to interpolation. This binning process is not associated with the geometry and is used to bin the data on a regular grid in order to compute the DFT. The DFT-based algorithms are computationally fast but can introduce errors due to the annulus sector binning. The Minimum Weighted Norm Interpolation (MWNI) (Liu and Sacchi, 2004, Trad, 2009) algorithm preserves amplitude and can interpolate spatially sparse data. It has a drawback of introducing artifacts when the number of iterations is not accurately chosen. Another technique is Projection onto Convex Sets (POCS) (Abma and Kabir, 2006), which utilizes a 4D Fourier transforms in space (receiver-space and source-space) for each frequency slice. By applying a threshold only, the higher magnitude components are kept, after which the data are inverse Fourier transformed spatially. POCS requires more iterations than MWNI and creates more artifacts for data with large gaps (Pan and Schlosser, 2013). On the other hand, POCS is less sensitive to the number of iterations than MWNI (Pan and Schlosser, 2013). The second group of techniques relies on a Non-Discrete Fourier Transform (NDFT) and does not require annulus sector binning before interpolation such as Anti-Leakage Fourier Transform reconstruction (Xu et al., 2005). NDFT is computationally intensive because it reconstructs each wavenumber separately but can accurately handle narrow azimuth marine data. NDFT can interpolate at any location and does not suffer from the binning issues observed in the first group. Finally, and more recently, hybrid approaches have been

implemented which apply regular grids with an additional interpolation to minimize binning error helping the far offsets (Jin, 2010; Wang and Wan, 2013, Pan and Schlosser, 2013).

To assess the artifacts and validity of the 5D interpolation algorithm, Cary and Perz (2012) used the newly interpolated traces to reconstruct the input traces. They compared the newly generated traces with the original and confirmed that subtle geological features such as diffractions are not interpolated properly. This workflow serves as a measure of energy leakage in the 5D interpolation process and can be used to assess the output of any 5D interpolation algorithm.

Perry (2017) demonstrated on his Red Fork case study that 5D interpolation attenuated geometrical structures such as faults and channels. The objective of his work was amplitude enhancement and found that 5D interpolation provided superior prestack inversion results. However, he was surprised that 5D interpolation degraded the fault and channel images mapped by coherence attributes. The underlying cause of this degradation and those observed by Chopra and Marfurt (2013) motivates this study. The objective of this study is to examine the advantages and disadvantages of 5D POCS interpolation on a land seismic data from northwestern Oklahoma. In particular, we are interested in understanding issues associated with suppressing subtle geometric features after 5D interpolation. Fractures and drilling zones of interest are often associated with karst (Milad and Slatt, 2017). The paper is structured as follows: We begin with a synthetic model to illustrate the mechanics of the 5D POCS algorithm and how it handles specular and nonspecular scattered events. Next, we summarize the background geology of the area of interest, after which we describe the data acquisition and processing workflow leading up to the interpolation. We present our choice of interpolation method for this dataset and examine the influence on velocity picking, imaging and geometrical attributes. Finally, we apply model-

based post stack acoustic inversion on both datasets and summarize the advantages and limitations using POCS interpolation.

A Simple Model of Specular and Nonspecular events

5D interpolation affects both specular events such as reflection and nonspecular events such as diffraction. To illustrate the effect of normal moveout (NMO) on diffraction and the sensitivity of interpolation to the annulus sector binning, we construct a 3D model with a vertical fault as a diffraction generator (Figure 3.1a). Diffractions in theory are sensitive to small scale such as faults, channels and karst features (Rauch-Davies et al. 2014; Decker, 2014). We use a 15 Hz peak frequency Ricker wavelet as the source, a Δx=Δz=5 ft grid size and 101 receivers in the inline and crossline direction with a receiver spacing of 40 ft. We propagate the source using a finite difference acoustic modeling algorithm and bin the data on a 151 x 151 grid resulting in a maximum fold of 9. Figure 3.1b shows seven NMO-corrected CMPs. By construction, POCS interpolation algorithm involves filtering lower amplitude wavenumbers in the Fourier domain and hence can introduce undesired energy in the time domain. To enhance the viewing of the result, we added 10% Gaussian noise and show the same CMPs in Figure 3.1c. To mimic the inconsistent sampling problem in real data problem, we mute four sources and show the same CMPs in Figure 3.1d. The stacks of both regular and decimated data are shown in 3.1e and 3.1f. Applying NMO using the correct RMS velocity accurately flattens the reflector but results in residual moveout on the diffraction (red arrows). This is due to the fact that diffractions have a longer travel time than the reflection. Also, the underlying assumption of 5D interpolation is that missing traces look like adjacent traces. This assumption has shortcomings in areas with different travel times events. We feed the decimated data into a commercial POCS algorithm to reconstruct the missing traces using

the following annulus sector bins: $\Delta\varphi$=45° by Δh=80 ft (Figure 3.1g) and $\Delta\varphi$=45° by Δh=100 ft (Figure 3.1h). Visualizing the CMPs shows that the data reconstructed has different characteristic for the deeper reflection (red arrow). The different can be explained by the bias due to the anulus sector bin used. To better analyze the effect of the interpolation, we stack the interpolated data using different annulus sector bins to evaluate the effect it has on constructing a seismic image. In Figure 3.1i we use $\Delta\varphi$=90° and Δh=750 ft offset, note the specular reflection in this simple model not well constructed (green arrows) and the diffraction (red arrow) is suppressed. In Figure 3.1j we use $\Delta\varphi$=45° and Δh=100 ft sector bin which results in a better specular reflection constructing with minor artifact but suppresses the nonspecular energy completely (red arrow). Finally, we show the results for $\Delta\varphi$=45° and Δh=80 offsets sector bins. We successfully construct the energy of the specular energy and partly construct the diffraction with minor artifacts. In general, coarse annulus sector binning affects both reflection and diffraction. In particular, diffractions are more susceptible and tend to be the first feature of the data to be affected. The sampling differences between the original and 5D interpolation in offset and azimuth could easily account for some of the differences in the diffractions and flat events that we see in Figure 3.1i-j. Processors should get into the habit of testing different annulus sector bins to ensure the features of interest are preserved.

Geological Background

The data used in this study were acquired by Chesapeake Energy to image a "Mississippi Lime" play in northwest Oklahoma. The “Mississippi Lime” is a loose term that represents a heterogeneous package of tight limestone, siliceous limestone, and fractured chert. The reservoir is complex with most porosity being fracture porosity with most of the fractures being shrinkage (diagenetic) rather than tectonic fractures. The original siliceous limestone was deposited during

the Mississippian and then tectonically uplifted in the early Pennsylvanian leading to periodic subaerial exposure and erosion, as well as post-depositional alteration. This complex geologic journey has led to a significant lateral and vertical heterogeneity and compartmentalization within Mississippian formation (Montgomery et al., 1998). The main four electrofacies proposed by Lindzey (2015) are high-porosity tripolite, chert, fractured tight chert, and tight limestone.

The structure in this area is relativity flat with one major fault that trends roughly northeast to southwest across the survey with the downthrown block to the south. The offset of the fault varies across the area with the maximum offset at 100 ft and the fault (Lindzey, 2015). The target of the survey is relatively shallow, ranging between 5000 to 5300 ft and 800-850 ms.

The Mississippian Limestone play has been drilled vertically with significant success over the past century. Intensive horizontal drilling started in 2007 followed by unconventional exploration which renewed the interest of this play over the past decade. Between 2011-2014, the production saw a jump from 50,000 bbl/day to 300,000 bbl/day.

Seismic Data Acquisition and Processing

The seismic data in this study cover 44 km^2 using the orthogonal acquisition pattern shown in Figure 3.2a. Twenty-six receiver-lines with a line spacing of 440 ft were active for each shot with a 220 ft receiver spacing. The source-line spacing is 880 ft with 220 ft source interval. This acquisition pattern produces a maximum nominal fold of 220. The maximum offset is 14,000 ft in the E-W direction and half that offset in the N-S direction. Figure 3.2b shows a representative spider plot for this survey.

The data quality is hindered by the presence of ground roll that can be linked to a shallow gypsum layer. This layer extends from the north of Oklahoma to the south of Kansas (Suneson 1998), evident by the presence of one of the largest gypsum caves, publicly accessible, close to this survey. We process the data using a conventional workflow starting with trace editing followed by relative amplitude scaling and surface consistent deconvolution. Next, we apply linear noise suppression. Refraction statics precede velocity analysis and surface consistent residual statics. Due to the fairly regular acquisition in our survey with few gaps, we chose POCS 5D interpolation technique using commercial software prior to migration velocity analysis. POCS is widely used in signal and image reconstruction. The main controlling factors for this technique are the annulus sector binning, the number of missing seismic traces and the threshold used to reject the low amplitudes wavenumber (Zi-Jian et al., 2015). POCS requires at least half the traces to be live in the input gather (Pan and Schlosser, 2013). We interpolated the data along the azimuth and offset axes using $\Delta\varphi$=45°and Δh=660 ft bins. The objective of this interpolation is to enhance the coherent signal and suppress the acquisition footprint whilst preserving the geology. Figure 3.3a and 3.3b shows the fold map of the data before and after 5D interpolation resulting in an average increase in fold by a factor of 4. Figure 3.3c shows the spider plot for the same CMP shown in Figure 3.2b after 5D interpolation.

Effect on Migration and Geometric Attributes

To compare the two datasets, we first consider the effect of 5D interpolation on the velocity analysis. The velocity semblance is constructed by combining a number of CMP's that lie close together to form a super-gather. The data quality and offset coverage dictates how many CMPs are used in the super-gather. For these data, we used 7 by 7 bins (or 49) CMPs to construct a

supergather for semblance-based velocity analysis. In fact, one may consider the super-gathers as a crude form of interpolation where we rely on adjacent CMPs to provide denser offset coverage. The advantage of 5D interpolation over super-gathers is that the it uses higher dimensions to interpolate. Figure 3.4 show the velocity semblance for a super-gather computed using the data with and without 5D interpolation. The interpolated data improves the velocity semblance resolution in the shallow section, resulting in more continuous reflectors on the interpolated gather. The zone of interest is highlighted with the yellow box on both datasets. At the zone of interest, a significant improvement is achieved in the far offset which gives a clearer semblance. The deeper section on both Figure 3.4a and 3.4b is contaminated by the multiples due to the carbonate layering in the zone of interest. Because of the improvement seen on the interpolated data, we used it to pick the migration velocity.

Unfortunately, if we picked multiples below the top of the basement (below the yellow box), the continuity of these vents will be also improved. The data beyond the muted zone (red dashed line in a) have been extrapolated and the result in the far offset may be inaccurate. Such extrapolation may result in an image that is highly prejudiced by the initial picked velocity. We show a CMP before and after interpolation to verify the effect of interpolation on the far offset in Figure 3.5. To reduce the effect of the interpolated data, a harsh mute is applied after migration to suppress all the artificial events created in the far offset.

There are two pitfalls in this model-driven workflow. First, if we assume our model to be one of hyperbolic moveout, weaker, far offset nonhyperbolic moveout traces may be misinterpolated or perhaps extrapolated based on the higher amplitude near traces (Figure 3.5). Second, if it is difficult to pick an accurate velocity due to strong multiples (such as below the

basement at t=1.2 s in this data volume), then we will preferentially interpolate and enhance multiples rather than the weaker primaries.

Figure 3.6 shows line AA' through the stacked data volume after prestack Kirchhoff time migration for both data sets in Figure 3.6 using the velocity picked on the interpolated data. The Mississippian top appears as a broad peak on the seismic data that can be difficult to pick in certain areas (Lindzey, 2015). We observe a more balanced amplitude after the interpolation (Figure 3.6b) which can be linked to the reduction in footprint. In addition, the fault is clearer on the interpolated section (green arrow). For that reason, the balanced amplitude is more desired for automatic pickers. This is also a product of the higher fold generated by the interpolation

The third comparison is on seismic geometrical attributes. The vertical resolution is defined as a quarter wavelength of the data. We computed coherence on the original dataset and extracted horizons slices along the Marmaton and Mississippian formation in Figure 3.7. Both slices show both random and coherent noise. Other techniques in the literature such as SOF (Zhang et al., 2016a) and radial trace time frequency peak filtering using Hurst exponent statics (Zhang et al., 2016b) can reduce the random and coherent noise. Also, separate techniques also exist in the literature to suppress footprint such as those described by AlAli et al. (2018) and Galibert et al. (2002); however, they offer no data regularization. Coherent noise such as footprint is more difficult to predict by interpolation as they mask in with the signal. Interpolating without distinguishing the two could indeed result in distorting coherent signal amplitude. Trad (2014) acknowledged that applying normal moveout (NMO) prior to interpolating the data simplifies the task by reducing the wavenumber bandwidth (and aliasing) in the offset direction and reducing the binning error. Applying NMO allows the interpolation to preserve the coherent signal and suppress

the footprint. Figure 3.8 shows the same two horizon slices extracted from the coherence volume after 5D interpolation. Both slices show less acquisition related noise. The channel edges seen in Figure 3.8a are suppressed after the interpolation. The Mississippi Lime horizon slice shows a clearer image and a slimmer fault.

The ability of 5D interpolation to enhance the reflections and preserve subtle features such as faults, diffraction and fractures is crucial. The challenge for 5D interpolation parameterization is in defining the appropriate annulus sector binning to approximate the diffraction wavenumbers properly. Such sensitivity is more of an issue for data located close to the borders of the survey, particularly at shallow times or far offsets because of decrease in the number of live samples.

Effect on P- Impedance

To further evaluate the impact of seismic data interpolation, we performed model-driven acoustic impedance inversion on the data before and after 5D interpolation. A total of four wells are available for this survey with P-wave logs and density. Perry (2017) demonstrated how 5D interpolated and spectral balancing together can improve the P-impedance compared with the original data. Figure 3.9 shows horizon slices along the top Mississippi lime through the regular and 5D interpolated volumes. Both slices show similar overall trends. The linear features shown by black arrows in Figure 3.9a are artefacts that correspond to acquisition footprint seen on the original amplitude data. 5D interpolation suppress the footprint noise and hence, in the impedance we have a much smoother variation of P-impedance.

Figure 3.10a and 10b shows coherence co-rendered with P-impedance for the original and 5D interpolated data respectively. Lindzey (2015) indicated that the downthrown block shows a

broader peak in the at the top of the Mississippian immediately south of the fault compared to the north of the fault. She concluded that is due to result of the abundance of chert conglomerate transported from the upthrown (red arrow) block down to the downthrown block (white arrow). Both slices show similar trends with a more pronounced low impedance on the 5D interpolated data.

Finally, we show the impedance slice through the same horizon with the coherence computed on the original data for comparison. The structurally governed impedances changes are imaged better in Figure 3.11 than in Figure 3.10a and 10b. Such an analysis make sense, since with the original coherence we can preserve all the structural features and with 5D interpolated P-impedance we are able to suppress all the footprint noise and its effect on impedance.

Conclusions

For economic reasons, most seismic surveys are acquired on coarse grids which gives rise to acquisition footprint. This limitation can degrade the quality of the data and affects semblance-based velocity analysis, geometrical attributes and amplitude preservation. In the midcontinent of the USA, 5D interpolation methods have become a well-accepted part of the seismic processing workflow that helps suppress acquisition footprint and improves specular reflections for impedance inversion. Although regularized seismic data yields a better signal-to-noise ratio and better AVO analysis, one must be aware of the inherent limitations of the method due to parameters settings and the nature of the features being interpolated. We have demonstrated using POSC interpolation algorithm on an Oklahoma Mississippi Lime dataset that subtle features can be damaged at the expense of improving the amplitude analysis. We attribute the loss of “edges” in the seismic images using the traditional Fourier transform based 5D interpolation techniques to

the error introduced due to the annulus sector binning, and inherent NMO correction. All these factors could lead to the lack of low-amplitude wavenumber needed to construct subtle features such as diffraction and which are of importance to interpreters. In our analysis we found that computing geometrical attributes on original interpolated seismic data gives better results whereas impedance is better computed on 5D interpolated data. We recommend that interpreters request data volumes with and without interpolation to construct a more detailed image of the subsurface.

Acknowledgments

We would like to thank our AASPI sponsors for their support and in particular Chesapeake Energy for their permission to work on this dataset. Special thanks to Landmark, HampsonRussell and Schlumberger for providing the licenses needed to carry this study. The first author would like to thank Saudi Aramco for sponsoring his studies.

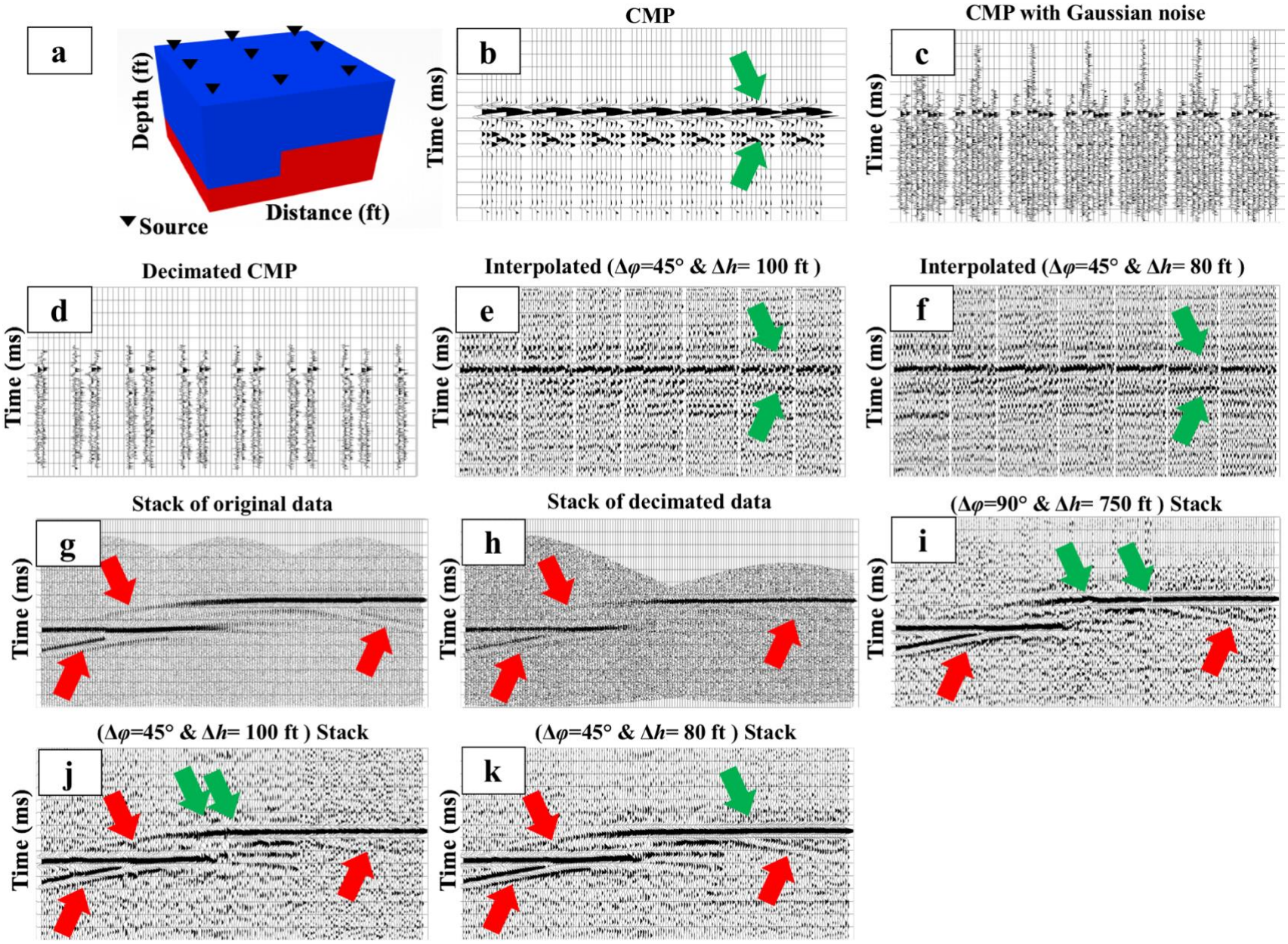
a
Depth (ft)
Distance (ft)
Source
CMP
b
Time (ms)
CMP with Gaussian noise
c
Time (ms)
Decimated CMP
d
Time (ms)
Interpolated (Δφ=45° & Δh= 100 ft)
e
Time (ms)
Interpolated (Δφ=45° & Δh= 80 ft)
f
Time (ms)
Stack of original data
g
Time (ms)
Stack of decimated data
h
Time (ms)
(Δφ=90° & Δh= 750 ft) Stack
i
Time (ms)
(Δφ=45° & Δh= 100 ft) Stack
j
Time (ms)
(Δφ=45° & Δh= 80 ft) Stack
k
Time (ms)

Figure 3.1. (a) Model of a faulted reflector in depth. (b) 7 CMPs after NMO correction using the correct velocity. Red arrows indicate unfocussed diffraction events. (c) same CPDs in (b) after adding gaussian noise 10% of the amplitude. (d) CMPs in (c) after decimation. We muted 4 out of the possible 9 sources in the modeled data. (e) Stacked original data. (f) Stacked data after decimation. Red arrows indicate areas where we can see residual moveout on the diffraction. Also, note how the strength of the diffraction is different between two stacks are different due to decimation. The edge of the top diffractor is shorter. CMPs after POCS interpolation using the annulus sectors bins measuring $\Delta\varphi$=45° and Δh= 80 ft (g) and $\Delta\varphi$=45° and Δh=100 ft (h). The number of traces per CMP depends on the annulus sector bin size. In this figure we illustrate the remnant moveout on the diffraction after NMO and express the importance of annulus sector binning prior to interpolation. To better illustrate the result, we show the stacks due to different annulus binning in figures (i) $\Delta\varphi$=90° and Δh= 750 ft (j) $\Delta\varphi$=45° and Δh= 80 ft (k) $\Delta\varphi$=45° and Δh= 80 ft. The specular reflection energy is not properly constructed due to the in appropriate annulus sector binning (green arrows). (k) give the best binning to enhance the specular reflection. Red arrows show areas where the nonspecular energy is not is not constructed. With this minor change and after 3D stacking subtle features may get suppressed.

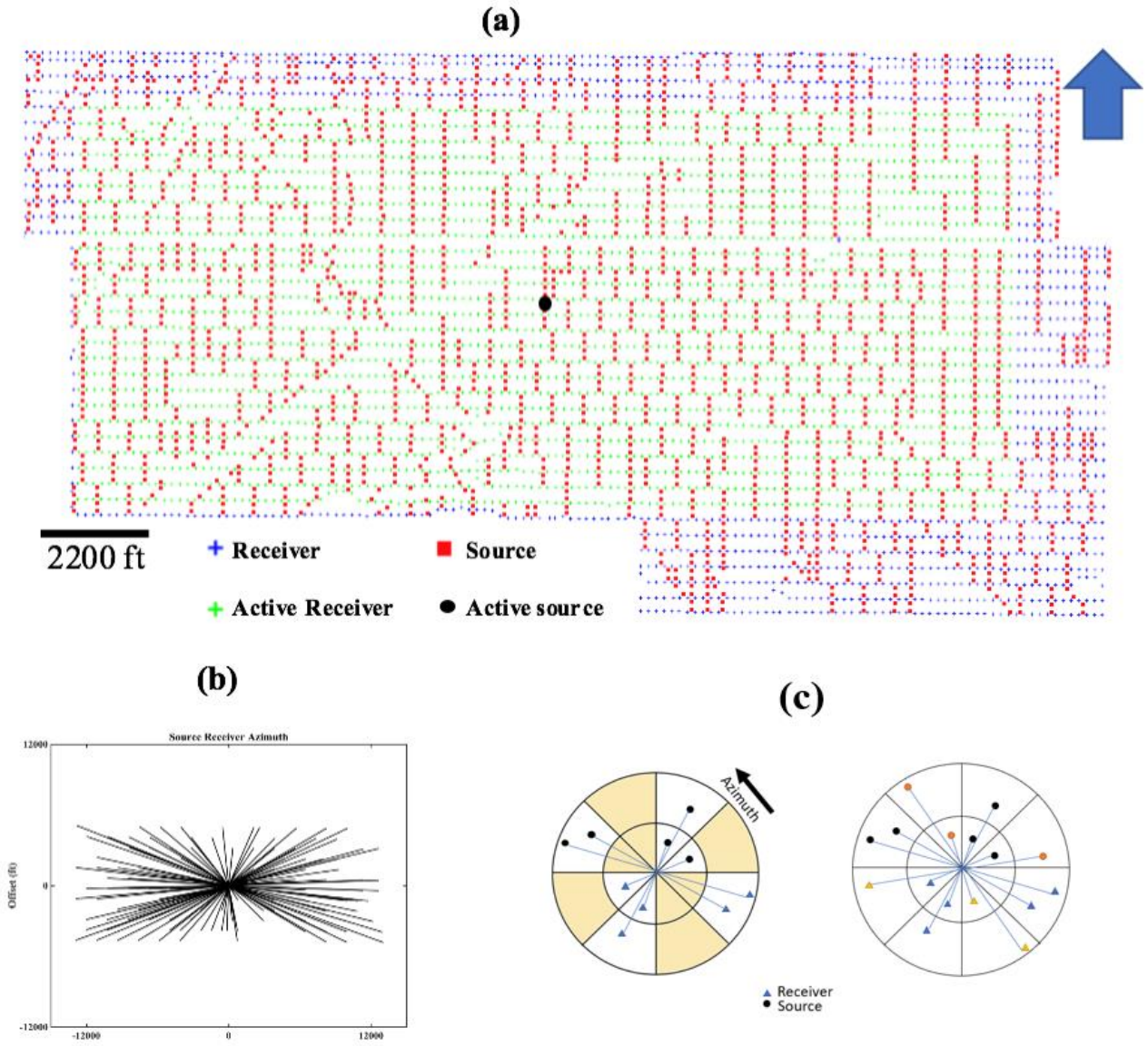

Figure 3.2. (a) Map showing the survey acquisition geometry. orthogonal geometry. Squares indicate shot locations with shot lines running approximately North-South. Plus, signs "+" indicate receivers with receiver's lines running approximately East-West. Back circle and green + signs indicate a representative common-shot gather. (b) Spider diagram a representative common midpoint gather. Notice the survey has longer offsets in the E-W direction than in the N-S direction. (c) cartoon showing the annulus sector binning of a common midpoint gather with two offset and four azimuthal sectors with (left) data before 5D interpolation showing three bins containing one traces, one bin containing two trace, and four bins containing no trace. (right) the goal of 5D interpolation is to fill each bin with at least one trace. In our implementation, the annulus sectors bins measuring $\Delta\varphi$=45° and Δh= 660 ft used to interpolate the data. At least 50% of the traces need to be alive to interpolate.

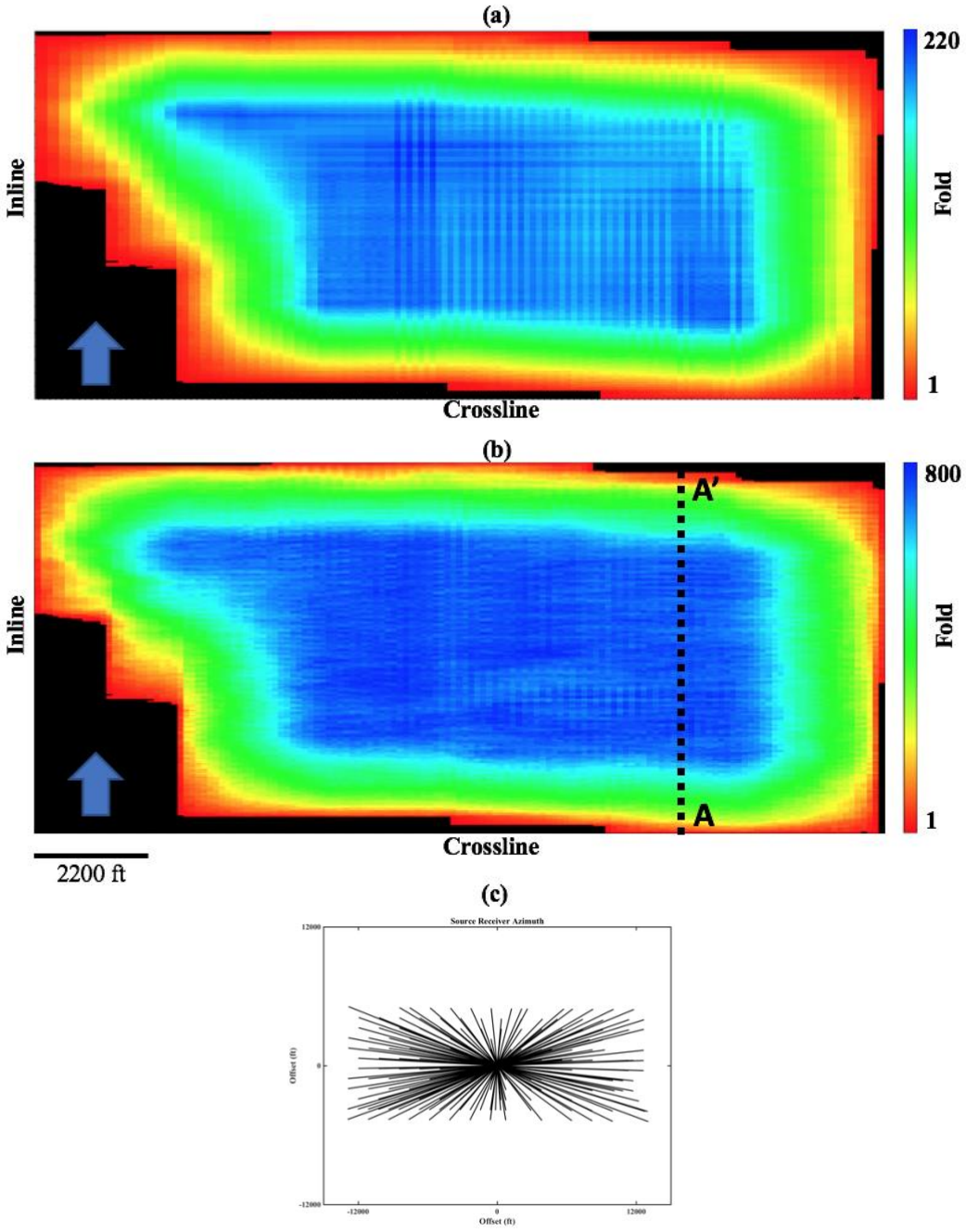

Figure 3.3. Fold map of the survey shown in Figure 3.2 (a) before and (b) after 5D POCS interpolation. The nominal bin size is 110 x 110 ft. In general, this more regular fold will result in reduced acquisition footprint. (c) Spider plot of the same representative common midpoint gather shown in Figure 3.2b after 5D interpolation.

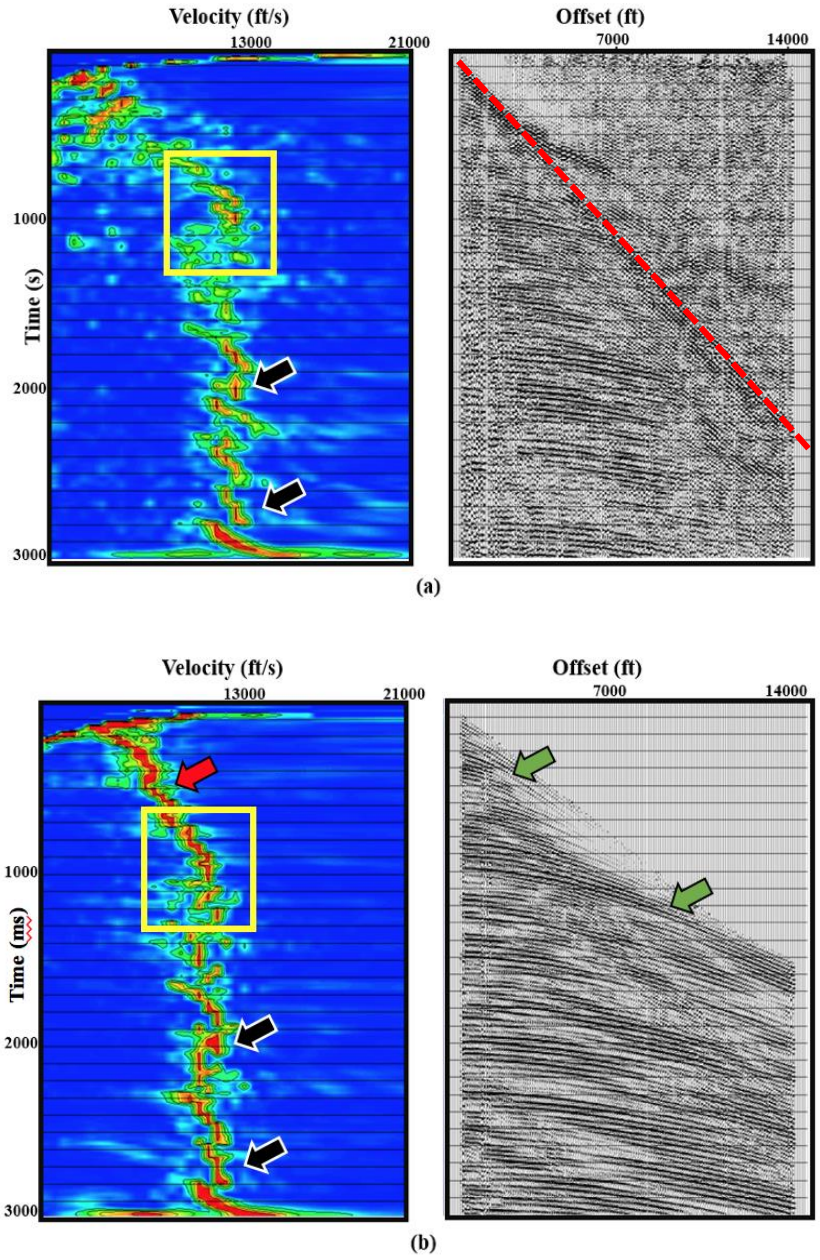

Figure 3.4. Velocity semblance panels and the corresponding CMP supergathers (a) before and (b) after 5D interpolation. The yellow box indicates the target area consisting of high-velocity "Mississippi Lime" and other fast Paleozoic sediments. Top of basement is at approximately t=1.2 s. The section below top basement is contaminated by multiples (black arrow). The interpolated semblance (b) shows more focused "wrap-ups" in the semblance panel (red arrow) and more continuous hyperbolae in the CMP gather (green arrows). Unfortunately, if we picked multiples below the top basement, this continuity of these events will also be "improved". The data beyond the mute zone (red dashed line on the gather in a) have extrapolated and may result in inaccurate response and a stacked volume that over stresses the initial picked velocity.

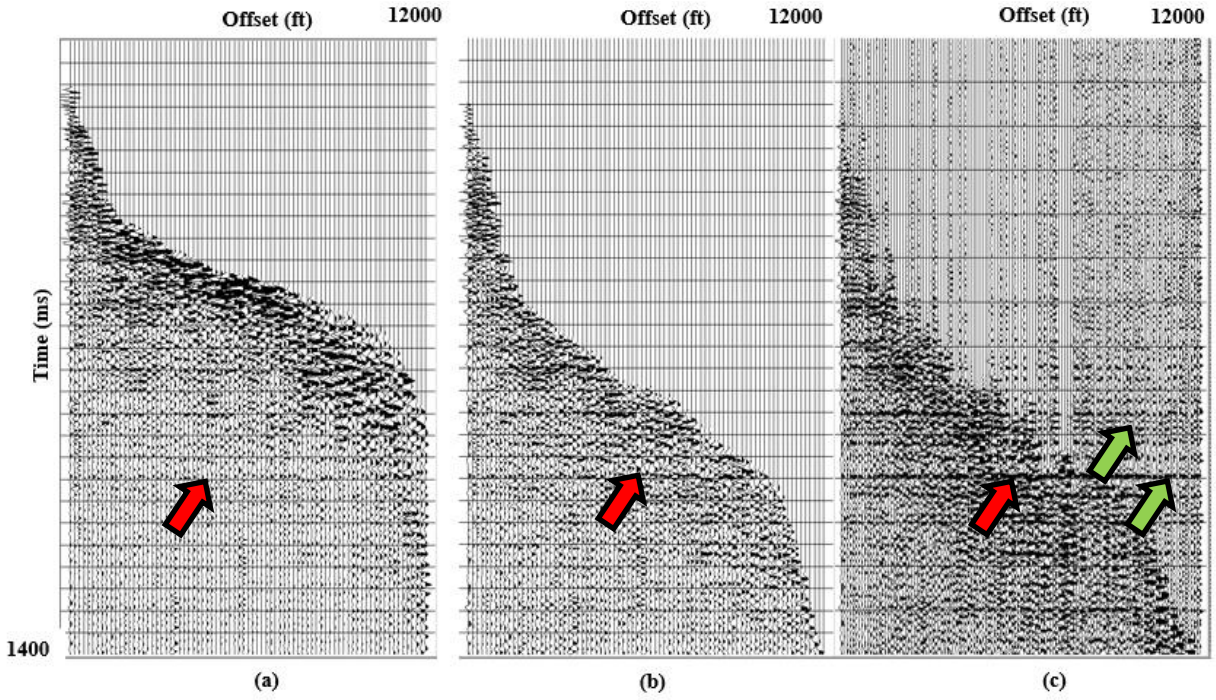

Figure 3.5. (a) Original CMP without mute. (b) Original CMP after the mute. (c) Interpolated CMP. The three CMPS are plotted against absolute offset. Note we have stronger reflections after interpolation and more traces per CMP bin (red arrow). The green arrows show the extrapolated data along the reflections. This data results in stressing the far offset amplitude on the stack.

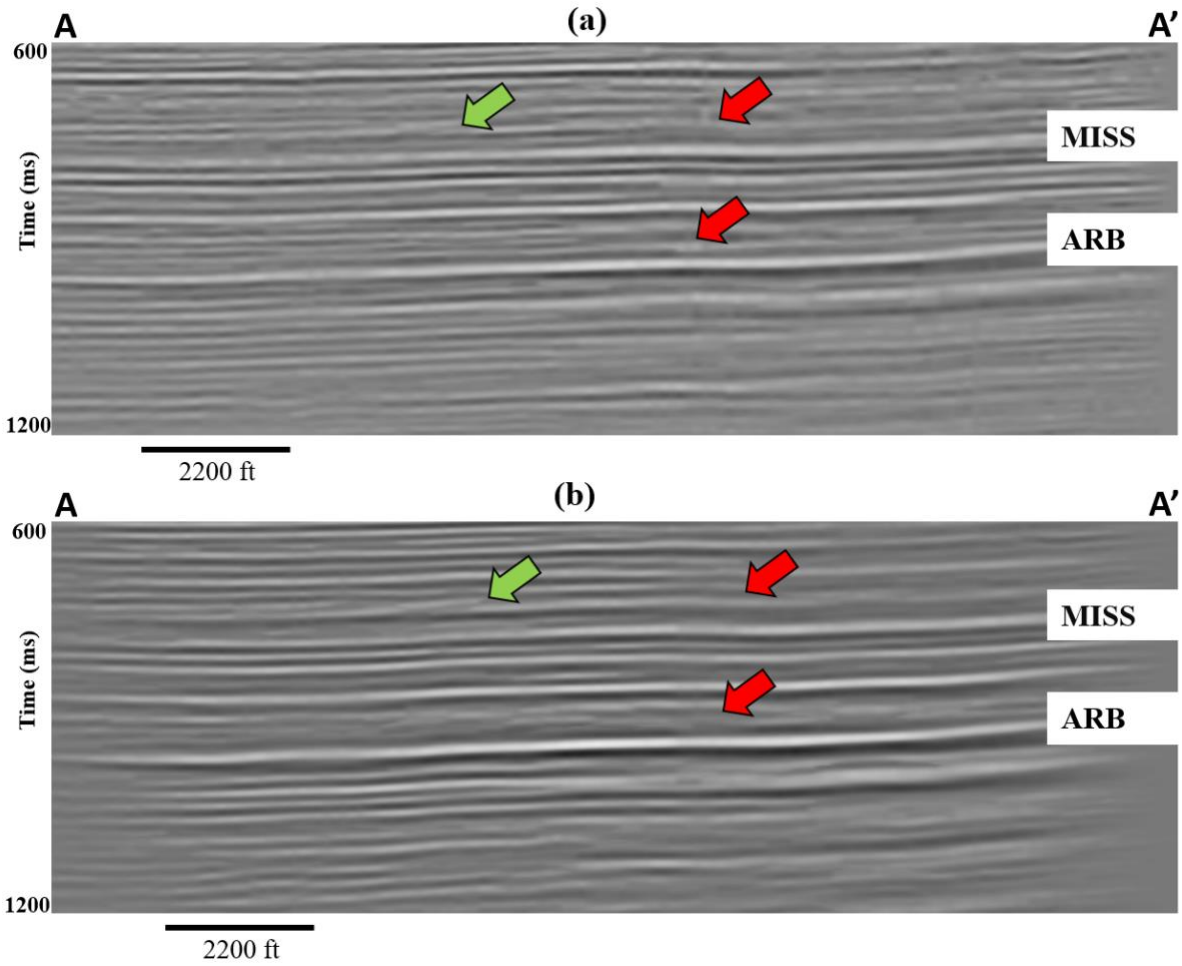

Figure 3.6. Vertical slices along line AA' through the migrated volumes generated (a) without and (b) with 5D interpolation. Note the better amplitude balancing in the zone of interest between t=900 and t=1200 ms. The vertical resolution at the deeper Arbuckle horizon is also significantly improved in (b) when compared with (a). The improved amplitude balancing is directly related to the more consistent fold and spider diagrams provided by 5D interpolation as shown in Figure 3.3. Red arrow indicates areas where the noise has been suppressed. The green arrow shows the fault.

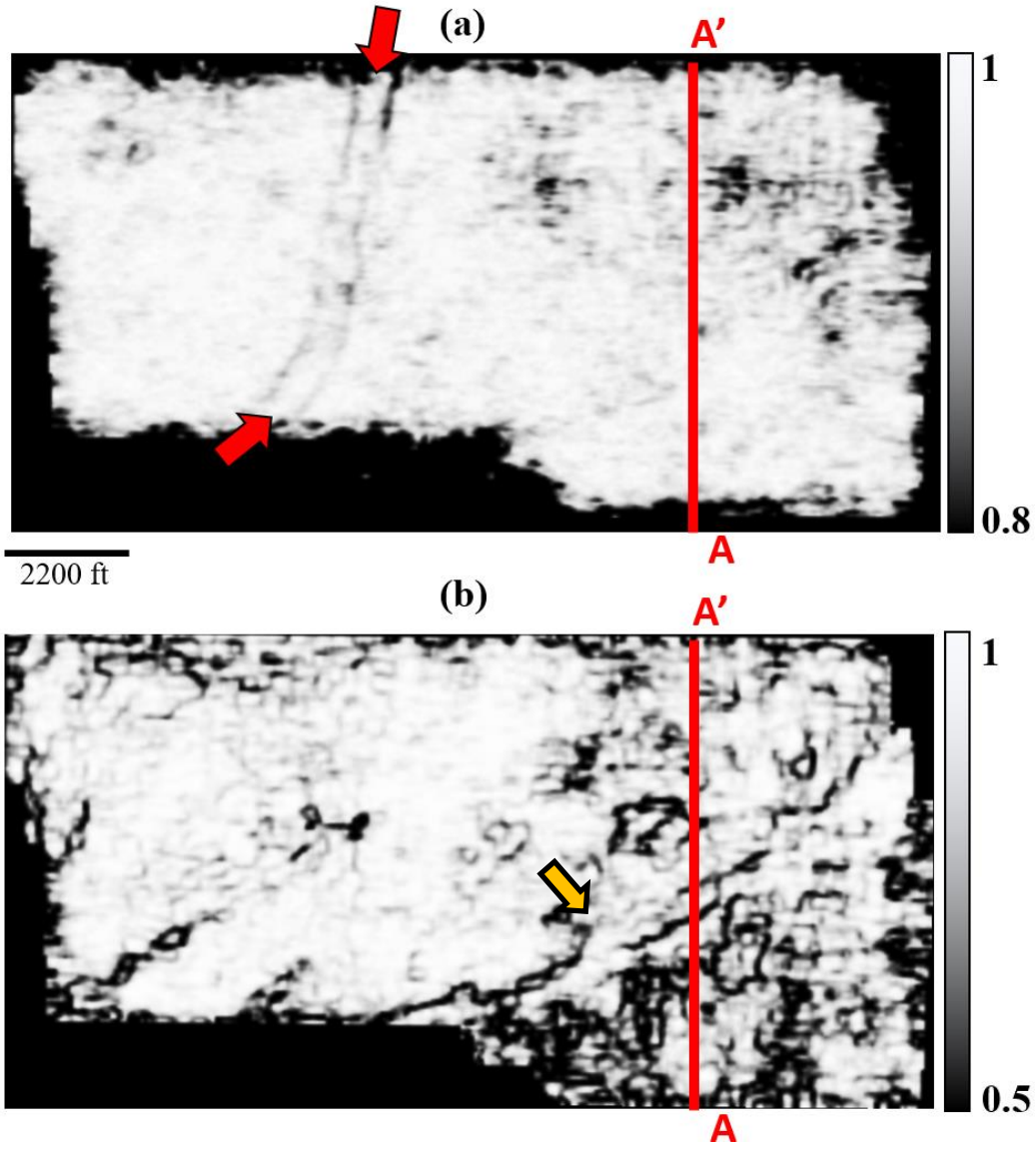

Figure 3.7. A horizon slice along (a) the top of the Marmaton and (b) top Mississippian through coherence volumes computed from on the original data. Note the channel running north-south on the Marmaton slice, indicated by red arrows. In the Mississippian image note what appear to be en echelon faults (orange arrow) and elliptical karst collapse features, some of which were identified by Cook (2016) on horizontal image logs. In both slices, the N-S and E-W acquisition design results in a rectangular footprint pattern that fades in and out across the survey that is directly linked to the deployment of sources and receivers shown in Figure 3.2.

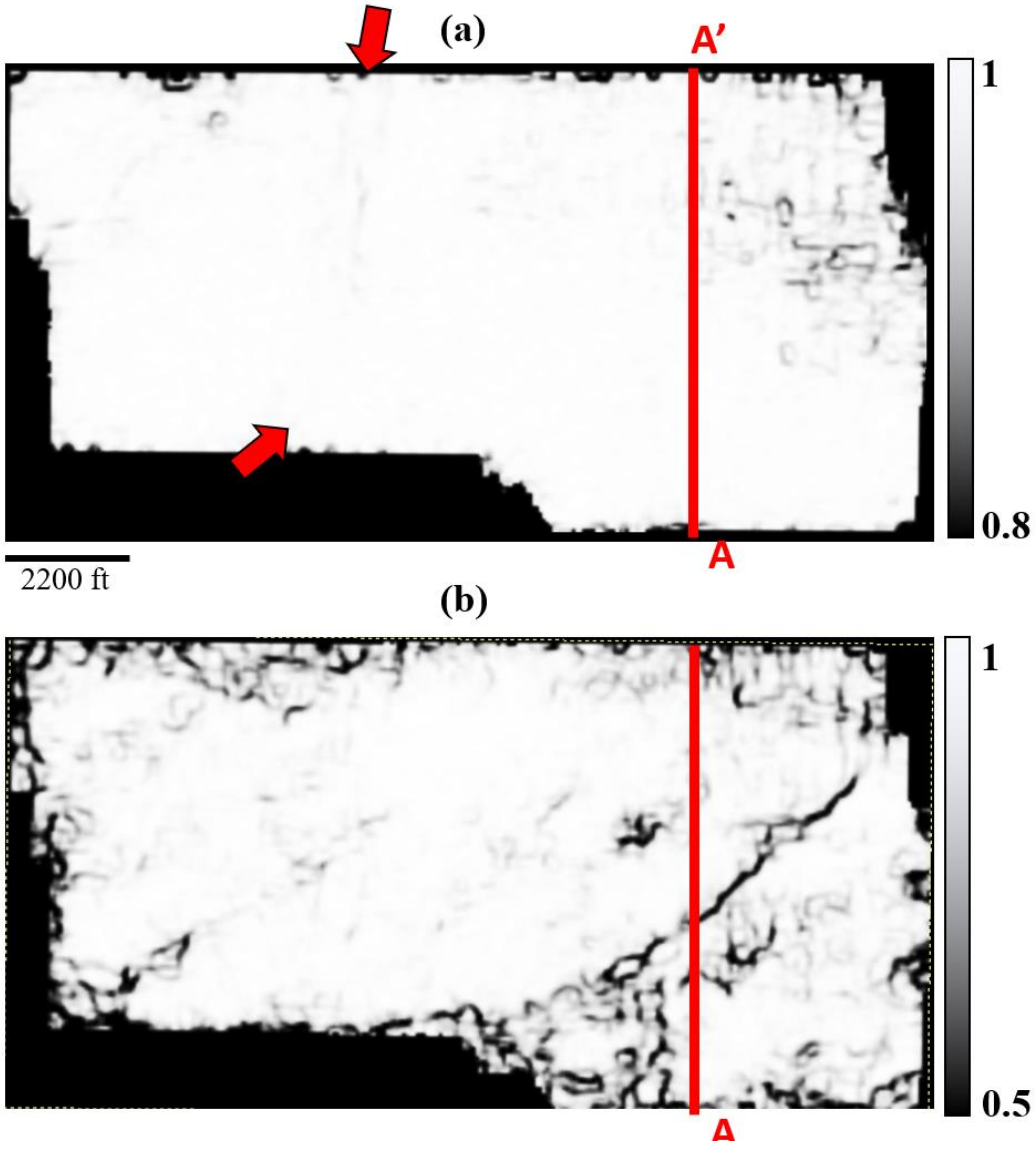

Figure 3.8. The same horizon slices shown in Figure 3.7 along the top of the Marmaton (a) and Mississippian (b) formations but now through the coherence volume computed from the 5D-interpoled volume. Most of the footprint artifacts have been eliminated. Unfortunately, the channel edges seen in Figure 3.7a have been lost after 5D interpolation. The NE-SW trending fault that appeared to be en echelon in Figure 3.7b appears to be more continuous after 5D interpolation rather than as an en echelon fault in Figure 3.7b. Karst collapse features in the Mississippian identified by Cook (2016) also appear to have been suppressed.

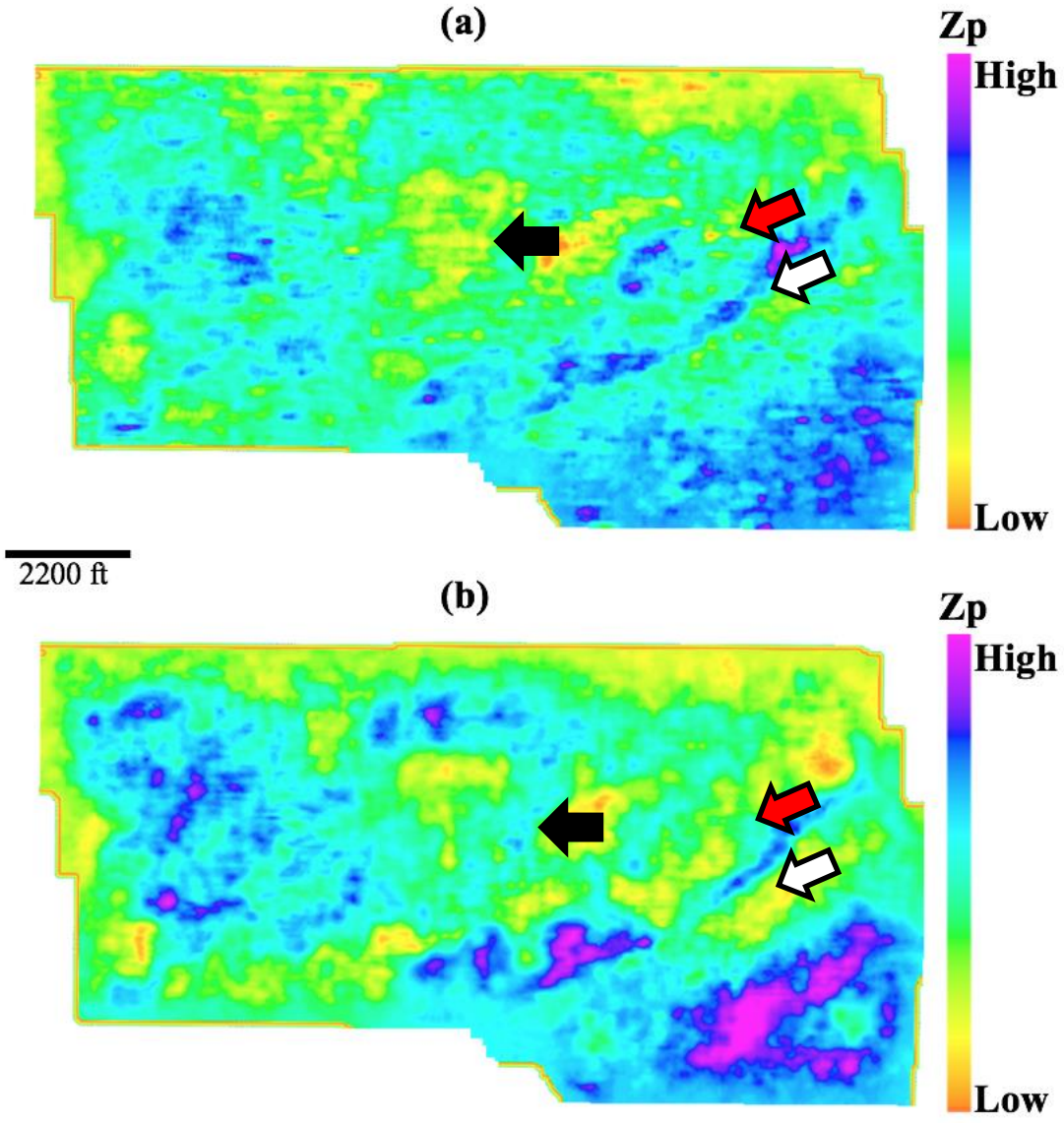

Figure 3.9. Horizon slices along the top of the (a) Marmaton formation and Mississippian through the P-wave impedance volumes obtained by prestack inversion of the original data. The black arrow indicates the liniment feature we describe as footprint.

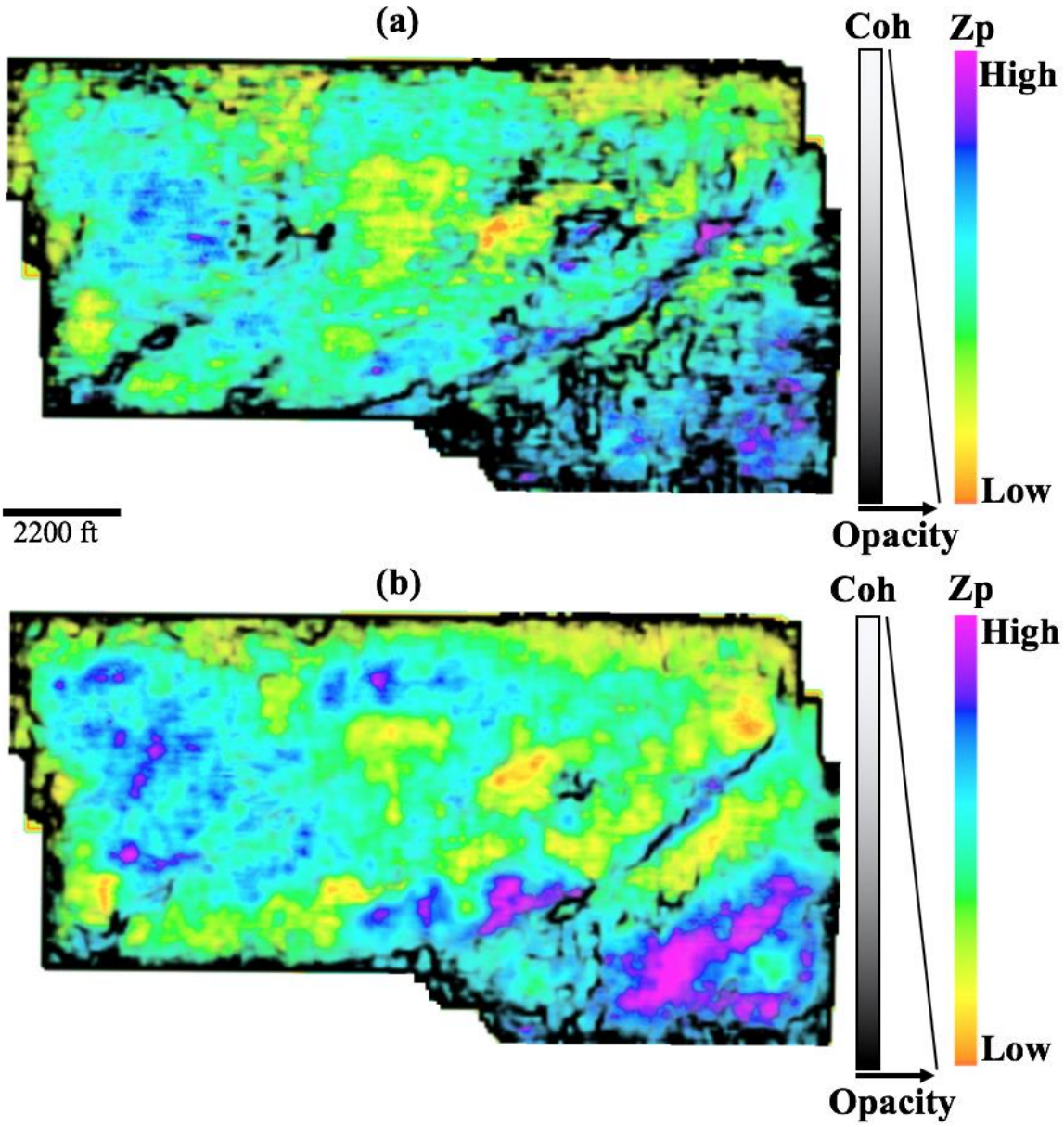

Figure 3.10. Mississippian horizon slices through acoustic impedance co-rendered with coherence (a) before and (b) 5D interpolation.

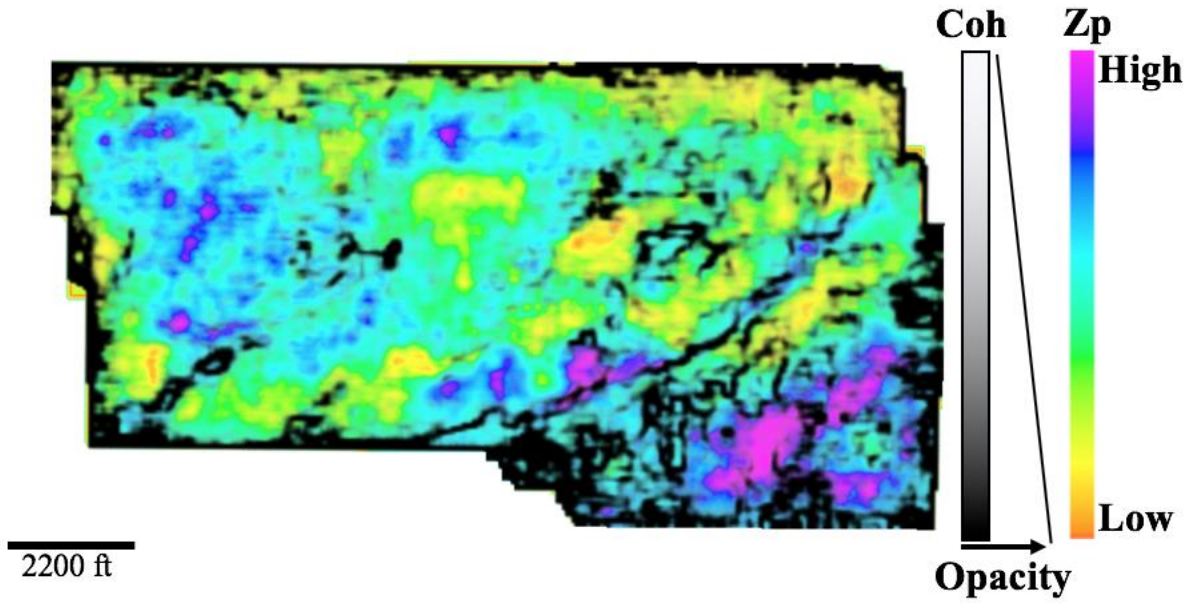

Figure 3.11. The impedance computed on 5D interpolated data co-rendered with the coherence computed on the original data. Note the coherence anomaly seems to delineate the high impedance (magenta) anomaly in the SE part of the image.

References

Abma, R., and N. Kabir, 2006, 3D interpolation of irregular data with a POCS algorithm: Geophysics, **71**, E91-E97.

Alali, A., G. Machado, and K. J. Marfurt, 2018, Attribute-assisted footprint suppression using a 2D continuous wavelet transform: Interpretation, **6**, T457-T470.

Barnes, S., R. V. Borselen, H. Salazar, A. Vazquez, I. Ronzon, and R. Martinez, 2011, Application of True-azimuth 3D SRME to an onshore Mexican data set: 81st Annual International Meeting, SEG, Expanded Abstract, 3515-3519.

Cary, P., and M. Perz, 2012, 5D leakages: measuring what 5D interpolation misses: 82nd Annual International Meeting, SEG, Expanded Abstract, 1-5.

Chopra, S., and K. J. Marfurt, 2013, Preconditioning seismic data with 5D interpolation for computing geometric attributes: 83rd Annual International Meeting, SEG, Expanded Abstract, 1456-1460.

Decker, L. A., 2014, Seismic diffraction imaging methods and applications: M.S. thesis, The University of Texas at Austin.

Downton, J., B. Durrani, L. Hunt, S. Hadley, and M. Hadley, 2008, 5D interpolation, PSTM and AVO inversion: 78th Annual International Meeting, SEG, Expanded Abstract, 237-241.

Galibert, P. Y., L. Duval, and R. Dupont, 2002, Practical aspects of 3D coherent noise filtering using (f-kx-ky) or wavelet transform filters: 72nd Annual International Meeting, SEG, Expanded Abstract, 1-4.

Jin, S., 2010, 5D seismic data regularization by a damped least-norm Fourier inversion: Geophysics, **75**, WB103-WB111.

Lindzey, K., 2015, Geologically constrained seismic characterization and 3D reservoir modeling of a Mississippian reservoir, Northcentral Anadarko Shelf, Oklahoma: M.S. thesis, The University of Oklahoma.

Liu, B., and M. D. Sacchi, 2004, Minimum weighted norm interpolation of seismic records: Geophysics, **69**, 1560-1568.

Montgomery, S. L., J. C. Mullarkey, M. W. Longman, W. M. Colleary, and J. P. Rogers, 1998, Mississippian "chat" reservoirs, South Kansas: Low-resistivity pay in a complex chert reservoir: AAPG Bulletin, **82**, 187-205.

Pan, J., and G. Schlosser, 2013, 5D Interpolation of seismic data with combination of MWNI and POCS algorithm: Integration geoConvention, 1-3.

Pan, X., S. Cao, S. Zu, and F. Gong, 2016, A fast minimum weighted norm interpolation: 86th Annual International Meeting, SEG, Expanded Abstract, 4107-4111.

Peery, A., 2017, Application of modern 3D seismic data acquired for deeper resource plays to shallower mature fields- A Red Fork case study: M.S. thesis, The University of Oklahoma.

Rauch-Davies, M., K. Deev, D. Pelman, and M. Kachkachev-Shuifer, 2014, Diffraction imaging applied to pre-existing 3D seismic data to map fracture corridors in an unconventional play: First Break, **32**, 87-90.

Sunson, N. H., 1998, The Geology of the Gypsum Hills in Woodward and Major Counties in Oklahoma: Technical report, Oklahoma Geological Survey.

Trad, D., 2009, Five-dimensional interpolation: Recovering from acquisition constraints: Geophysics, **74**, V123-V132

_____, 2014, Five-dimensional interpolation: New directions and challenges: CSEG Recorder, 2-29.

Verma, S., S. Guo, and K. J. Marfurt, 2016, Data conditioning of legacy seismic using migration-driven 5D interpolation: Interpretation, **4**, SG31-SG40.

Wang, J., and S. Wang, 2013, Hybrid 5D Fourier transform - A flexible tool for land data interpolation: 83rd Annual International Meeting, SEG, Expanded Abstract, 3603-3607.

Xu, S., Y. Zhang, D. Pham and G. Lambare, 2005, Antileakage Fourier transform for seismic data regularization in higher dimensions: Geophysics, 75, WB113-WB120.

Zhang, B., T. Lin, S. Guo, O. E. Davogustto, and K. J. Marfurt, 2016a, Noise suppression of time-migrated gathers using prestack structure-oriented filtering: Interpretation, 4, SG19-SG29.

Zhang, C., Y. Li, H. Lin, and B. Yang, 2016b, Seismic directional random noise suppression by radial-trace time-frequency peak filtering using the Hurst exponent statistic: Geophysical Prospecting, **64**, 571-580.

Chapter 4: Signature of Fractures on Seismic Data

Abdulmohsen Alali, Nori Nakata, Bin Lyu and Kurt Marfurt

The University of Oklahoma, ConocoPhillips School of Geology and Geophysics.

This paper will be submitted to the SEG journal Interpretation

Abstract

Fractures play an important role in most carbonate and unconventional reservoirs. For this reason, accurate identification of fractures and their associated properties using seismic data have significant importance in reservoir characterization. Amplitude variation with azimuth analysis provides measurements that are sensitive to the intensity (fracture density) and orientation of fractures. If the fractured unit can be treated as an equivalent anisotropic effective medium, we can create an approximate fracture model. The underlying assumption of effective medium theory is that the fractures are uniformly disturbed and sufficiently close such that only specular reflections from the boundaries of the fractures are observed. In contrast, for random fracture spacing, individual scattering occurs, and the assumptions of effective medium theory assumption are violated.

In this paper, we model discrete fractures in the reservoir and analyze the amplitude at the top and bottom of the reservoir. In the first analysis, we examine constant vs random fracture distributions. We find that the bottom reflection is more sensitive to the fracture scattering and hence shows a larger amplitude deviation between the constant and random fracture spacing amplitudes. In the second analysis, we vary the fracture vertical location within the reservoir. The deviation in the bottom reflection is reduced with reduced fracture vertical extent. Finally, comparing the amplitude of the top reflection generated of isotropic and the fractured models indicates the location of fractures within the reservoir.

Introduction

Natural fractures exist in both conventional and unconventional reservoirs. Natural fractures exist in various scales, from discrete joints/faults measuring 10s or 100s of meters to

microcracks measured in millimeters. Fractures are important in oil and gas exploration and development, providing not only significant permeability, but sometimes significant porosity as well. The knowledge of the spatial distribution, orientation and mechanical properties of the fracture systems is critical in constructing numerical reservoir simulators to enhance oil recovery.

Fracture detection is an integrated task involving geology, geophysics and petrophysical techniques. A common approach is to use hard-data, such as cores, outcrop analysis, image log, and well logs measured directly from the target formation. In general, such measurements provide very high vertical resolution and can be used to constrain predictions made from 3D surface seismic data. Hard-data are essential in characterizing the zones of interest and providing information on whether the fractures are limited to a specific formation or cut through multiple formations. Core and log measurements are local and hence fail to provide information on the natural network and lateral extent of the fractures (Milad et al., 2018).

Another common technique relies on 3D surface seismic data which provide higher lateral resolution but lower vertical resolution than well control. Depending on the scale of the fractures, different seismic attributes can be used. Large-scale faults can be detected using seismic geometric attributes, such as coherence, curvature or disorder (Marfurt and Chopra, 2007). "Fracture swarms" which are closely spaced fractures can be detected using diffraction imaging (Decker, 2014). Cracks and micro-scale fractures can be indirectly detected through azimuthal variation in velocity and amplitude (Grechka, 2014; Liu et al., 2016; Liu and Martinez, 2012).

Figure 4.1 shows the different scale fractures and their methods of detection. Beginning with fractures that are much smaller than the seismic wavelength, such microscale fractures, give rise to amplitude and velocity variations that can be measured on prestack seismic offset and azimuth gathers. This directional dependence of velocity and amplitude, or anisotropy, requires a

theoretical model that allows us to build relation between the sub-seismic scale properties and the seismic wavelength. We use Effective Medium Theory (EMT), to replace the small scale heterogenous isotropic medium with an equivalent large scale homogeneous anisotropic media to represent the fractures. When the size of fractures relevant to the seismic wavelength is extremely small, the effect of a fractured layer on the seismic response can be treated as the average properties of a medium (Schoenberg and Sayers, 1995).

Techniques characterizing the anisotropy can be based on velocity or amplitude variations with direction. The most common velocity-based techniques to characterize the anisotropy include velocity variation with azimuth (VVAz) and shear-wave splitting, as well as amplitude-based techniques such as amplitude variation with Azimuth (AVAz). The anisotropy parameters predicted by each technique vary due to method sensitivity and underlying approximations (Delbecq et al., 2013).

Since initial observations of azimuthal changes in velocity by Lynn et al. (1995), Mueller (1991), Crampin (1981), and Thomsen (1986), anisotropy analysis from surface seismic data has progressed rapidly. Rüger and Tsvankin (1997) defined the basic theory for amplitude-variation-with-offset (AVO) inversion in fractured media. Gray (2008) used azimuth-dependent variations in the AVO to allow fracture delineation. Zelewski et al. (2009) demonstrated the usefulness of wide-azimuth and AVAz in predicting the presence of fractures. Dong and Davidson (2003) discussed seismic acquisition design and its impact on the prediction of fracture density and orientation. Liu et al. (2011) proposed a pre-processing workflow dedicated to amplitude versus incident and azimuthal angle (AVAz) inversion, while simultaneously addressing the imaging issues caused by the shallow surface overburden complexity and acquisition footprint. Liu et al.

(2016) studied the effects of overburden and thin layers on fractures-induced azimuthal AVO response through forward modeling.

Other scholars conducted more complicated forward modeling experiments to validate the robustness of the effective medium theory. Liu et al. (2015) constructed a synthetic model with parallel and orthogonal fractures at different scales and estimated the fracture density of the small-scale fractures even when large-scale fractures were present. Fang et al. (2017) showed that fracture clustering, which violates the uniform fractures distribution assumed by EMT, can significantly affect the reflection characteristics and cause AVAz/AVO responses to deviate from those corresponding to constant spaced fracture amplitude. Seismic amplitude in the presence of fracture clustering is dominated by fracture scattering; with sufficient clustering one may treat fracture scattering as a single separate diffraction. Schuster et al. (2017) argue that with sufficient lateral seismic data resolution that one can separate diffractions using diffraction imaging.

Diffraction imaging is unique due to its ability to image small-scale discontinuities including faults, edges, pinch outs, rugosity, channel edges, fractures, and karst (Sturzu et al., 2014; Sturzu et al., 2015; Decker, 2014; Osareni et al., 2017). Liu et al. (2015) used four color-blended diffraction volumes to highlight lineament in the sub surface. Rauch-Davies et al. (2014) and Berkovitch et al. (2009) used diffraction imaging to generate a diffraction strength volume and correlated it with fracture density from well logs to highlight potential fracture corridors. In addition to scattering due to fractures, the effect of the overburden, thickness and lateral distribution of the fractures is an active area for research. Documenting the effect of fracture signature on seismic amplitude can help bridge the gap between the high resolution seen on image logs such as Schlumberger's Fullbore Formation Microimager (FMI logs) and the seismic data.

In this study, we consider two groups of fractures, confined fractures which are extensional non-sheared fractures that do not cross through the entire layer and unconfined fractures which are fractures that cut through the whole layer. We follow the work by Fang et al. (2017) and examine the seismic amplitude due to a fractured medium using both constant and irregular fracture spacing. in both confined and unconfined settings.

The paper is structured as follows: First, we briefly introduce the models of fractured media and the parameters needed to build the model of choice. We use the power-law theory that provides the randomness of the fracture spacing. Second, we introduce the modeling algorithm and the properties of the fractures considered in this study. Third, we validate our modeling accuracy by constructing a three-layer model with a constant fracture spacing and propagating the wavefield as an EMT (single anisotropy parameters) vs. discrete joints fractures, where each fracture is modeled using a single stiffness. Next, we generate a suite of three-layer models and vary the confined and unconfined fracture spacing and location within the reservoir and analyze the amplitude on CMP gathers. We conclude with a summary of the advantages and limitations of studying fractures using full wavefield modeling.

Models of Fracture Media

Fracture intensity and orientation are two of the more important parameters we need to estimate both in the exploration stage of the oil field and later in the development and mature stage when constructing geocellular models for flow simulation (Milad and Slatt, 2018). Working backwards from 3D surface seismic data, we first characterize the seismic anisotropy and subsequently the physical properties of the fractures. The most popular method to characterize anisotropy is the estimation of Thomson's parameters (Rüger et al., 1997; Thomsen, 1986). While

Thomson's parameters are very useful in characterizing anisotropy, they offer no direct reference to the fracture properties of the medium. A second widely used fracture model is based on either Schoenberg's (1980) Linear Slip Theory (LST) on Hudson's (1980) model.

Linear Slip Theory describes a fracture as a thin layer inside an isotropic host medium. As the thickness of the inserted layer approaches zero, the resulting medium reduces to a linear slip interface. The LST technique allows us to study the fracture represented as a weakness surface. A horizontally fractured medium is formed by an interface inserted in a homogeneous isotropic host medium. A vertically fractured medium is formed by a vertical interface inserted in a homogeneous isotropic host medium.

Hudson's (1980) model represents fractures as aligned isolated penny shaped cracks inside the host rock. The origin of the isolated penny shaped cracks indicates the type of anisotropy, typically with a Horizontal axis of symmetry (Horizontally transverse isotropic, HTI) or Vertical axis of Symmetry (vertically transverse isotropic, VTI). Hudson's model treats fractures as isolated cracks and therefore does account for the fluid flow between cracks. The accuracy of Hudson's theory decreases when the crack density is large. In contrast, LST holds for large crack densities (Grechka and Kachanov, 2006). Also, LST offers a more intuitive understanding of the fracture because it does not assume penny shaped cracks. For this reason, we will use the LST to model fractures in this paper. The elastic properties of a fracture are described by the fracture compliance matrix and depend on the geometry of the fracture surface (Schoenberg, 1980; Schoenberg and Sayers, 1995). The stiffness matrix for an HTI medium is given by:

$$C = \begin{bmatrix} (\lambda+2\mu)(1-\Delta_N) & \lambda(1-\Delta_N) & \lambda(1-\Delta_N) & 0 & 0 & 0 \\ \lambda(1-\Delta_N) & (\lambda+2\mu)[1-\frac{\lambda^2}{(\lambda+2\mu)^2}\Delta_N] & \lambda(1-\frac{\lambda}{\lambda+2\mu}\Delta_N) & 0 & 0 & 0 \\ \lambda(1-\Delta_N) & \lambda(1-\frac{\lambda}{\lambda+2\mu}\Delta_N) & (\lambda+2\mu)[1-\frac{\lambda^2}{(\lambda+2\mu)^2}\Delta_N] & 0 & 0 & 0 \\ 0 & 0 & 0 & \mu & 0 & 0 \\ 0 & 0 & 0 & 0 & \mu(1-\Delta_T) & 0 \\ 0 & 0 & 0 & 0 & 0 & \mu(1-\Delta_T) \end{bmatrix} \quad (1)$$

where

$$\Delta_N = \frac{d_f Z_N(\lambda+2\mu)}{1+d_f Z_N(\lambda+2\mu)}, \quad (2)$$

and

$$\Delta_T = \frac{d_f Z_T \mu}{1+d_f Z_T \mu}, \quad (3)$$

where

λ and μ are the lame parameters,

Δ_T and Δ_N are the tangential and the normal weakness,

Z_N and Z_T are the normal and tangential compliances, and

d_f is the fracture spatial density that is defined as the number of fractures per unit distance.

Note that C_{44} is equal to the μ of the homogeneous isotropic host medium stiffness which indicates that the fracture is described by the elements corresponding to the fracture system only (Cui et al., 2018; Bakulin et al., 2002). Under the LST, the anisotropy parameters can be linked directly to the fractures using equations 1-3. The HTI medium is the simplest to study the fracture behavior and seismic data signature as a function of offset and azimuth.

To construct the randomness of the fracture spacing, we follow the power-law function by Priest and Hudson (1976) and Fang et al. (2017) given by:

$$m = \frac{a^n - a_{min}^n}{a_{max}^n - a_{min}^n}, \quad (4)$$

where a is the fracture spacing in unit distance, n is the power-law exponent that controls the distribution, m is a random number between 0 and 1, and a_{min} and a_{max} are the minimum and maximum values for fracture spacing, respectively. By solving equation 4 for a we obtain models with different fracture spacing. Using $n = 1$ generates uniform random distribution between a_{min} and a_{max} which can lead to the formation of clusters of fractures.

Finite Difference Modeling

We use the finite-difference software of Tesseral Technology Inc (Kostyukevych et al., 2008) to model the anisotropic wavefield. A grid size of 4 meters in Δx and Δz is used for optimized forward modeling. The source is a Ricker wavelet with 30 Hz peak frequency. Each fracture is modeled as a single grid width size. We define the normal stiffness (Z_N = 5 e-9 m/Pa) and (Z_t = 5 e-8 m/Pa) as a function of the normal (Δ_N) and tangential weakness (Δ_T). We generate fractured models using both effective medium theory (EMT) and as discrete joints akin to the work done by Fang et al. (2017). For the EMT, we model the fractured layer using the average anisotropic parameters over the wavelength. In all our models, the fractures are situated in a layer with v_P=3 km/s, v_S=1.7 km/s and density 2200 $\frac{kg}{m^3}$. The fracture planes are assumed to be vertical (HTI) for all cases such that the only variable is the fracture spacing. Given the frequency and the velocity of the fractured layer, we determine the dominant wavelength to be 100 meters.

Numerical Validation

Our objective is to examine the amplitude due to non-uniform fracture spacing in different confined setting. First, we analyze the scattering due to a single fracture in a homogenous medium. Figure 4.2 shows a simple sketch to describe the different arrivals due to a single fracture. The observed arrivals are: PP and PS diffractions from the top and bottom tips of the fracture, as well as scattering from the sides of the fracture in the form of P-P scattering and P-S scattering. Fang et al. (2013) carried a detailed analysis and concluded that the factors that influence fracture scattering are the stiffness of the fracture and specifically (Z_N/Z_t), incident angle and Poisson's ratio of the host medium (Fang et al., 2013). In our analysis we use $\frac{Z_N}{Z_t} < 0.5$ and hence P-S scattering dominates the energy scattered due to the fracture (Fang et al., 2013).

Second, we validate the accuracy of the modeling algorithm using uniformly distributed fractures modeled via the EMT and as discrete joints fractures. We construct a model with 129 fractures and 12-meter spacing using a single source located in the middle of the survey. Figure 4.3 shows the models used to generate the two datasets. Figure 4.4 shows the shot gather generated using the EMT (Figure 4.4a) and the discrete joints (Figure 4.4b). The two shot gathers are identical which indicate the validity of our modeling algorithm under the EMT assumption of uniformly spaced fractures. Next, we use equation 5 to generate a random fracture distribution with a_{min} =8, a_{max} =24 and n=1. The spacing between adjacent fractures is plotted against the offset in Figure 4.5. As a comparison, we show the shot gather generated using the constant spacing fractures vs. the randomly spaced fractures in Figure 4.6a and 4.6b. Using the random distribution, we observe scattering particularly below the second reflection. Scattering also occurs under the first reflector but are weaker.

CMP Amplitude Analysis

In the previous section we demonstrated how scattering due to irregular spaced fractures can generate amplitude signatures different from uniformly spaced fractures on common shot gathers. In this section, we analyze the seismic amplitude on CMP stacked data in three different scenarios: isotropic, consent spacing fracture, and irregularly spaced fractures. We also vary the location of the fractured zone. Figure 4.7a shows the models in depth with unconfined fractures that cuts through the whole formation, fractures confined to the top (4.7b) and fractures confined to the bottom (4.7c) of the formation.

The acquisition configuration is shown in Figure 4.7d. The fracture parameters and wavelet used for modeling are the same as those used in Figure 4.3. For the irregular fracture model, we computed 30 simulations for each of the models shown in Figure 4.7 using equation 1 and a_{min} =8, a_{max} =24 and n=1. CMP data are collected from 0.5 to 1 km. We show the normalized P wave amplitude comparison in Figure 4.8. The red and yellow curves indicate the response of the constant and irregularly spaced fracture models. The blue dashed curves indicate the response due to an isotropic case. Figures 4.8a and 4.8b are for the unconfined fracture, Figures 4.8c and 4.8d are for the fracture confined to the top of the formation and finally Figure 4.8e and 4.8f show the bottom confined fracture. For the unconfined fractures, comparing Figure 4.8a with 4.8b shows a smaller deviation between the constant and random fracture spacing for the top reflection and a big deviation for the bottom reflection. The bottom reflection has a larger Fresnel zone and is affected more by the fractures. For the top confined fracture, Figure 4.8c shows identical results to 4.8a because the same fracture scattering is seen by the top reflection in both cases. For the bottom reflection 4.8d, the isotropic reflection has larger normalized amplitude than the fractured reflection. For the bottom confined fracture, the top reflection of the fractured cases matches the isotropic case. In the presence of an accurate velocity model such as from tomography or CMP

reflection scan, modeling the response for an isotropic model and comparing it with the real data gives a quick indication about the location of the fracture. From our analysis we notice the top reflection is less influenced by fracture scattering and can provide insight when compared with the modeled isotropic amplitude behavior. The bottom reflection sees more of the fracture signature but translating the signature into fracture spacing is challenging. Due to the deviation between the constant spacing and irregular fractures, the results indicate that EMT may give inaccurate results because it does not account for fracture clustering effect.

Limitations: Although the thickness of this reservoir is unrealistic, similar results can be achieved using thinner formation and higher frequency wavelets. In addition, stacked carbonate can give rise to strong internal multiples and undesired arrivals and those have not included in this analysis. We also assumed knowledge of the spatial distribution and characteristics of the fracture to construct our forward models. For real data, we can rely on core and outcrops to approximate of the fracture characteristics and orientation to carry similar forward model analysis. Although numerical modeling does not encapsulate the full complexity of the real data problem, it gives more insight into studying fracture scattering as a complimentary method to the existing effective medium theory. Also, forward modeling can bridge the transition from EMT and fracture-scattering theory to diffraction scattering theory base methods such as diffraction imaging. Linking diffraction imaging to fracture characterization is an active area of research. In Appendix A we analyze the effect of anisotropy as a function of azimuth for different fractured layer thicknesses. Also, we list some of the factors controlling the resolution of diffracting imaging through established concepts in the literature.

Conclusions

Using numerical modeling under EMT and as unconfined, confined discrete joints we find that when: fractures are irregularly spaced, clustering occurs, and the response is different from the seismic amplitude predicted from EMT theory. This amplitude deviation is stronger for the bottom reflections.

The top reflection is less influenced by fracture scattering and by comparing it to isotropic modeled AVO can establish whether fractures are confined to the bottom of the reservoir. It remains a future research area to study the effect of scattering in a thinner more realistic formation thickness and predict fracture distribution from fracture scattering directly. Also, studying the signature of random fracture length can spark ideas to using fracture scattering directly to analyze the anisotropic properties.

Acknowledgments

Special thanks to Magdy Ghattas of Marathon Oil Co. for fruitful discussions and bringing our attention to this area of research. We would like to extend our gratitude to the sponsor of the Attribute Assisted Seismic Processing and Interpretation (AASPI) consortium for their generous support. Special thanks to Tesseral Technology for providing the licenses for Tesseral Pro needed to carry this study. The first author thanks Saudi Aramco for support of his Ph.D. studies.

Figures

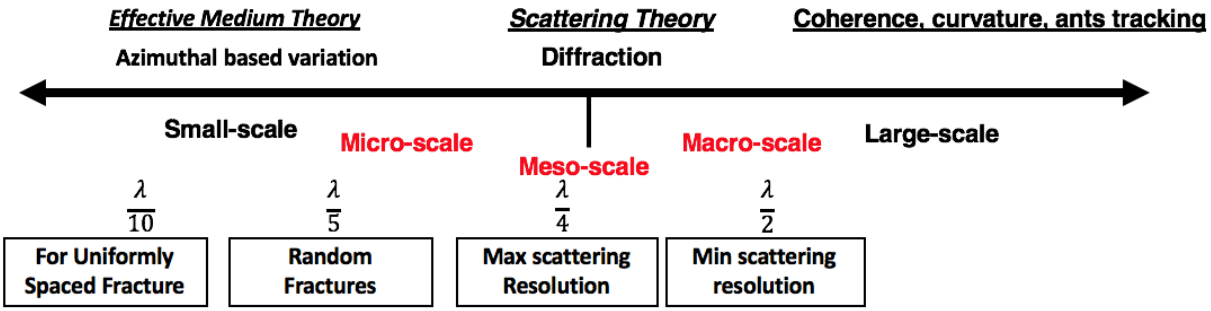

Figure 4.1. Different scale fractures are detected using different methods. Larger scales can be detected through seismic attributes such as coherence. Meso-scales can be detected using diffraction imaging. Micro-scale can be detected through AVAz and AVO. In this paper, we focus on the micro-scale to meso-scale transition.

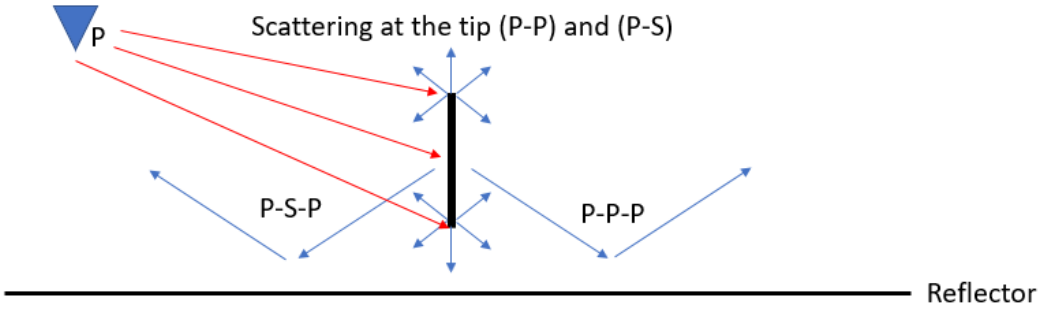

Figure 4.2. Different arrivals due to a single fracture for incident P-waves. Modified after (Fang, et al., 2013). Depending on the fracture properties such as stiffness, elastic properties and angle of incident (red arrows), different arrivals dominate the response. Although shear waves are generated from the refraction tips, we preferentially measure and process to enhance PP diffractions. In contrast, a P-wave incident on the side of the fracture will generate both PP and PS reflections. These events will convert at the bottom of the formation (forming what many call a prism wave) which where PPP and PSP events are measured at the surface.

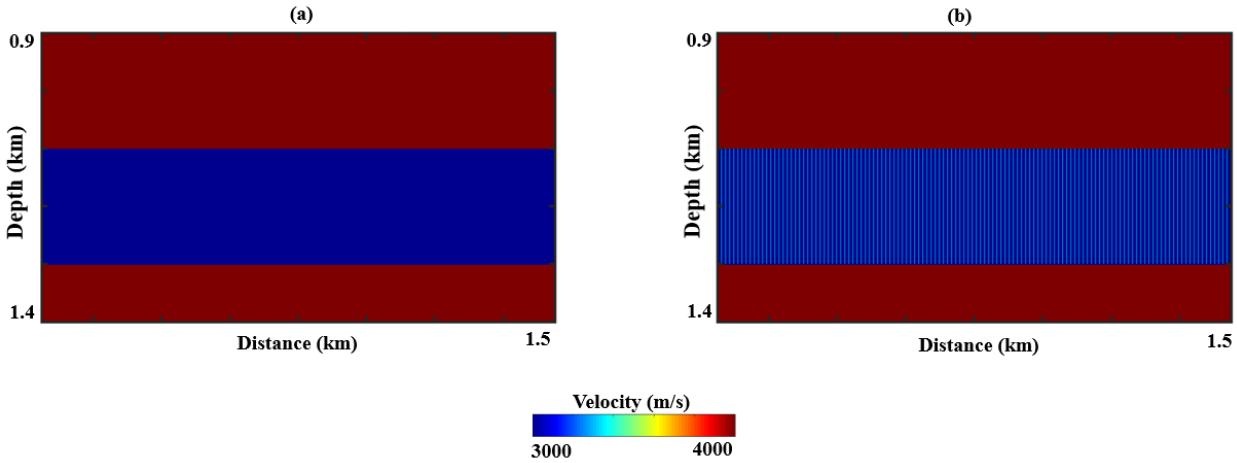

Figure 4.3. The model used to generate the data under the effective medium theory (4.3a) and as discrete joints (4.3b). In 4.3b the spacing between the fracture is 12 m. The thickness of the fractured layer is 200 m and the fractures extend through the whole layer (unconfined fractures). We average the anisotropy parameters over the wavelength to represent the model under the EMT.

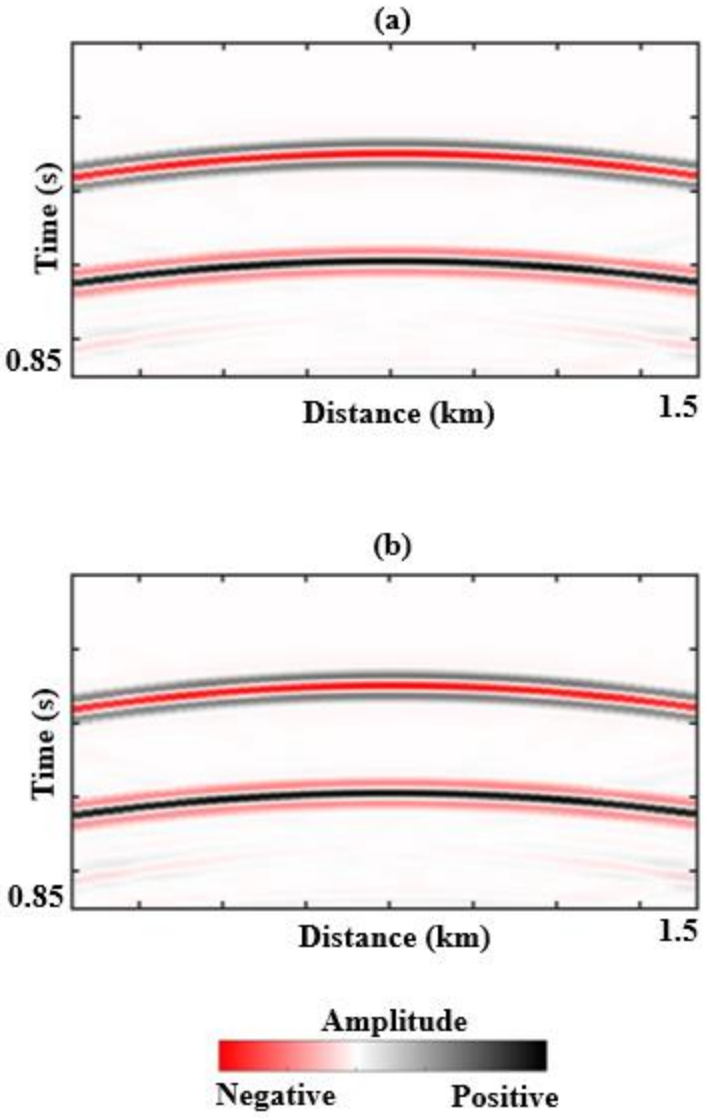

Figure 4.4. (a) Shot gather modeled using the model in Figure 4.3a. (b) Shot gather modeled using the model in Figure 4.3b. A wavelet with a peak frequency of 30 Hz, grid size is $\Delta x=\Delta z=4$ m. The two shot gathers are identical which confirms that discrete joints give similar results to EMT when the fractures are uniformly spaced.

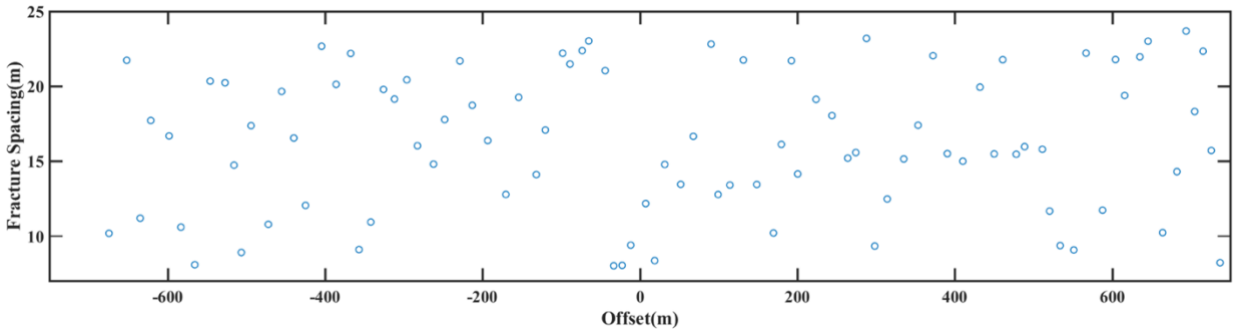

Figure 4.5. Fracture spacing generated using the power-law equation, the circle represents the fracture spacing between adjacent fractures against the source-receiver offset.

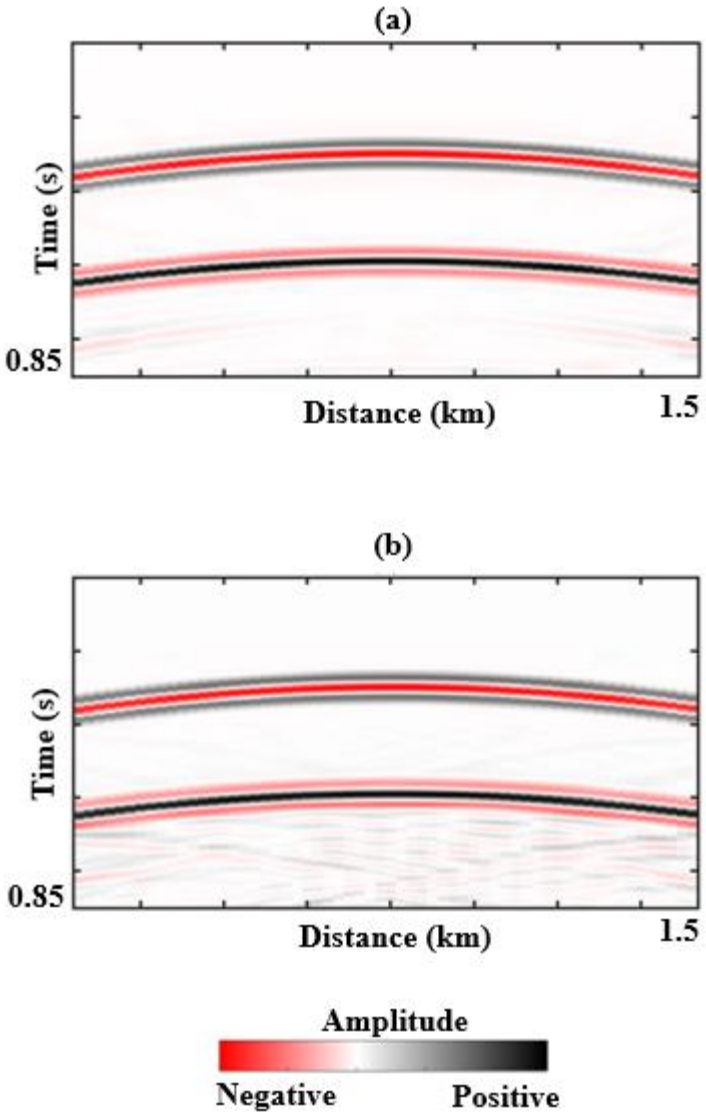

Figure 4.6. (a) Shot gather modeled using the model in Figure 4.3b. (b) Shot gather modeled using the model with irregular fracture spacing. The gather generated using the irregular fracture model shows scattering under the second reflection. The factor that controls the scattering include the fracture stiffness, frequency of the wavelet, fracture spacing and elastic properties of the host medium.

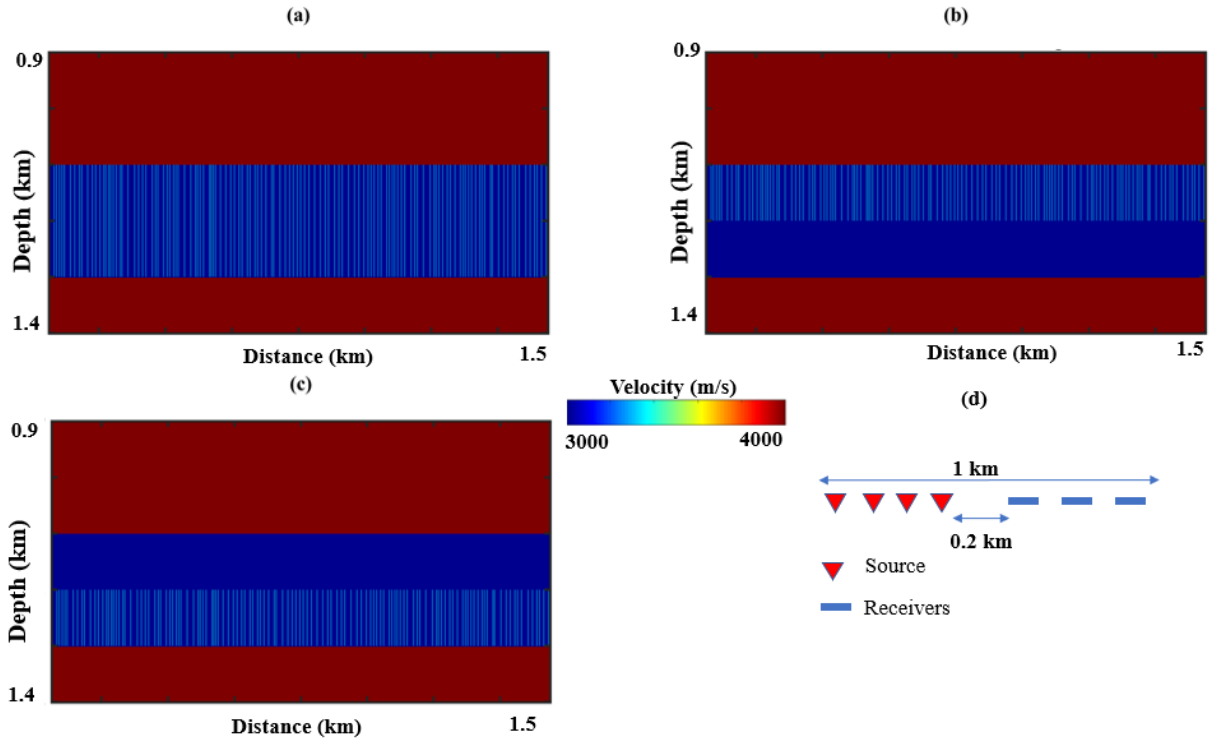

Figure 4.7. Velocity model in depth with irregularly spaced fractures (a) unconfined. (b) confined top of the formation. (c) confined to bottom of the formation. (d) acquisition geometry.

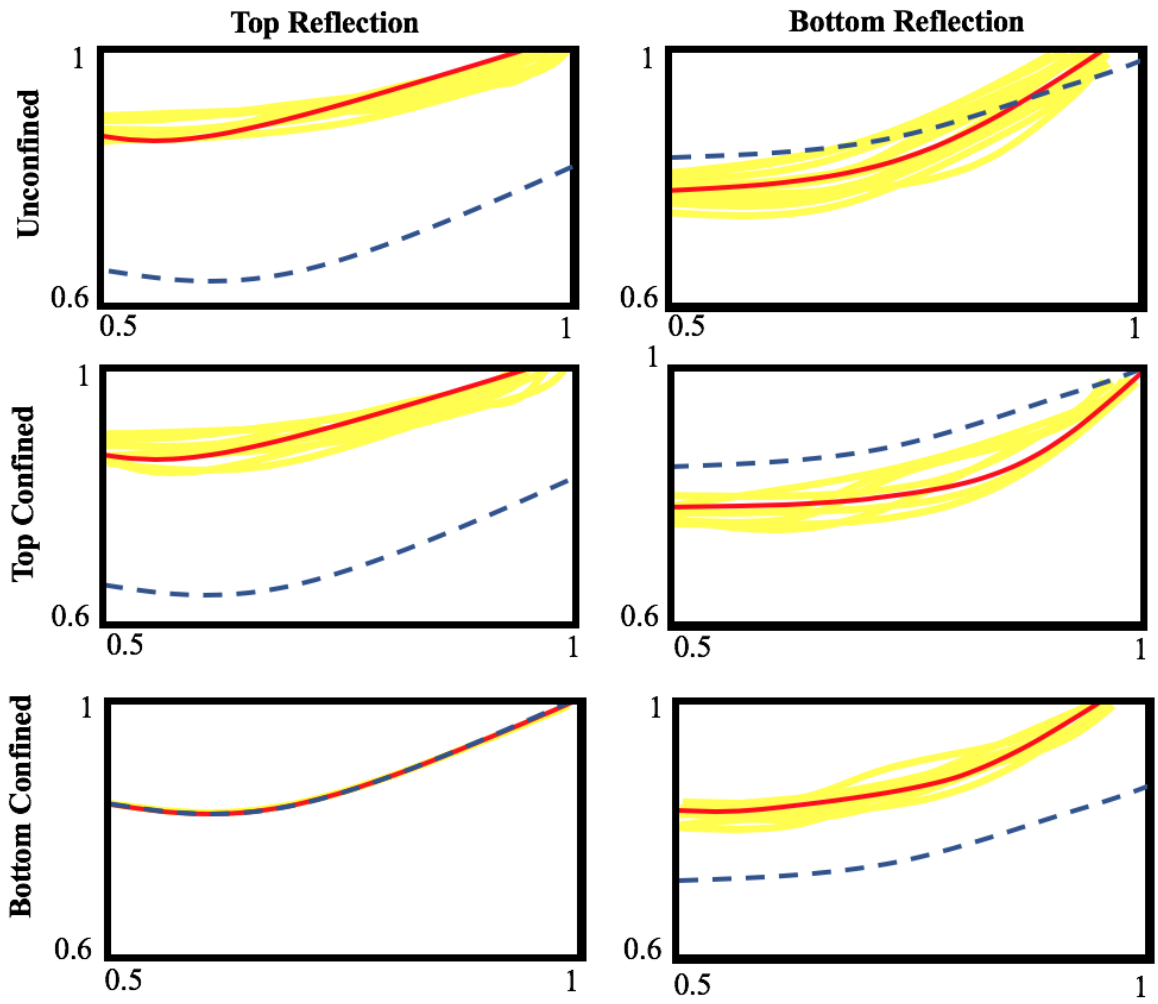

Figure 4.8. The P-wave normalized amplitude comparison between the isotropic (blue), regular fracture spacing of 12 meters (red) and irregular fracture spacing (yellow) for 30 simulation models generated using equation 4.

References

Bakulin, A., V. Grechka, and I. Tsvankin, 2000, Estimation of fracture parameters from reflection seismic data Part I: HTI model due to a single fracture set: Geophysics, **65**,1788-1802.

Berkovitch, A., I. Belfer, Y. Hassin, and E. Landa, 2009, Diffraction imaging by multi-focusing: Geophysics, **74**, no. 6, WCA75-WCA81.

Crampin S., 1981, A review of wave motion in anisotropic and cracked elastic-media: Wave Motion, **3**, 142-152.

Chopra, S., and K. J. Marfurt, 2007, Seismic attributes for prospect identification and reservoir characterization: SEG.

Cui, X., L. Lines, E. S. Krebes, and S. Peng, 2018, Seismic Forward Modeling of Fractures and Fractured Medium Inversion: Springer.

Decker, L. A., 2014, Seismic Diffraction Imaging Methods and Applications: PhD thesis, University of Texas at Austin.

Delbecq, F., J. Downton, and M. Letizia, 2013, A Math-free Look at Azimuthal Surface Seismic Techniques: CSEG Recorder, 21-31.

Dong, W., and M. E. Davidson, 2003, Quantifying 3D acquisition adequacy for azimuthal AVO analysis: The Leading Edge, **22**, 476-480.

Fang, X., M. C. Fehler, T. Chen, D. R. Burns, and Z. Zhu, 2013, Sensitivity analysis of fracture scattering: Geophysics, 78, no. 1, T1–T10,

Fang, X., Y. Zheng, and M. C. Fehler, 2017, Fracture clustering effect on amplitude variation with offset and azimuth analyses: Geophysics, **82**, no. 1, N13-N25.

Gray, D., 2008, Fracture Detection using 3D seismic Azimuthal AVO: CSEG Recorder, 39-49.

Grechka, V., 2014, Seismic characterization of fractured reservoirs: Encyclopedia of Exploration Geophysics, C1_1-C1_12.

Grechka, V. and M. Kachanov, 2006, Effective elasticity of rocks with closely spaced and intersecting cracks: Geophysics, **71**, no. 4, D85–D91

Hudson, J. A., 1980, Overall properties of a cracked solid: Math. Proc. Camb. Phil. Soc., **88**, 371–384.

Kostyukevych, A., N. Marmalevskyi, Y. Roganov, and V. Tulchinsky, 2008, Anisotropic 2.5D - 3C finite-difference modeling: 70th Annual Conference and Exhibition, EAGE, Extended Abstract, P043.

Liu, E., M. Johns, G. Zelewski, W. A. Burnett, X. Wu and J. Zhang, 2015, Fracture Characterization by integrating seismic-Derived attributes including anisotropy and diffraction imaging with borehole fracture data in an offshore carbonate field: Proceedings of the International Petroleum Technology Conference.

Liu, E., M. K. Johns, G. Zelewski, W. A. Burnett, J. Zhang, X. Wu and G. L. Skeith, 2016, Effects of overburden and thin layers on fracture-induced azimuthal AVO response: 86th Annual International Meeting, SEG, Expanded Abstracts, 347-351.

Liu, E., and A. Martinez, 2012, Seismic fracture characterization: Concepts and practical application: EAGE.

Liu, E., G. Zelewski, C. P. Lu, J. M. Reilly, and Z. J. Shevchek, 2011, Mitigation of overburden effects in fracture prediction using azimuthal AVO analysis: An example from a Middle East carbonate field: The Leading Edge, **30**, 750-756.

Liu, Y., N. Dong, M. Fehler, X. Fang, and X. Liu, 2015, Estimating the fracture density of small-scale vertical fractures when large-scale vertical fractures are present: Journal of Geophysics and Engineering, 12, 311-320.

Lynn, H. B., Bates, C. R., Simon, K. M., and van Dok, R., 1995, The effects of azimuthal anisotropy in P-wave 3-D seismic: 65th Annual International Meeting, SEG, Expanded Abstracts, 723-730.

Milad, B., and R. Slatt, 2018, Impact of Lithofacies Variations and Structural Changes on Natural Fracture Distributions: Interpretation, **6**, no. 4, 1-15

Milad, B., S. Ghosh, and R. M. Slatt. 2018, Comparison of rock and natural fracture attributes in karsted and non-karsted Hunton Group Limestone: Ada and Fittstown area, Oklahoma: Shale Shaker, **69**, no. 2, 70-86.

Mueller, M., 1991, Prediction of lateral variability in fracture intensity using multi-component shear-wave surface seismic as a precursor to horizontal drilling in the Austin Chalk: Geophysical Journal International, **107**, 409-415.

Ogiesoba, O. C., and A. Klokov, 2017, Examples of seismic diffraction imaging from the Austin Chalk and Eagle Ford Shale, Maverick Basin, South Texas: Journal of Petroleum Science and Engineering, **157**, 248-263.

Rauch-Davies, M., Deev, K., Pelman, D., and Kachkachev-Shuifer, M., 2014, Diffraction imaging applied to pre-existing 3D seismic data to map fracture corridors in an unconventional play: First break, **32**, 87-90

Rüger, A., and I. Tsvankin, 1997, Using AVO for fracture detection: Analytic basis and practical solutions: The Leading Edge, **16**, 1429-1434.

Schoenberg M. A., 1980, Elastic wave behavior across linear slip interfaces: The Journal of the Acoustical Society of America, **68,** 1516–21

Schoenberg, M. A., and C. M. Sayers, 1995, Seismic anisotropy of fractured rock: Geophysics, **60**, 204-211.

Schuster, G. T., G. Dutta, and J. Li, 2017, Resolution limits of migration and linearized waveform inversion images in a lossy medium: Geophysical Journal International, **209**,1612-1621.

Sturzu, I., A. M. Popovici, T. J. Moser, and S. Sudhakar, 2015, Diffraction imaging in fractured carbonates and unconventional shales: Interpretation, **3**, SF69-SF79.

Sturzu, I., A. M. Popovici, M. A. Pelissier, J. M. Wolak, and T. J. Moser, 2014, Diffraction imaging of the Eagle Ford shale: First Break, **32**, 49-59.

Thomsen, L., 1986, Weak elastic anisotropy: Geophysics, **51**, 1954-1966.

Appendix A

In this appendix, we give a brief background on the motivations behind this work and provide additional model results to support our analysis. This effort started as a collaboration with Marathon oil company to understand the effectiveness of AVAz and diffraction imaging in characterizing fractures. In particular, Marathon geophysicists want to investigate how the thickness, velocity and fracture intensity of the reservoir change the seismic amplitude. Understanding the effects of these factors requires us to show the basic limits of seismic resolution. Ultimately, the goal is to compliment the results from the well logs through seismic forward modeling. We summarize our findings on the benefits and limitations of using finite difference algorithm to model fractures as AVAz and diffraction imaging problems.

Amplitude Variation with Azimuth

Liu et al. (2015) used velocity, density and fracture intensity from well log to model AVAz for a marine data offshore of the United Arab Emirates. They used a reflectivity-based rather than a full-wave modeling algorithm and as a result, they did not model undesired arrivals such as multiples and P-S waves. For real data, mitigating the multiples is essential prior to any AVAz analysis. First, we constructed a 3-layer model to analyze the amplitude variation at a specific offset in three different scenarios: unconfined fractures, confined fractures the top and the bottom of the reservoir. Second, we generated three models to analyze the effect of the anisotropy as an overburden on a deeper isotropic/isotropic reflection as a function of azimuth. We use Δ_T =0.1 and $\Delta_N = 0.2$ to represent the anisotropy.

The models used for the first case are show in Figure A-1a to A-1c. To avoid tuning and shear-wave arrivals, we used a thick reservoir. In Figure A-1a, the whole 600 m thick layer is fractured. In the Figure A-1b, the top 300 meters of the fractured cases. In the third scenario, the bottom 300 meters of the layer is fractured A-1c. For thick reservoirs, there is a strong sensitivity in the reflection from the top and the base of the zone to where the fractures are located. Specifically, the top reflectivity is insensitive to fractures when they are confined to the bottom. The base reflection is sensitive to the location of the fracture zone in all three scenarios.

Figures A-2 shows a suite of the models constructed to examine the effect of the thickness, and the location of the anisotropic layer in the overburden. Figure A-2a, shows different models with three different thickness (10m, 50m and 150m). The anisotropic layer leaves an imprint on the deeper isotropic/ isotropic reflecting for all three thickness. A thicker anisotropic layer results in a lower amplitude deeper reflection. The maximum and minimum amplitude orientations are dependent on the thickness and positions of the fracture layer which may be another reason for the 90-degree ambiguity in determining the fracture orientation from amplitude data.

Diffraction Imaging

Using diffraction imaging to deterministically resolve the fractures changes the nature of the task at hand. We rely on 2D synthetic data to model individual diffraction and examine the controlling factors. We structure this section as follows: The diffraction imaging assumptions considered in our models are:

1- The acoustic PP wavefield are modeled and recorded only,

2- The modeling is noise free,

3- Multiples due to reflections have been successfully migrated and removed, and

4- We can separate non-specular diffraction from specular reflection.

Finite difference modeling

We use a grid size of 1 meter for Δx and Δz. Diffractions are modeled with a 2% slower velocity than the background medium. The width of the fracture/diffractor affects the amplitude generated and therefore a thicker diffractor gives a stronger seismic amplitude. For synthetic modeling, any fracture width provides good results, especially in noise free environments. The only limitations for synthetic data are that thinner fractures (< 1 meter) require a smaller grid and subsequently increase the computation time. We chose a 10 meters thick fracture because it has 5% of the reflection amplitude energy, and this representative of detectable diffraction in real data. For all the models, we use two diffractions separated by 100 meters.

To understand the detection limitations of diffraction imaging, we review the concepts of horizontal and vertical resolution for poststack data in a lossless medium. The vertical resolution for a poststack data in a lossless medium is given by Schuster et al. (2017):

$$dz = \frac{wavelength}{2} \qquad \text{(A-1)}$$

where dz is the vertical resolution and the wavelength is given by $\frac{v}{f}$ where v is the velocity and f is the frequency. With winder range of incident angle, we approach the $\frac{wavelength}{4}$. Figure A-3a demonstrate how to approach the maximum resolution, and includes faults with the following throws 100, 40 and 5 meters. For faults to be deterministically detected on conventional reflection seismic data, they need to be above be a quarter of the dominant wavelength or more. For our

numerical example, this occurs for the fault with a throw of 34 meters and above. We can detect separate diffractions from the top and bottom of the feature for larger throw faults such as the 100-meter fault. As we approach a quarter of the wavelength, the scattering from top and bottom interfere, and we detect the feature as a single point diffractor. Such faults cause reflection peaks to line up against troughs at the location of the fault (Figure A-3b). Smaller faults can still produce a recognizable displacement in the reflection. Finally, the fault with a throw of 5 meters or less appears difficult to detect. Using diffraction imaging, we can detect the 100 m and 40 m throw faults but may struggle with the 5 meters throw because it has a low amplitude and could be masked by the background noise.

The horizontal resolution for a poststack lossless medium is given by Schuster et al. (2017):

$$dx = \frac{wavelength}{2}\frac{z_0}{L} \qquad \text{(A-2)}$$

where dx is the lateral resolution and L is the migration aperture. From equation A-2 we conclude that shallower depths and smaller wavelengths result in increased horizontal resolution. The migration aperture is inversely proportional to the horizontal resolution, whereby a shorter aperture smears the diffractions and reduces the lateral resolution. For real data the aperture is a little more complex. Large apertures will not only increase the computation time but also in poor signal to noise ratio and degrade the migration quality. Two nearby fractures are resolved when the horizontal resolution identifies them as two separate events. We examine the influence of migration aperture in Figure A-4. In Figure A-4b we use a 1100-meter aperture and find the two diffractors are not resolved. In Figure A-4c, we use a 2250-meter aperture and can resolve the two diffractions.

Next, we examine the effect of velocity inaccuracy on horizontal resolution. We generate three models with a 5% slower, correct and 5% faster velocities. Velocity inaccuracy can push the energy up for slow velocity (Figure A-5a) or down for faster velocity (Figure A-5b). Also, it causes the energy of the diffractor in the image domain to be smeared to appear as a smile or a frown. Therefore, velocity inaccuracy reduces the horizontal resolution and the ability to resolve the features is no longer valid. Whereas an error in the overburden velocity may not necessarily reduce the resolution but it may move the diffraction location laterally.

Confined vs unconfined fractures

Next, we construct a 3-layer model based on well log obtained from Marathon company. The model consists of an overburden, a carbonate formation and a half space (Figure A-4-6a). We insert two diffractors 100 meters apart in the target tight mudrock and examine the following three scenarios: First, unconfined diffractors that cuts through the entire target formation (150m thick). Second, the fractures are 75 m long and confined to the bottom of the target. Finally, the fractures are 75 meters long and confined to the top of the mudrock. We also compute the envelope for the three cases given by:

$$e(x,t) = \sqrt{r(x,t)^2 + r^H(x,t)^2}$$

where $r(x,t)$ is the original trace and $r^H(x,t)$ is its Hilbert transform. Note the unconfined diffractions have more significant effect on the amplitude at the bottom of the diffractor (Figure A-6b). A confined fracture to the lower mudrock is more pronounced than a fracture confined to the top and hence can be imaged better both on the imaged data and the attribute (Figure A-7b). Further, the strength of the envelope can give an indication of the location of the fracture but is not

conclusive. The stronger diffraction amplitude seen at the bottom is driven by the contrast between the fracture and the bottom layer. For closely spaced fractures (below seismic horizontal resolution), the destructive interference may smear the amplitude and attribute. Distinguishing the models in that case using diffraction imaging results can be challenging.

18-layers model

Carbonate formation are often vertically stacked which adds an undesired complexity, creating a significant interbed multiples which can mark the deeper diffractions within the limited resolution. To illustrate how marking due to shallower fractures influences the amplitude, we examine the following three scenarios: Fractures located in the carbonate, the mudrock formation and both formations. Figure A-8a shows a zoomed portion of the model with the layers highlighted. Although interbed multiples due to reflections have been suppressed, we still observe multiples due to the diffractions. We also see a strong bottom reflection due to the strong velocity contrast at the base of the carbonate (Figure A-8b). Figure (A-8c) shows the imaged diffraction in the mudrock. Weaker multiples still existed due to the reverberations within the diffractors. Finally, in Figure (A-8d) the fracture located in the carbonate has masked the fracture at the top of the mudrock where the vertical resolution limit, the thickness from the top of the carbonate to the top of the mudrock is 50 meters. The vertical resolution according to equation (A-1) is 66 meters. With more sources and wider azimuth acquisition in the field, we may achieve a finer resolution and hence map the fractures better.

For real data, factors like noise, data quality, acquisition parameters and processing can suppress low amplitude small-scale fractures. Diffraction imaged real data are usually noisy because of the low amplitude of diffractions compared with background noise.

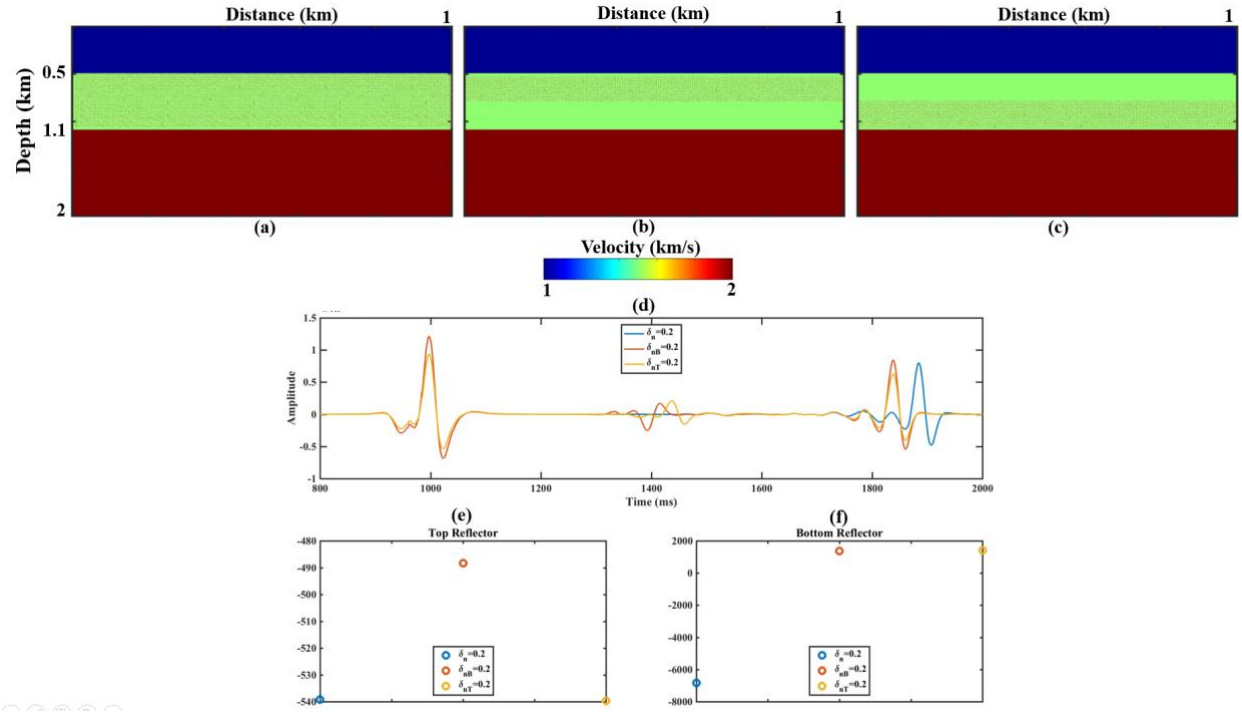

Figure A-1. Velocity model in depth with the middle layer(a) fully fracture (b) top 300 meters (c) bottom 300 meters. (d) Seismic trace at offset (750m), blue for fully fractured, red for bottom fractured, and yellow for top fractured. (e) Average amplitude for the top reflection. (f) Average amplitude for the bottom reflection. Although the maximum reflection for the bottom reflection of the red trace (bottom fracture) looks larger, it has the same average amplitude.

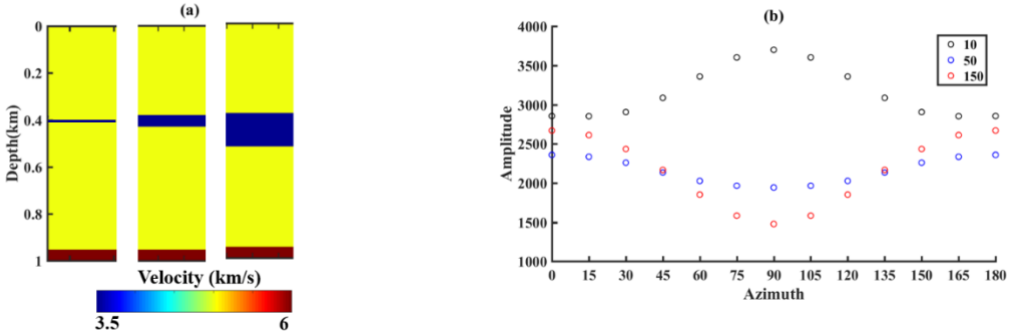

Figure A-2. A varying thickness anisotropic layer influences the deeper isotropic/isotropic reflection and gives a different amplitude signature. (a) Three models with different thickness fractured layer in blue. From the left the thickness of the layer is given as (10, 50 and 150 meters). (b) The variation of the amplitude as a function of azimuth for the three-model shown in (a). The corresponding thicknesses are given in the legend. The maximum and minimum amplitude orientations are dependent on the thickness and positions of the fracture layer which maybe another reason for the 90 degrees ambiguity in determining the fracture orientation from amplitude data

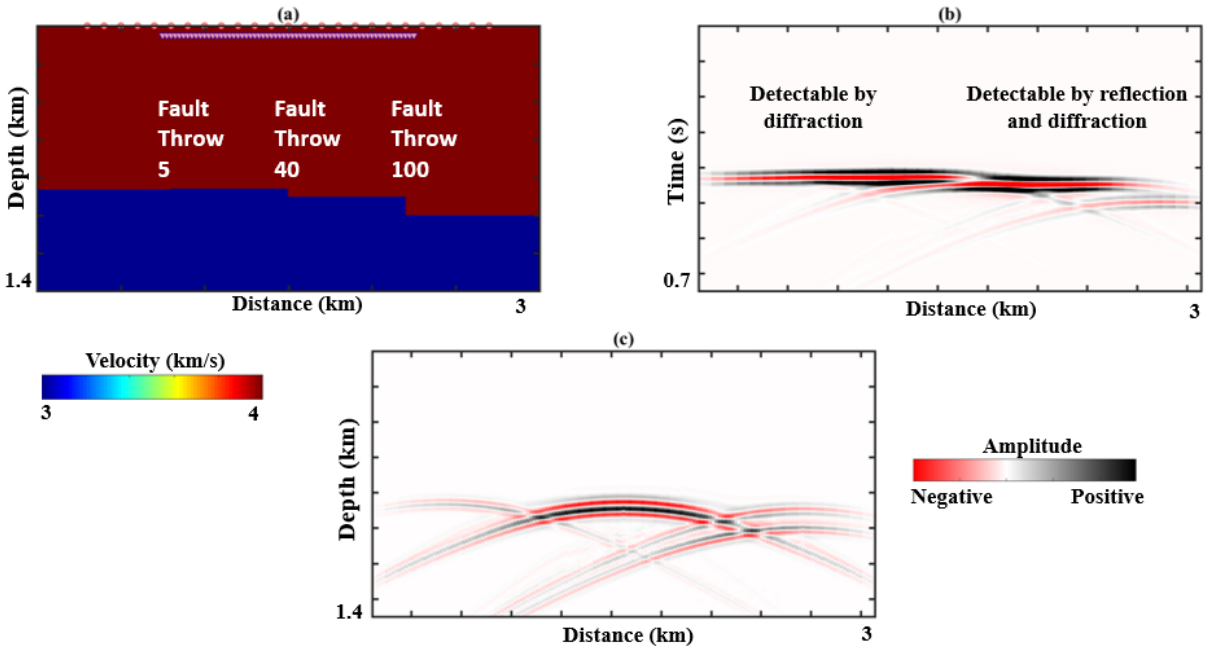

Figure A-3. (a)The model with 3 vertical faults cutting through a single reflector. From left to right, the fault throws are 5 meters, 40 meters and 100 meters. These faults correspond to 1/20, 2/5 and 1 the dominant wavelength. Sources (circle) and receivers (triangles) are placed on the surface. For better visualization, we pushed the receiver deeper to distinguish both. (b) the CMP stack of the seismic data. Each fault produces a diffraction from the top and the base of the diffraction. The two faults at the far right produce detectable change to the reflection. The smaller fault with 5 meters does not produces any detectable displacement. (c) shows diffractions modeled in the absences of the reflection. Using ideal diffraction imaging, all these faults are detectable.

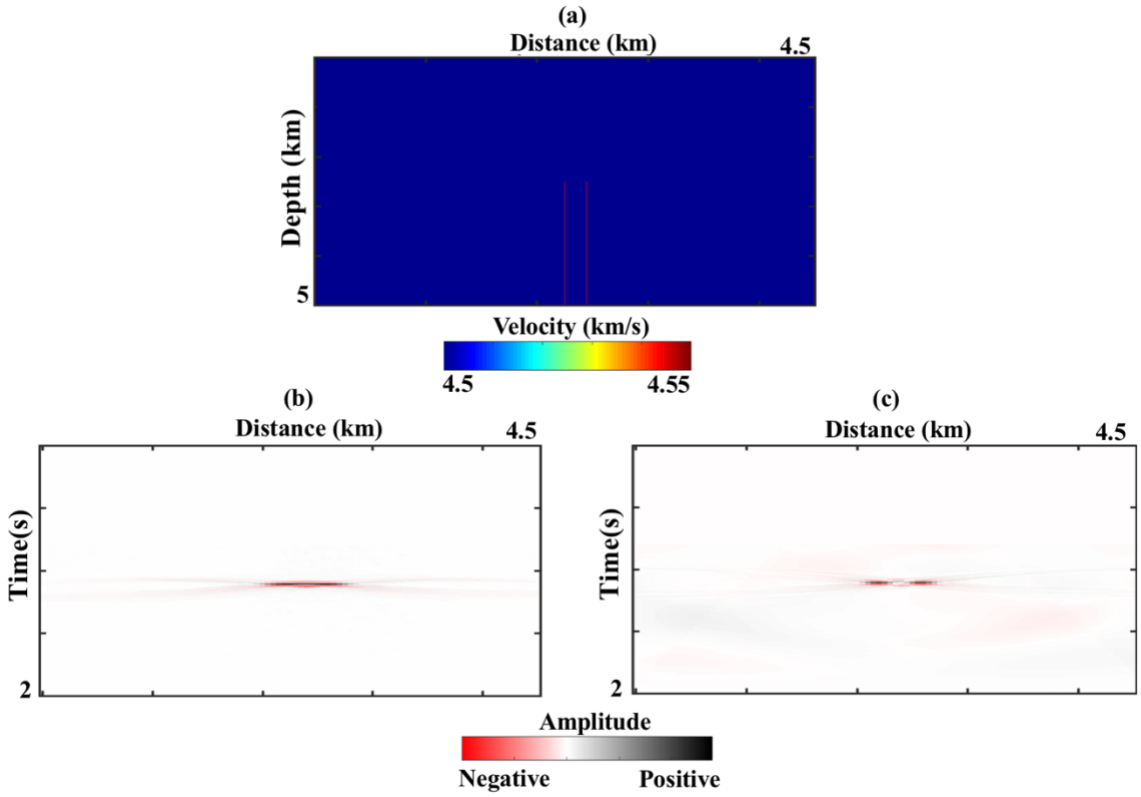

Figure A-5. (a)Velocity model in depth. (b) Migrated data using a 1125 m aperture. (c) Migrated result using a 2250 meters aperture. The x-shaped impulse is a result of imaging the diffraction with limited wavenumber (incident angles). Increasing the incident angles results in reducing this effect.

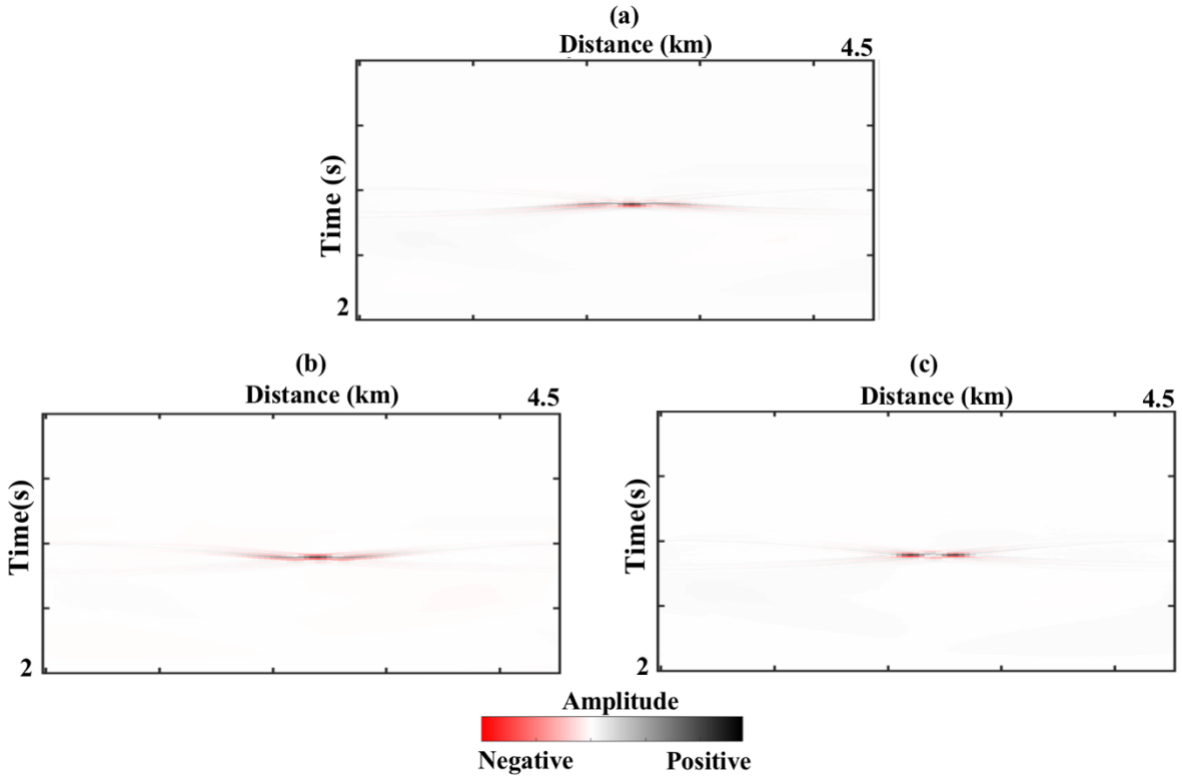

Figure A-5. We show here the migrated results shown in Figure A-4-3c using (a)5% slower velocity. (b) 5% faster velocity and (c) the correct velocity. An error in the velocity reduces the horizontal resolution and affect the ability to resolve the two fractures. Velocity inaccuracy in the overburden can also shift the resolved feature laterally.

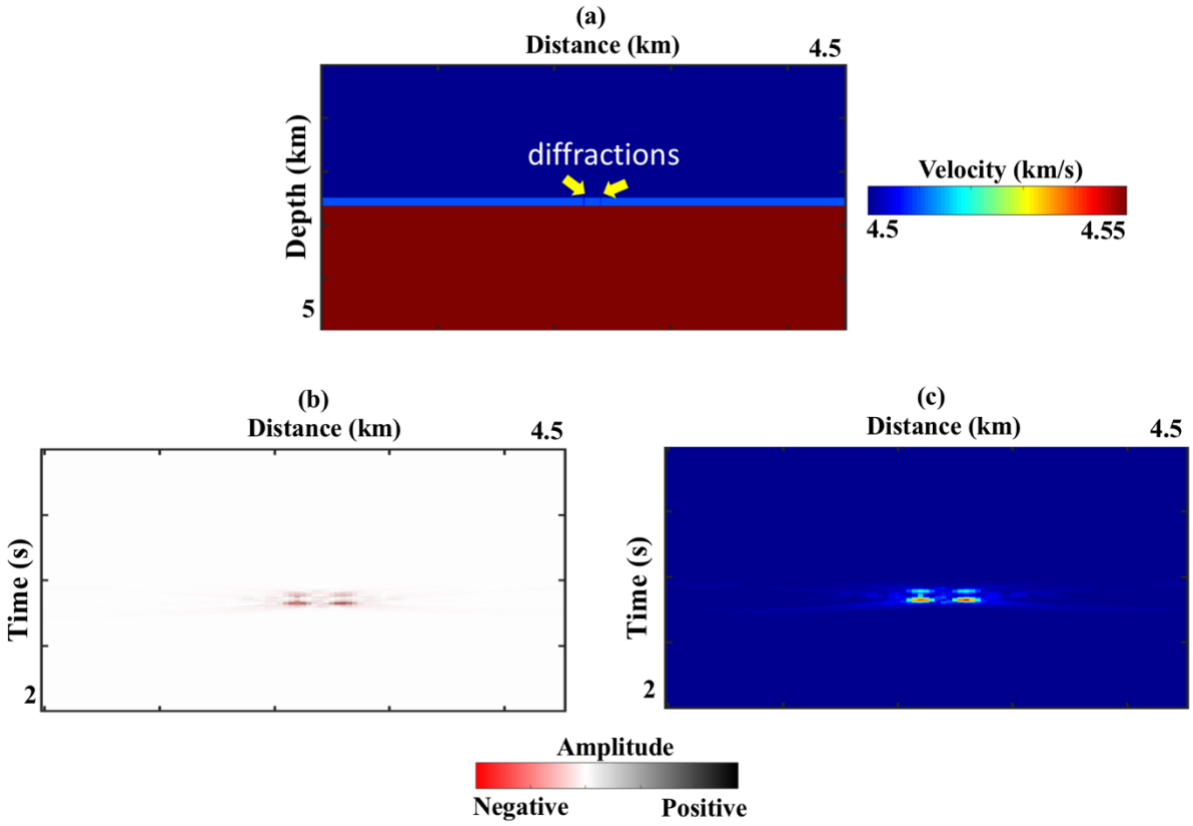

Figure A-6. (a) Velocity model in depth with two 10 meters thick fractures located in the middle layer (mudrock). The fractures are separated by 100 meters. (b) Diffraction imaged section due to unconfined fractures (cut through the whole layer). (c) Instantaneous envelope computed on the data shown in (b).

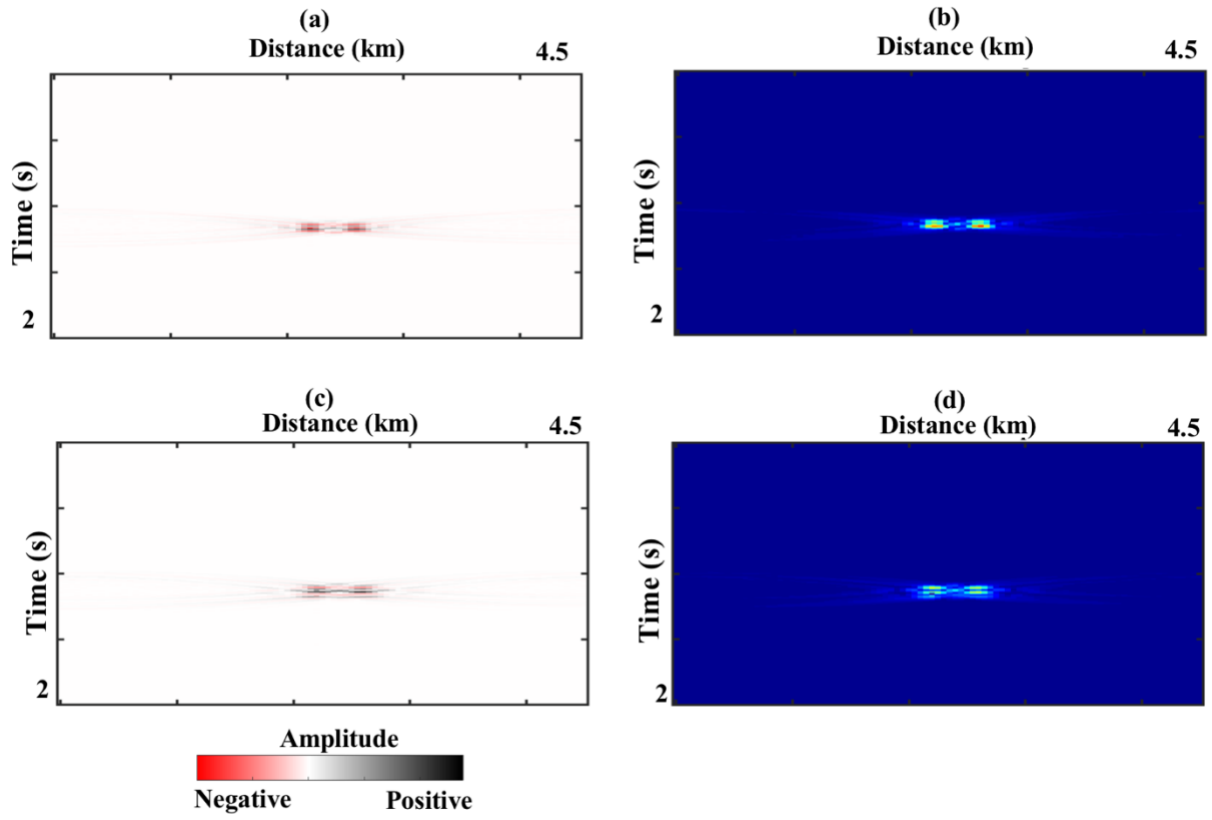

Figure A-7. (a) Diffraction imaged data using fractured confined to the bottom of the middle layer (top 75 meters). (b) Instantaneous envelope computed using (a). (c) Diffraction imaged data for fractures confined at the top of the middle layer (bottom 75 meters). (d) Instantaneous envelope computed using (c).

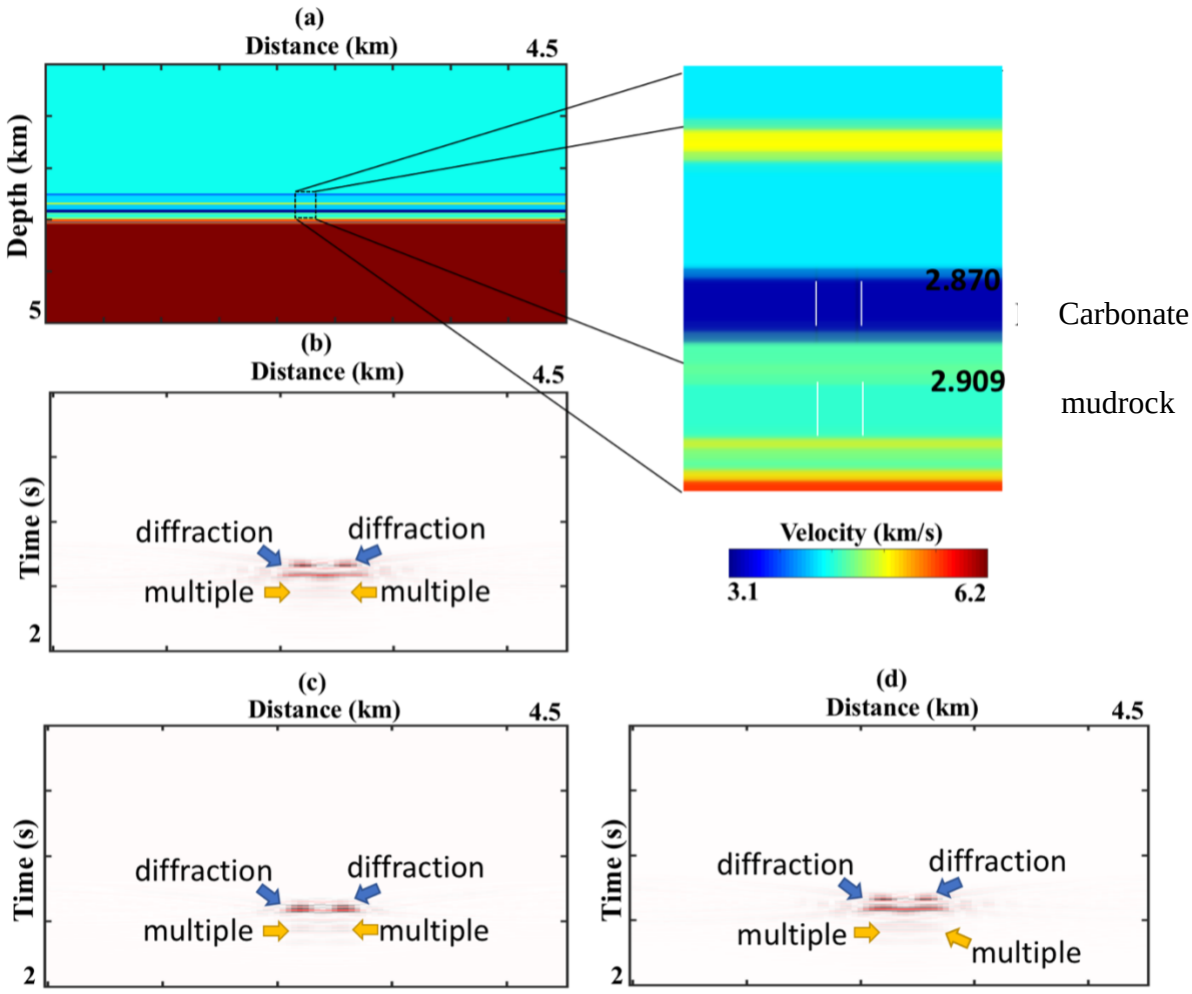

Figure A-8. (a) An 18-layers model based on well logs data obtained from Marathon with a close up of the formation of interest. We generated three model with fractured Carbonate, mudrock and both. For all cases, we use two fractures with 10 meters thickness and 100 meters apart. (b) Diffraction imaged section generated using the fractured Carbonate model. (c) Diffraction imaged section generated using the fractured mudrock model. (d) Diffraction imaged section generated using fractured Carbonate and mudrock formations. The blow arrows indicate the top of the diffractions which is easily seen on the three imaged sections. The diffraction from the bottom is more continuous when the Carbonate is fractured. This can be explained by stronger reverberation due to the strong contrast at the base. When both formations are fractured, the diffractions from the Carbonate masks the deeper diffractions. This can be explained by the concept of vertical resolution. If the two layers are within the limit of the vertical resolution, diffraction imaging will fail to separate the two.

Chapter 5: Sensitivity Analysis of Velocity with Diffracting Focusing in the Image Domain

Abdulmohsen Alali, Nori Nakata and Kurt Marfurt

The University of Oklahoma, ConocoPhillips School of Geology and Geophysics.

Submitted as an extended abstract for the SEG annual meeting 2017

The paper will be submitted to the EAGE journal of geophysical prospecting

Abstract

Diffractions provide valuable information about local discontinuities and other small-scale variations in the subsurface. Most velocity analysis workflows, from simple semblance scans of CMP gathers to more sophisticated tomographic analysis, emphasize the contribution of specular reflections. In this study, we evaluate the greater sensitivity of diffractions to errors in the velocity model as a potential high-resolution velocity analysis tool. Our analysis consists of two steps. First, we analyze the velocity errors based on the focused energy of diffracted events in the image-domain. For a single common shot image, maximum focusing (measured as the maximum energy at a given subsurface image point) occurs when the diffraction is imaged with the correct velocity. The diffractor can be distinguished even in a heterogenous medium. We improve upon this initial observation by cross-correlating multiple nearby shot images and find that the cross-correlation of the images is not only maximum but also laterally symmetric for the correct velocity. We combine these observations to construct an objective function, which can be used to estimate velocity errors in the image-domain. We evaluate the efficacy of thee method using simple and complex 2D wave equation synthetic models followed by reverse time migration.

Introduction

Recorded seismic waves are either reflected or diffracted, depending on the geometry of the subsurface structures. Diffractions are indicators of small-scale faults, pinch-outs, karst, reef edges and sudden changes in facies (Krey, 1952). In general, diffractions exhibit lower energy than specular reflections (Klem-Musatov, 1994). In addition, conventional seismic data processing parameters are selected to enhance the energy of specular reflections and may be suboptimal in imaging diffractions. Nonetheless, the proper imaging of diffractions results in improved fault terminations needed for structural interpretation and onlap and downlap patterns needed for

sequence stratigraphic interpretation. The greater sensitivity of diffractions to velocity make them an excellent candidate to further improve an initially velocity model based on specular reflections. A major challenge in utilizing diffractions is in detecting them. Landa et al. (1987) proposed a method of detecting diffractions imaged by common-offset sorted gathers. Fomel et al. (2007) separated seismic diffractions from reflections using plane-wave destruction which relies on the continuity of the local slope of the reflection in the stacked section. Once separated, they found an optimal velocity to image the diffractions using a local focusing algorithm. Khaidukov et al. (2004) proposed a focusing-defocusing technique in the post-stack domain, whereby they focus the reflection to a point while the diffraction remains unfocused over a large area. Then, they suppress the focused reflection and defocus the diffractions. Moser and Howard (2008) studied the sensitivity of the diffraction to the small-scale scatter in the context of depth imaging and modified the migration kernel to directly image the diffractions. Decker et al. (2017) implemented a semblance-weighted least-squares migration to enhance the imaged diffraction.

Other scholars have explored the use of diffractions in analyzing and updating the velocity model. Harlan et al. (1984) used slant stacking to suppress the reflections then migrated the diffractions until the maximum focusing was reached. Sava et al. (2004) updated the interval velocity using the focusing and defocusing of diffractions and reflections by analyzing residual diffraction focusing in physical space using prestack residual migration. Huang et al. (2015) concluded that tomograms inverted using diffraction energy significantly improved the resolution of the velocity model obtained from using only specular reflection because the first Fresnel zone of diffracted waves is only 70% the size of that from specular reflections. Khoshnava et al. (2018) analyzed the diffraction moveout approximation in the presence of anisotropy. They also examined the different anisotropic diffraction travel time approximation on several 2D examples with VTI

anisotropy. They found that ignoring the anisotropy can result in low-resolution images with wrongly position or spurious diffractions

These studies indicate that diffractions can be used to assess inaccuracies in the migration velocity model. The most common technique to analyze the velocity of reflections in the image domain is Al-Yahya's (1989) migration velocity analysis (MVA). MVA indicates that the correct velocity will give the same image for collections of sources and receivers. If traces at the same point but imaged from different geometries are plotted side by side, the accuracy of the migration velocity is measured by the consistency (or "flatness") of the common image gathers (CIGs). Sava et al. (2005) suggested a different migration velocity analysis in the image domain by incorporating the focusing of diffractions. Beginning with a suboptimally focused image, they used the defocused migrated events to update the velocity. Because it is difficult to identify diffracted events on CIGs used in the MVA method, their diffraction focusing criterion is based on kinematic information in defocused diffraction and reflection.

In this paper, we build on the previous observations that diffractions are more sensitive to velocity than specular reflections. We begin introducing the theoretical background for the behavior of focused energy of diffracted events in the image-domain and image cross-correlation. Then we validate the method using numerical models with different complexity. Next, we introduce the objective function base on image cross-correlation. We conclude with an assessment of the limitations of this workflow and how one might be able to construct an interactive velocity analysis tool.

Theoretical Background

Migrated images can be constructed using a one-way downward continuation (Stolt, 1978) or two-way extrapolation reverse-time migration (RTM) (Hemon, 1978; Baysal et al., 1983). The

latter is computationally intensive but recently has become routinely used in complex marine areas such as the Gulf of Mexico and the Red Sea where it is critical to handle multipathing and even turning waves. For those advantages, we use RTM as our imaging technique of choice. We use Claerbout's (1985) imaging condition

$$R(\mathrm{x}) = \sum_t W_s(x,z,t)\, W_R(x,z,t), \qquad (1)$$

where $R(\mathrm{x})$ is the imaged section at $\mathrm{x} = (x,z)$, $W_S(x,z,t)$ and $W_R(x,z,t)$ are the receiver and source wavefields, respectively. The imaging condition in equation 1 suggests that we forward prorogate the source-generated wavefield and backward propagate the received wavefield (in this paper using a finite difference algorithm) using a velocity model in depth. At each time step we cross-correlate the two wavefields to generate the zero-lag reverse time migrated image. The term "reverse time" comes from the fact that we reverse the receiver wavefield and backpropagate it in time.

Locating diffractors

In order to locate potential diffractors, we propose a two-step workflow: First, we image the data using bulk-shifted velocities (the starting velocity multiplied by a -/+ percentage) centered around a reasonably accurate starting velocity such as the pre-stack migration velocity based on reflection events, tomography or velocity scans on CMPs pre-stack migration velocity. We repeat the imaging condition given by equation 1 using bulk-shifted velocities (Figure 5.1) where we examine the energy distribution as well as the location of the energy for a single diffraction. A velocity that is 10% too slow results in an image that is concave down but shifted too shallow (Figure 5.1). A velocity that is 10% too fast results in an image that is concave up but shifted too deep (Figure 5.1). For a velocity that is accurate velocity the diffraction is well focused at the correct location and has the highest energy in the center of the window (Figure 5.1). In the absence

of complex structure or strong lateral velocity variation, a good pre-stack time migration (PSTM) velocity should be within few percentages range of the correct velocity in the (Rauch-Davies et al., 2018).

Second, we construct a 3D matrix with each slice corresponding to the migrated section using a different velocity. Then using a window around the zone of interest defined by the processers/ interpreter the size of the dominant wavelength, we compute the sum of the envelope along the depth direction at each imaged trace following:

$$E(x) = \sum_{z0}^{z1} \sqrt{[r(x,z))]^2 + [r^H(x,z))]^2} \quad , \qquad (2)$$

where

$E(x)$ is the average intensity (sum of the envelope) at location x,

z_0 and z_1 are the depth limits considered in the summation,

$r(x,z)$ is the migrated trace, and

$r^H(x,y)$ is its Hilbert transform in z.

Zavalishin (2000) finds that the envelope removes sensitivity to the frequency and phase of the image.

The diffraction should be focused and maximum at the correct spatial and depth location for the correct velocity slice as shown in Figure 5.1. The assumption of an optimal focusing for a diffractor within our analysis window is valid under the following conditions: (1) there should only allow subsequent velocity perturbations to include the correct velocity model, and (2) processing has minimized the introduction of imaging artifacts related to statics, strong multiples, and surface waves.

Image correlation objective function

Given this suite of images, we now wish to quantify the velocity error in the image-domain. We define the error as a local cross-correlation that measures the apparent shift between two nearby experiments. Hale (2006), Hale and Cox, (2008), and Perrone et al. (2015) shifted images using

$$c_i(\mathrm{x},\lambda) = \int w(\mathrm{x}-\xi) R_i(\xi - \tfrac{\lambda}{2}) R_{i+1}(\xi - \tfrac{\lambda}{2})\, d\xi, \qquad (3)$$

where $\mathrm{x} = (x, z)$ for the 2D case,

R_i and R_{i+1} are the reference and secondary image respectively,

$\boldsymbol{\lambda}$ is a 2D vector,

ξ denote a dummy variable of integration in the correlation and is defined in space x and z ,

$and\ w$ is the local cross-correlation weighting given by

$$w(\mathrm{x}-\xi) = \exp\{\tfrac{-1}{2}\big[(z-\xi_z) + (x-\xi_x)\big)]\}. \qquad (4)$$

The choice of window size X and Z is critical for several reasons. First, we have to ensure that the diffractor is present in the window imaged of choice. A good size for the window is the maximum wavelength in the data. The weight provides a smooth transition to zero along the sides of the correlation and removes the artefacts due to abrupt truncations. The two images R_i and R_{i+1} are products from the same velocity from nearby shots. Next, we define the objective function following (Perrone et al., 2015):

$$\Im(m) = \sum \ \|c_i(\mathrm{x},\lambda)\|_{\mathrm{x}}^2, \qquad (5)$$

where m represents the velocity model parameters, the $\sum_i$ indicates we are summing over several experiment-pairs, x is the lateral coordinate of the migrated traces and $\|\ \ \|^2$ indicates the $l_2$norm. The objective function in equation 5 relies on the local coherence between nearby shots assuming they see similar portions of the model and provide comparable images. Equation 5 also evaluates the degree of similarity in semblance between images through local correlations in the image

domain. Also, requires it requires no picking a moveout or the evaluation of focusing in common-image gathers (Symes, 1991).

Numerical Validation

Locating diffractors

To demonstrate the efficiency of the method, we use three numerical models with various complexity. In all the models, we have imaged the data with the following range of velocities 10% too low, 5% too low, correct, 5% too high and 10% too high. A single source is used and the direct wavefield have been suppressed in the modeling stage because they are not of interest in this study.

Diffractor in homogenous background velocity model

Figure 5.2a shows the velocity model used to generate a diffraction in a homogenous background medium. This model is the basic scenario to observe how the sum works on a diffraction imaged using various velocities. Figure 5.2b shows the shot gather containing the diffraction after suppressing the direct wavefields. Figure 5.2c shows the imaging section using the correct velocity. Following equation 2, we sum the energy at each receiver location on each velocity slice using a 300 m window centered at the depth of the diffraction imaged by the correct velocity. We can consider the summation as a 1D filter to create a profile of the sum of envelope as a function of each migrated trace location. The normalized results are shown in Figure 5.3. As the velocity increases from 10% too slow to 10% too high, the correct velocity concentrates the intensity around the location of the diffractor. The maximum energy is reached when the velocity is correct. Exceeding the correct velocity results in reducing the normalized amplitude. The homogenous background model is not ideal to analyze the different velocity effect in focusing and locating the diffractor in Figure 5.3. To analyze how the energy changes at the diffraction locations, we plot

the normalized amplitude against velocity in Figure 5.4. The trend indicates that the diffracted energy is not symmetric when the velocity is inaccurate.

Diffractor with heterogeneous velocity

For a more complicated case, we use the von Kármán stochastic random model to build the heterogeneous background velocity model (Nakata and Beroza, 2015). The velocity change ranges from 0.2 to 1.4 km/s (Figure 5.5a). Side and back scattered waves are generated when the energy propagates through heterogeneous background medium (Figure 5.5b). Figure 5.6 shows the summation of the envelope along the receiver location normalized. The scattering interference reduced the overall amplitude at the location of the diffraction for inaccurate velocities images. The interference, however, gives a realistic representation of the method working in more realistic setting. We still achieve a pronounced focusing at the correct location when using the correct velocity.

Sigsbee model

Next, we use a portion of the Sigsbee model (Paffenholz et al., 2002) to locate diffractions in complex geology setting. Figure 5.7 shows the Sigsbee velocity model with the portion cropped for the test highlighted by the white box. Figure 5.8a shows a zoomed version of the portion considered in this example whereas Figure 5.8b shows the imaged section using the correct velocity. A single source is used to image this model and assess the validity of the method in a more realistic scenario under poor illumination. We consider the summation across the areas highlighted by the yellow box a, red box b, and green box c. Figure 5.9 shows the sum of the envelope for the yellow box. The correct velocity summation is not symmetric as the reflection

contributes to the energy sum. For the correct velocity model, the maximum value still occurs at the location of the diffractor, while for other models it does not.

Next, we implement the same analysis on the reflections in red box b. The sum of the envelope at each receiver location is shown in Figure 5.10. The maximum and minimum velocities are dominated by reflectors and show no focusing. In contrast to the sum over window a, the reflection energy constructively interferes and show no focusing that allows one to analyze the velocity variation.

Finally, we show the intensity for the poorly illuminated diffraction in box c in Figure 5.11. Even when the diffraction is poorly imaged, we still see a maximum energy at the location of the diffractor.

Image correlation objective function

In Figure 5.12 we show a simple single diffractor model imaged by the two sources in red. The source spacing is 80 meters. We use 401 receivers located on the surface with 5 meters spacing. The resulting images are shown in Figure 5.13 using the 2% fast, correct and 2% slow velocity. Using equation 3, we cross-correlate the images from the two adjacent experiments and show the result of the cross-correlation in Figure 5.14. Note the symmetric correlation image for the correct velocity and the asymmetric correlation for the inaccurate velocity models. λ_x and $\lambda_z$are the correlation lag in the image space. The preliminary results encourage us to construct an objective function following equation 5 that can be used to measure the apparent shift between two images from nearby shots. Figure 5.15 shows the values of the objective function (equation 5) for different constant perturbations of the model used for the simple example considered.

Limitations and Future Work

We demonstrate the validity of the proposed method using synthetic data with variable complexity. We also demonstrate that the use of diffractions provides a smooth objective function that can be used to update the velocity model. A potential velocity updating technique is the adjoint state method which has been demonstrated for reflection by Perrone et al. (2015). We list below the inherent limitations and suggest additional research tasks to build on this work.

First, the underlying assumptions of a single diffractor per window and low noise level require further analysis and can be the topic for a future research. We use the maximum intensity to locate potential diffraction which fails in the presence of multiple diffractions.

Second, extending the method to 3D can be demonstrated using the equations above but may become computationally intensive. For instance, the search for a maximum intensity becomes a 3D problem rather than a 2D which requires a more advanced grid search method.

Finally, for 3D data or even for a large 2D data, imaging the section using bulk-shifted velocity is not desirable to say the least. Instead, we consider this work as a complimentary technique to analyze the velocity. Instead of propagating the wavefield through the whole section, we can achieve a subsequent localized forward simulation between the scattered wavefield caused by the bulk-shifted velocity within a target area and the unchanged velocity outside the reduced absorbing boundary (Masson et al., 2017). The localized simulation requires an exact boundary condition around the area of interest and changing the nature of the problem to a target oriented inverse problem. Basically, under the localized simulation, we save the wavefield everywhere except inside a zone of interest. Since our method is based on image cross-correlation, we worry mostly about that zone of interest. Hence, we can bulk-shift the velocity inside that zone of interest.

Conclusions

Because diffractions are more sensitive to the accuracy of the velocity than reflections, diffraction focusing can be used as a velocity analysis tool. At present, the method is interactive, whereby an interpreter identifies specific diffractions (such as about faults) for further analysis. Once identified, we perturb the velocity model and sum the energy within an analysis window slightly larger than the dominant wavelength. Evaluating three synthetic models with various complexity for a single common shot gather indicates that the most energetic events occur when using the correct velocity, suggesting that this energy can be used as a quantitative measure of the quality of focusing.

Multiple shots each will give diffraction images that are sensitive to the velocity in different ways. We use image cross-correlation between nearby experiences to analyze the velocity. Analysis of our synthetic models indicates that we obtain a more symmetric cross-correlation when the velocity model is correct and an asymmetric cross-correlation when it is incorrect. We combine these observations to construct an objective function that will be amenable to differential semblance optimization solutions.

Acknowledgment

We used Madagascar open-source software (Fomel et al. 2013) for the numerical modeling and we would like to extend our gratitude to the whole Madagascar family. The first author would like to thank Saudi Aramco for sponsoring his studies.

Figures

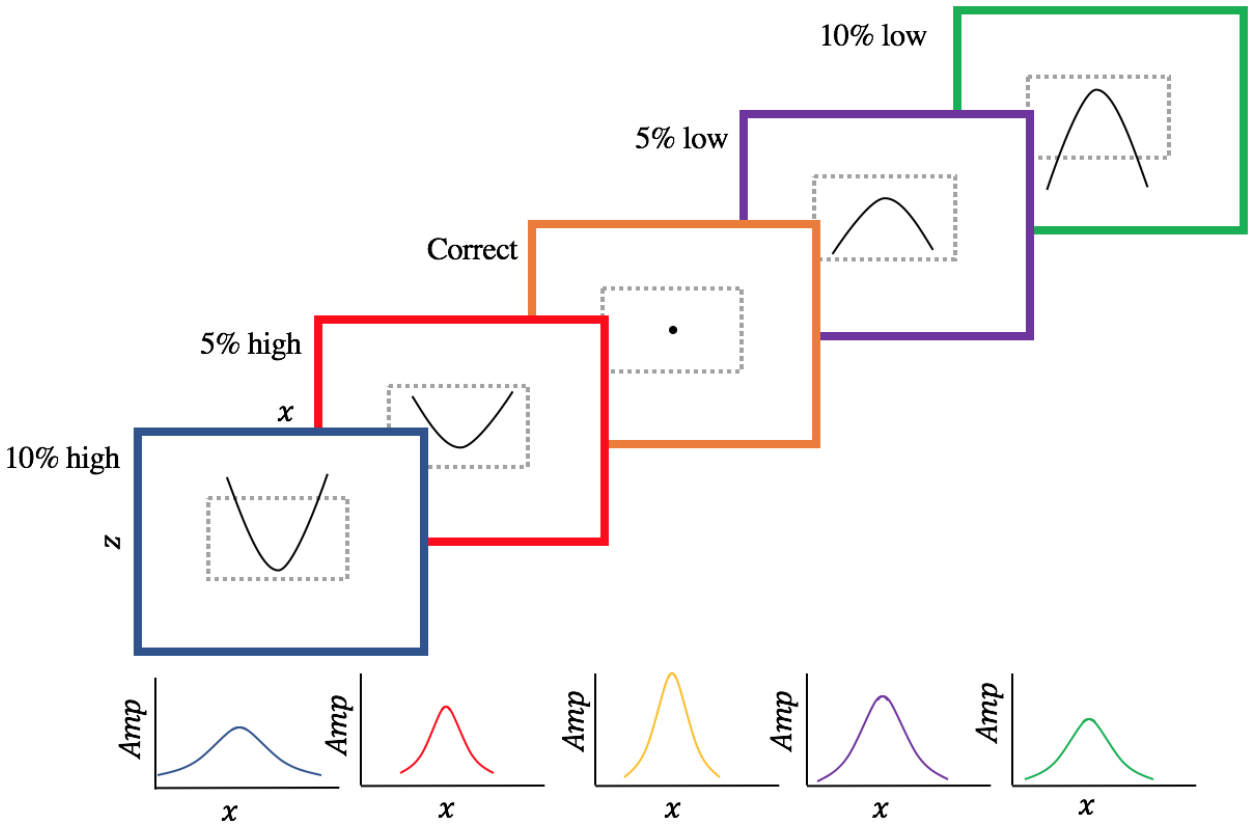

Figure 5.1. Top: Schematic cartoons of a diffraction model imaged using 10% slow, 5% slow, correct, 5% high, and 10% high velocities. The grey dashed box represents the window where we sum the energy at each image location (equation 2). The summation is done as a 1D calculation at each output migrated trace. The window should be placed around potential diffracting location. Bottom: The summation of envelope for each at each receiver normalized for each velocity slice. Because the diffraction is focused when the correct velocity is used, it gives the highest value (orange curve).

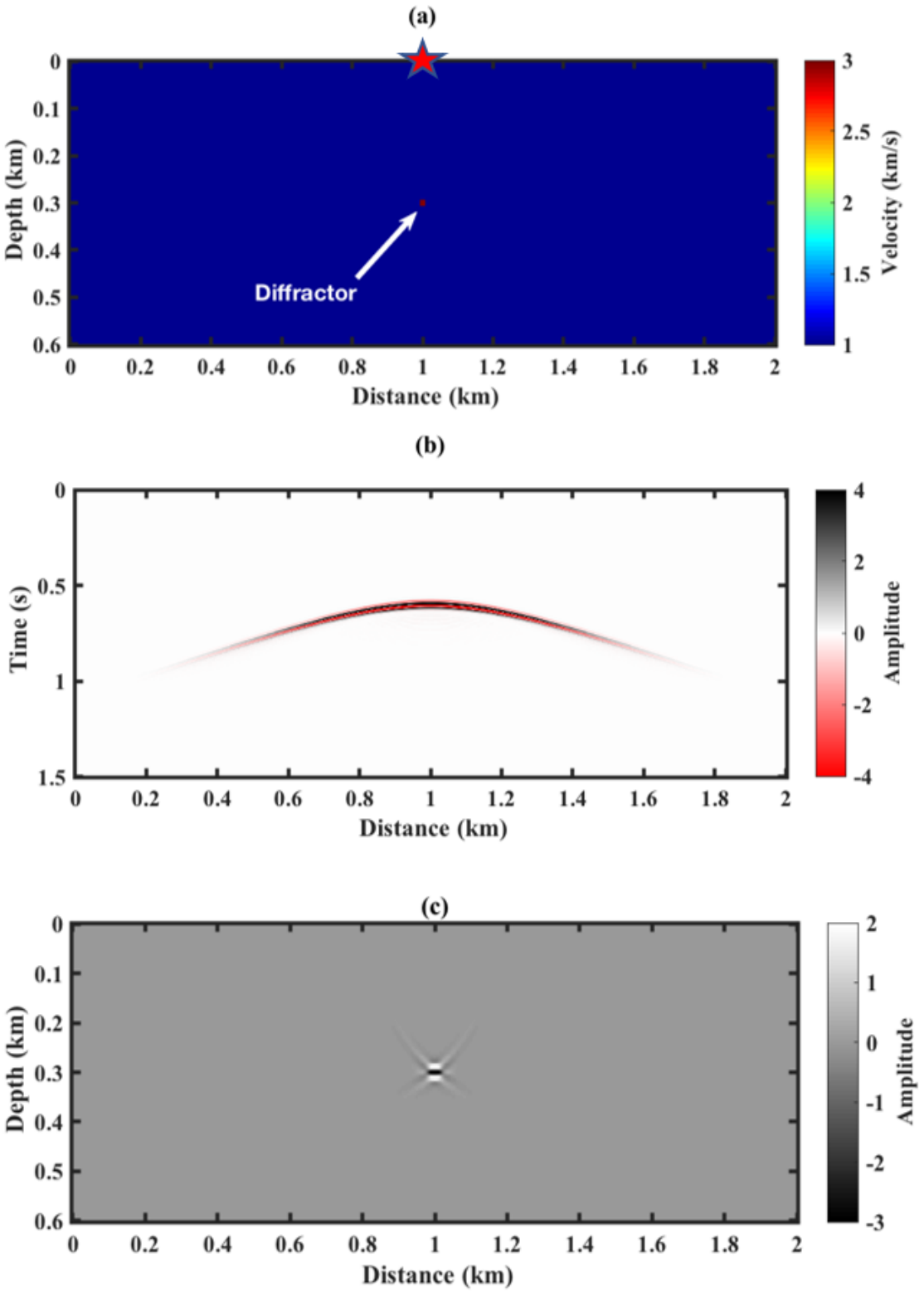

Figure 5.2. (a) A diffractor in a homogenous velocity model in depth. The red star indicates the location of the source (b) Gather generated using the model in panel (a) with direct wavefield suppressed. (c) RTM imaged gather in panel (b) using the correct velocity model.

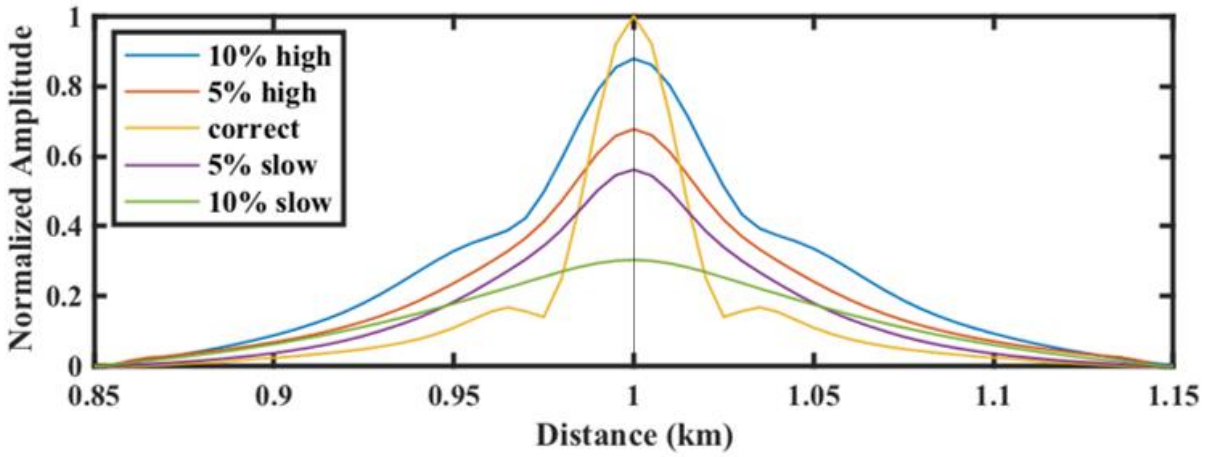

Figure 5.3. The summation of the envelope at each imaged trace for images generated using bulk-shifted velocity of the model in Figure 5.2a. We use a 300 m window centered at the depth of the diffractor in Figure 5.2c for the summation.

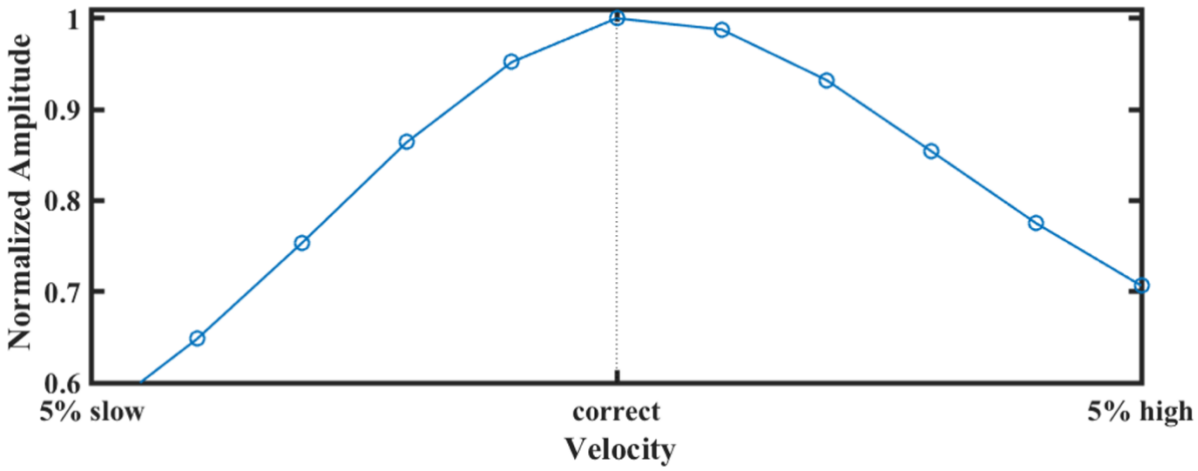

Figure 5.4. The normalized summation of the envelope at each receiver location of the diffractor (x =1 km) plotted at different velocities. The skewness is linked to the diffraction energy behavior under different velocities.

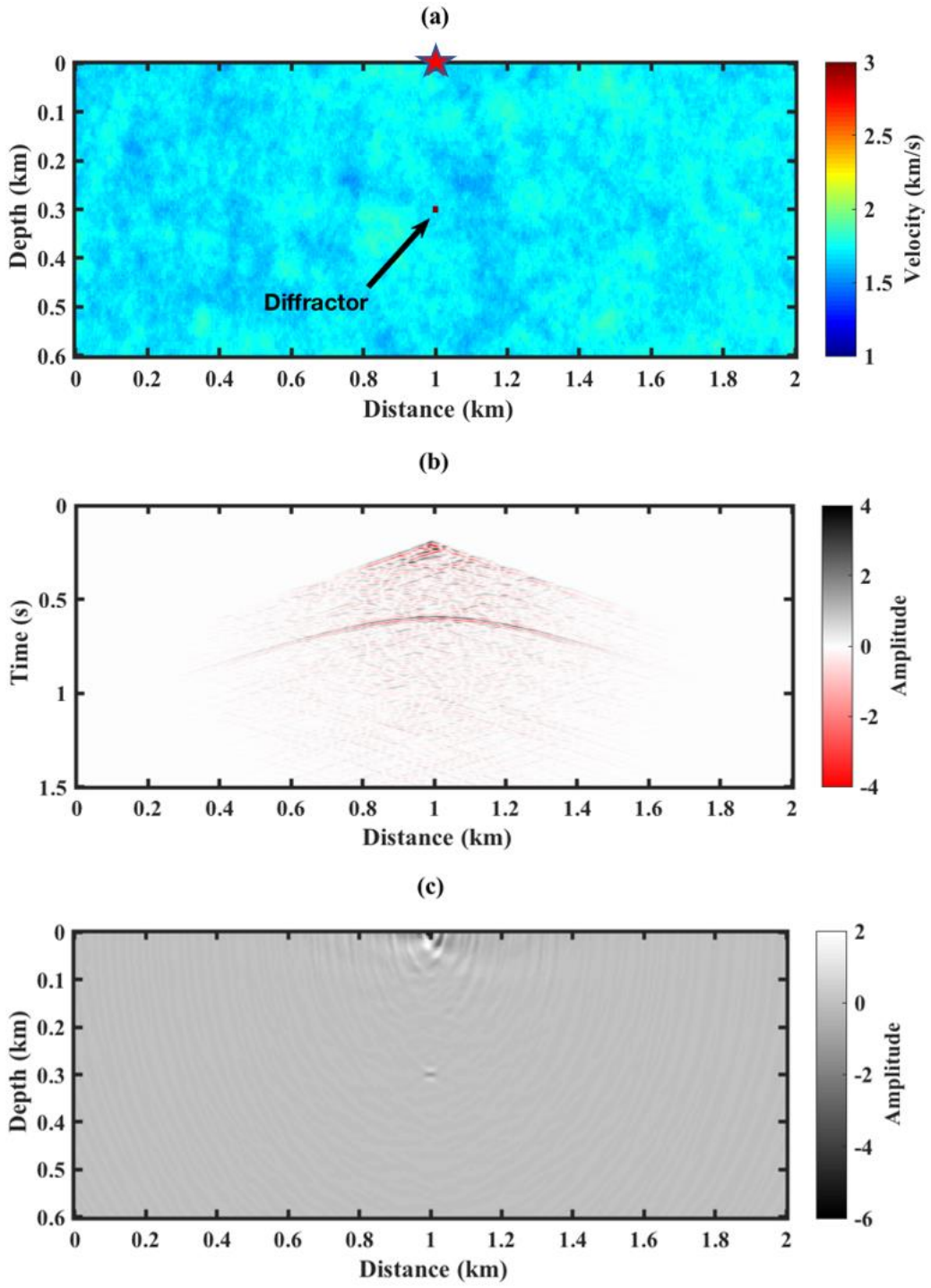

Figure 5.5. (a) Velocity model of a diffractor in a heterogeneous background. The black red star indicates the location of the source. 401 receivers are located on the surface with 5 meters spacing. (b) Gather generated using the model in panel (a) with direct wavefield suppressed. (c) RTM imaged using the correct velocity model in (a). The diffraction looks weaker due to the scattering from the background heterogenous model.

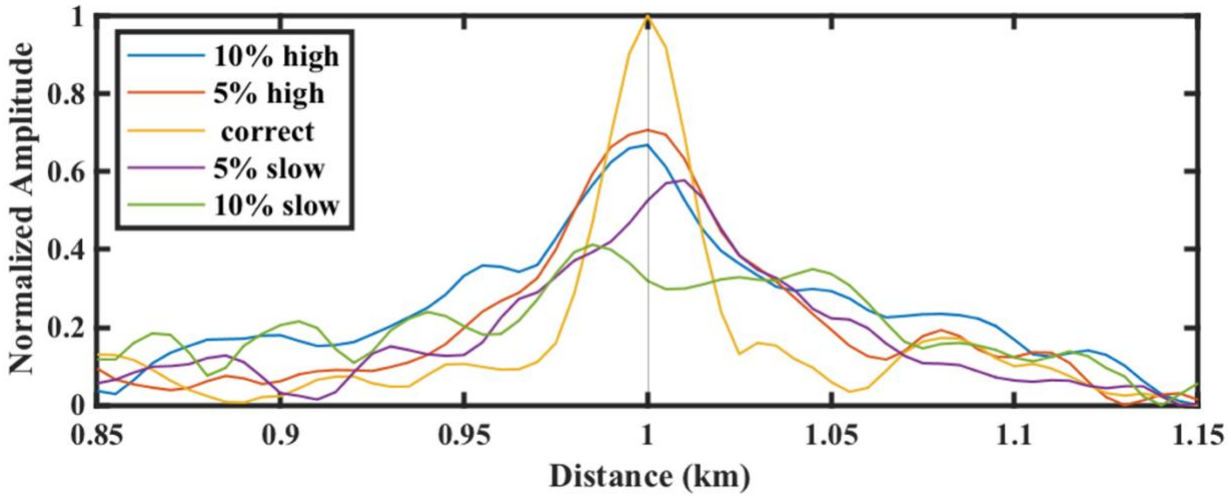

Figure 5.6. The summation of the envelope normalized at each imaged location for images generated using bulk-shifted velocity of the model in Figure 5.5a. We used a 300 m window centered at the depth of the diffractor in Figure 5.5c for the summation. The amplitudes for the ±10% velocities are lower than those shown in Figure 5.3. The highest amplitude corresponds to the correct velocity.

.

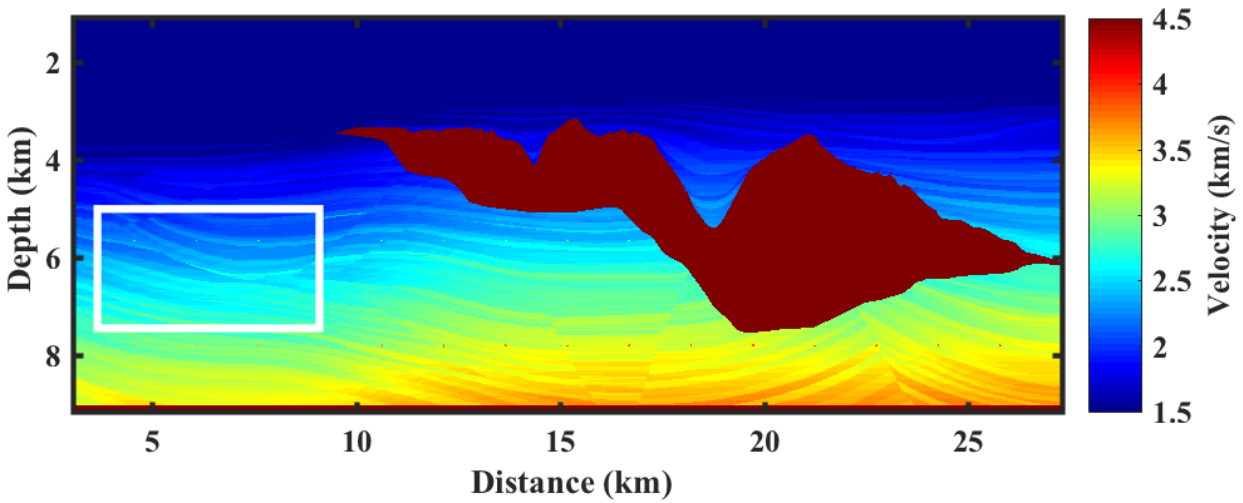

Figure 5.7. Sigsbee velocity model with the portion of interest highlighted in the white box.

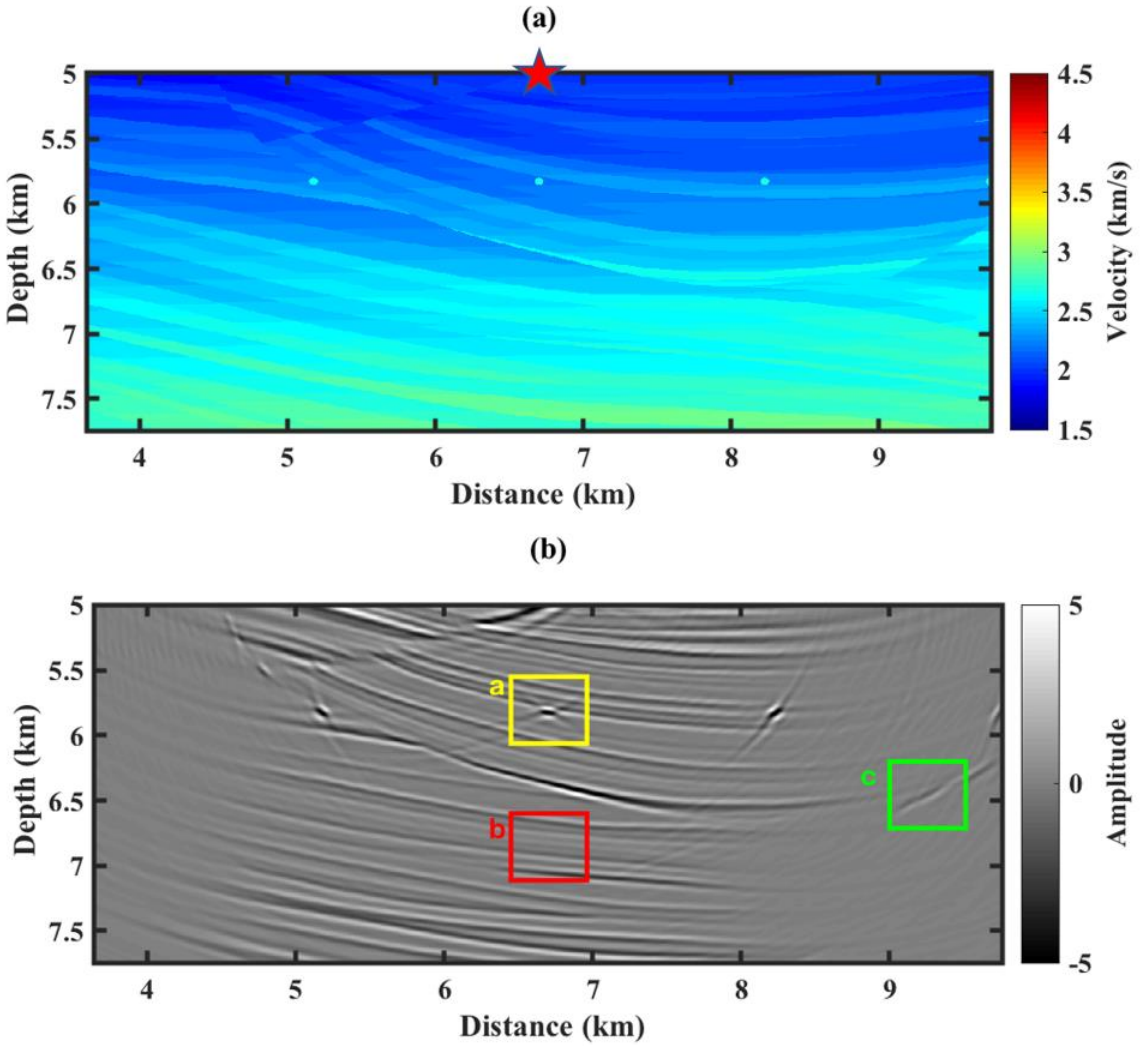

Figure 5.8. (a) The portion of the Sigsbee velocity model considered in study. The red star indicates the location of the source. 801 receivers are located across the 5 km depth with 85 meters spacing. A single source is used to image the section to examine the technique in poorly illuminated data. The source location is given by the red star. (b) RTM image of panel (a) using the correct velocity. The yellow, red and green boxes indicate the windows used for our analysis. We check the validity of the method of detecting diffractions in areas with different complexity. The yellow window has a reflection and a diffraction, the red window has reflections only and the green window has poorly imaged diffraction and reflections.

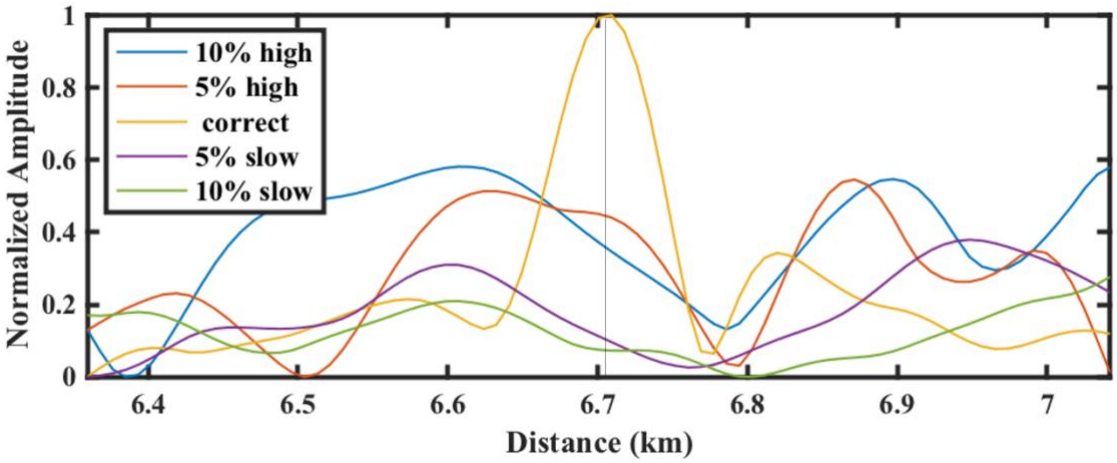

Figure 5.9. The summation of the envelope normalized at each receiver location for the yellow box shown in Figure 5.8b. The correct velocity summation is not symmetric as reflection contributes to the energy sum. For the correct velocity model, the maximum value still occurs at the location of the diffractor, while for other models it does not.

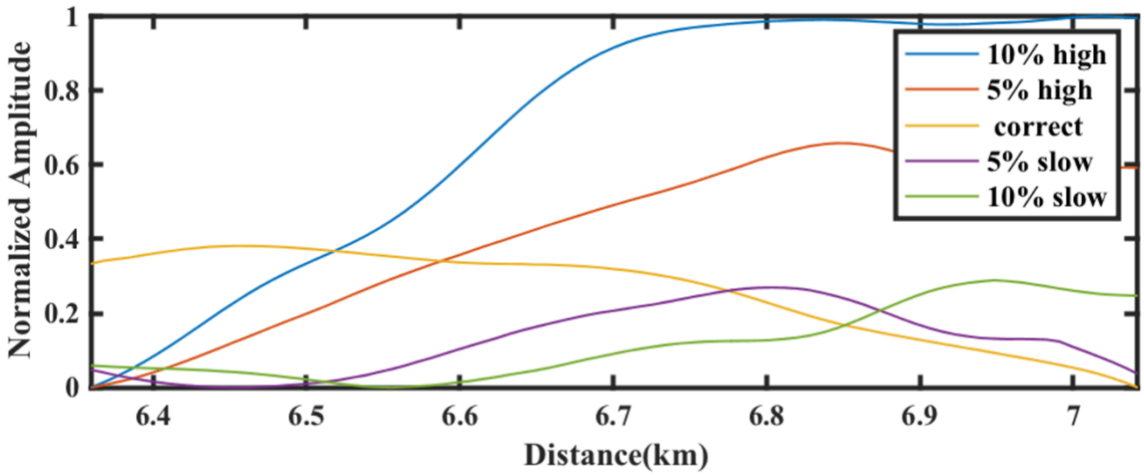

Figure 5.10. The summation of the envelope normalized at each receiver location for the red box shown in Figure 5.8b. The maximum and minimum velocities are dominated by reflectors and show no focusing.

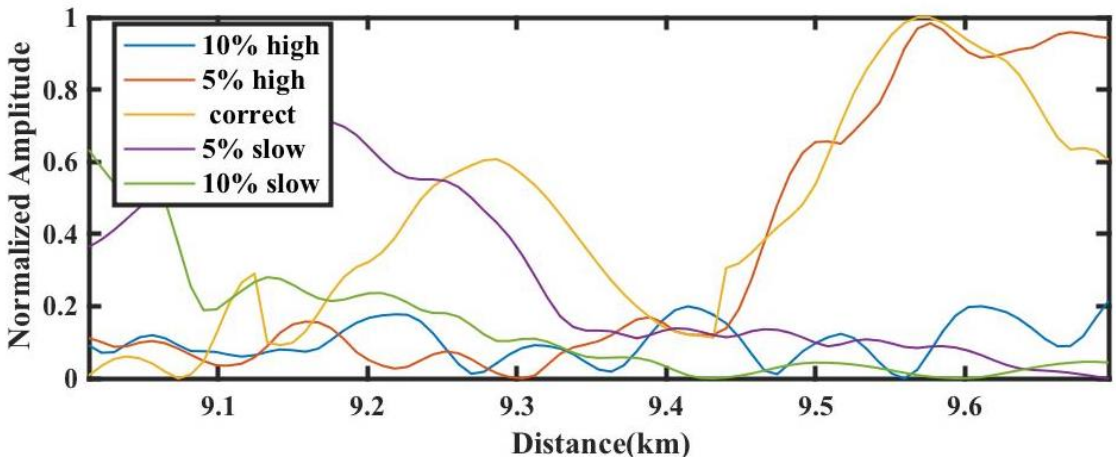

Figure 5.11. The summation of the envelope normalized at each receiver location for the green box shown in Figure 5.8b. Even for poorly illuminated diffractor, we still see a maximum energy at the location of the diffractor.

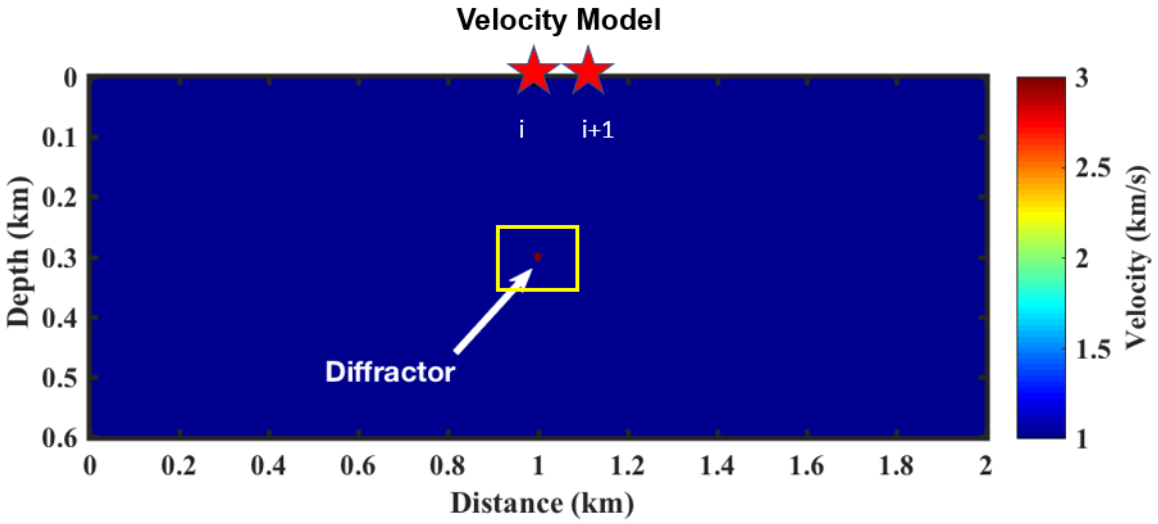

Figure 5.12. The model in depth used to cross-correlate two images from nearby experiments. The two sources are given by the red stars. 401 Receivers are located on the surface with 5 meters spacing.

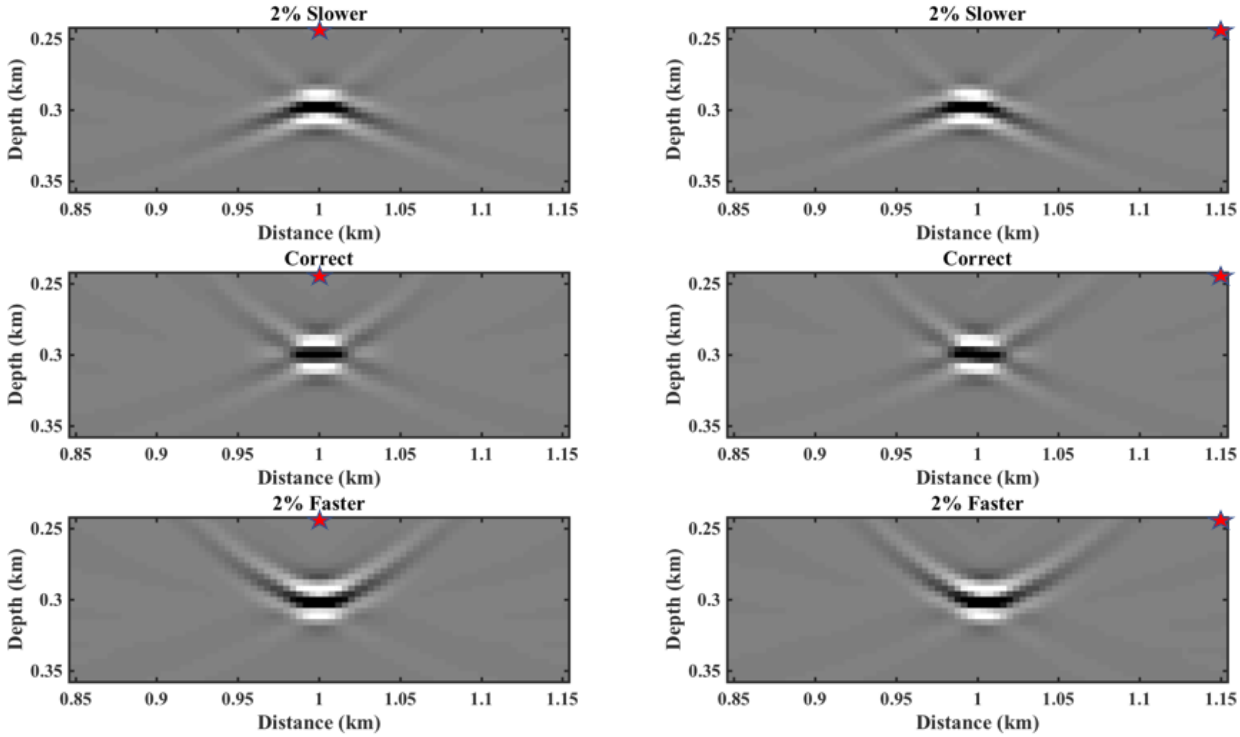

Figure 5.13. The imaged section from the two sources shown in Figure 5.12. The location of the source is given by the red star in each figure. The velocity used to generate the images are given in the title of each figure.

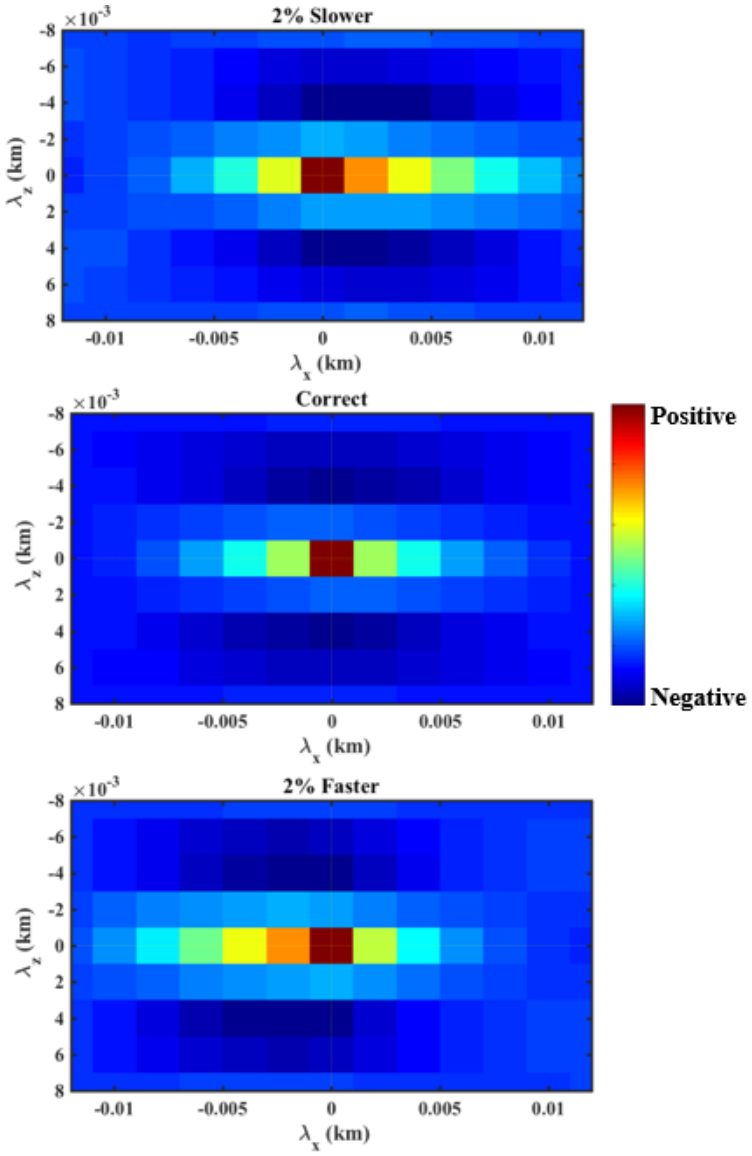

Figure 5.14. Local cross-correlation generated using the windows shown in Figure 5.13. We cross-correlate images generated from different sources (different experiments). Note the symmetric correlation image for the correct velocity and the asymmetric. for the inaccurate velocity models.λ_x and $\lambda_z$are the correlation lag in the image space. The size of the local window for cross-correlation is approximately equal to the maximum wavelength of the signal.

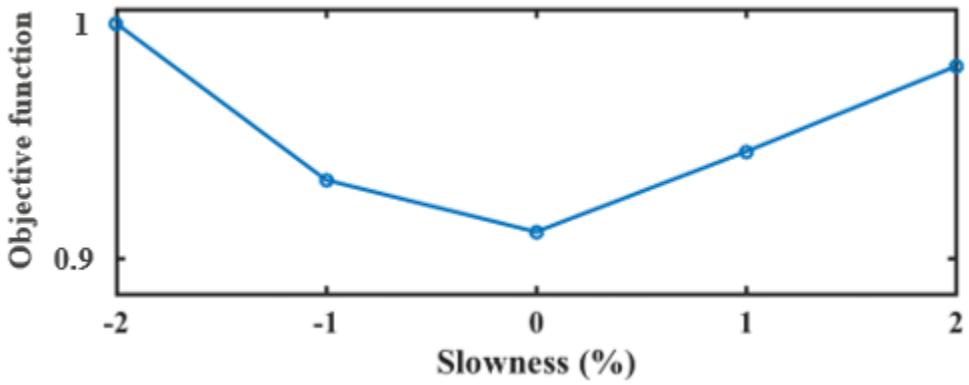

Figure 5.15. Values of the objective function for different errors in the velocity model. We consider a constant perturbation ranging from -2% to 2% of the correct velocity equation 5.

References

Al-Yahya, K., 1989, Velocity analysis by iterative profile migration.: Geophysics, **54**, 718-729.

Baysal, E., D. D. Kosloff, and J. W. C. Sherwood, 1983, Reverse time migration: Geophysics, **48**, 1514-1524.

Decker, L., D. Merzlikin, and S. Fomel, 2017, Enhancing seismic diffraction images using semblance-weighted least-squares migration: 87th Annual International Meeting of the SEG, Extended Abstracts, 5294-5299.

Fomel, S., E. Landa, and M. T. Taner, 2007, Poststack velocity analysis by separation and imaging of seismic diffractions: Geophysics, **72**, U89-U94.

Fomel, S., P. Sava, I. Vlad, Y. Liu, and V. Bashkardin, 2013, Madagascar: open-source software project for multidimensional data analysis and reproducible computational experiments: Journal of Open Research Software, **1**, e8.

Hale D., 2006, Fast local cross-correlations of images. 76th Annual International Meeting of the SEG, Extended Abstracts, 3160-3164.

Hale, D., B. Cox, and P. J. Hatchell, 2008, Apparent horizontal displacement in time-lapse seismic images: 88th Annual International Meeting of the SEG, Extended Abstracts, 3169-3173.

Huang, Y., D. Zhang, and G. T. Schuster, 2015, Tomographic resolution limits for diffraction imaging: Interpretation, **3**, 15-20.

Khaidukov, V., E. Landa, and T. J. Moser, 2004, Diffraction imaging by focusing and defocusing: An outlook on seismic super resolution: Geophysics, **69**, 1478-1490.

Khoshnavaz, M. J., A. Bóna, and M. Urosevic, 2018, Post-stack diffraction imaging in vertical transverse isotropy media using non-hyperbolic moveout approximations: Geophysical Prospecting, **66**, 273-281.

Klem-Musatov, K., H. Hoeber, M. Pelissier, and T. J. Moser, 2016, Seismic Diffraction: Society of Exploration Geophysicists.

Landa, E., V. Shtivelman, and B. Gelchinsky, 1987, A method for detection of diffracted waves on common-offset sections: Geophysical Prospecting, **35**, 359-374.

Lin, P., S. Peng, J. Zhao, X. Cui, and W. Du, 2018, A new scheme for velocity analysis and imaging of diffractions: Journal of Geophysics and Engineering, **15**, 1084-1093.

Masson, Y., and B. Romanowicz, 2017, Fast computation of synthetic seismograms within a medium containing remote localized perturbations: A numerical solution to the scattering problem: Geophysical Journal International, **208**, 674–692

Moser, T. J., and C. B. Howard, 2008, Diffraction imaging in depth: Geophysical Prospecting, **56**, 627-641.

Nakata, N., and G. C. Beroza, 2015, Stochastic characterization of mesoscale seismic velocity heterogeneity in Long Beach, California: Geophysical Journal International, **203**, 2049-2054.

Paffenholz, J. B., B. McLain, J. Zaske, and P. Keliher, 2002, Subsalt multiple attenuation and imaging: Observations from the Sigsbee2B synthetic data set: 72nd Annual International Meeting, SEG, Expanded Abstracts, 2122– 2125.

Perrone, F., P. Sava, and J. Panizzardi, 2015, Wavefield tomography based on local image correlations: Geophysical Prospecting, **63**, 35-54.

Rauch-Davies, M., Deev, K., Pelman, D., and Kachkachev-Shuifer, M., 2014, Diffraction imaging applied to pre-existing 3D seismic data to map fracture corridors in an unconventional play: First break, **32**, 87-90.

Rauch-Davies, M., S. Sutherland, B, M. Bradshaw, J. Codd and D. Kessler, 2018, Use of prestack depth migration for improving the accuracy of horizontal drilling in unconventional reservoir: The leading edge, **37**, 27-32.

Stolt, R.H., 1978, Migration by Fourier transform: Geophysics, **43**, 23-48.

Sava, P., B. Biondo, and J. Etgen, 2004, Diffraction-focusing migration velocity analysis: 74th Annual International Meeting of the SEG, Extended Abstracts, 2395-2398.

Sava, P. C., B. Biondi, and J. Etgen, 2005, Wave-equation migration velocity analysis by focusing diffractions and reflections: Geophysics, **70**, U19-U27.

Symes, W.W. 1991. Layered velocity inversion: A model problem from reflection seismology problem from reflection seismology. SIAM Journal on Mathematical Analysis **22**, 680–716.

Zhu, T., and J. Sun, 2016, Data-driven diffraction imaging of fractures using passive seismic data: 86th Annual International Meeting of the SEG, Expanded Abstracts

Chapter 6: Conclusions

The world's astonishing dependence on fossil fuels has not changed in the past four decades. Fossil fuels provide approximately 80% of the total energy used worldwide. This high percentage indicates that despite the recent glut in the market, the demand will be there for years to come. If my visits to the talks held by the Geophysical Society of Oklahoma City has taught me anything, it would be that people find a way to keep the oil business running to put "bacon" on the table. This also pushes the envelope for researchers to look for new and innovative ways to optimize drilling costs.

Fractures and faults are critical for drilling optimization. Fracture characterization aims to understand fracture patterns, so that an optimum strategy can be devised for completing and effectively draining a fractured reservoir. Fractures provide fluid migration pathways that can be exploited to extract reserves stored in low permeability rocks. This economic importance is driving significant improvement in ways seismic attributes can be used to characterize the fractures. Depending on the scale of the fractures, they can be stochastically or deterministically characterized on seismic data. In this dissertation, I examined the fracture and fault signatures imaged/enhanced using different seismic attributes.

Geometric attributes are very effective in detecting large-scale fractures. In chapter 2, I enhanced the expression of faults and subtle features using a continuous wavelet transform based workflow to suppress acquisition footprint. This technique relies on an edge detection attribute's sensitivity to periodic noise to design a mask and suppress the noise on seismic amplitude data. The workflow is suitable for legacy and mega-merged data where economic constrains limit reshooting or more carefully reprocessing the data.

In chapter 3, I showed that although Fourier-based 5D interpolation improves specular reflections, seismic edges may be unintentionally suppressed. Coherence anomalies associated with faults, karst and channels were suppressed in after 5D regularization of a modern well sampled Mississippi Lime survey. Artefacts can be created in the far offsets, and if not muted, potentially providing misleading AVO and prestack inversion predictions, and the stacked volume being overly influenced by the velocity used in 5D interpolation. Until these algorithm's limitations are addressed, I suggest that complimenting 5D interpolated with non-interpolated data is essential for constructing a better image of the subsurface.

In chapter 4, I analyzed amplitude variation with offset and azimuth to predict the signature of small-scale fractures. Detecting fractures using this technique assumes that fractures are uniformly spaced. I examined the signature of the fractures when this assumption is violated by fracture clustering. The presence of irregularly spaced can result in deviation of the amplitude predicted by the effective medium theory and inaccurate fracture characterization. I find that forward modeling of the amplitude variation with offset (AVO) for the target horizon using the velocity model provides insight into the location of the fractures within the reservoir. Fractures located at the bottom of the reservoir have no effect on the top reflection. Hence, similar AVO trends are observed for both the bottom located fractures and the modeled isotropic case for the top reflection.

In chapter 5, I analyzed how detected diffraction waves due to fracture can enhance imaging the subsurface. Due to diffraction's sensitivity to velocity inaccuracy, they are diffractions are useful in updating the velocity to build a more accurate sub-surface image. I prototyped an interactive method whereby an interpreter first identifies areas with potential diffractions. Once located, the interpreter perturbs the velocity model and sums the energy within the analysis

window to analyze the degrees of diffraction focusing. To improve on the velocity, I use image cross-correlation between nearby common shot gathers and analyze the results. A more symmetric cross-correlation indicates an accurate velocity model. Finally, I combine observations from different nearby experiments pairs to construct an objective function that can be used in a differential semblance optimization solution.